Metabolic Heterogeneity in Molecular Subsets of Diffuse Large B-cell Lymphoma

HARVARD UNIVERSITY
Graduate School of Arts and Sciences

DISSERTATION ACCEPTANCE CERTIFICATE

The undersigned, appointed by the

Division of Medical Sciences

in the subject of Cell Biology

have examined a dissertation entitled

Metabolic Heterogeneity in Molecular Subsets of Diffuse Large B-cell Lymphoma

presented by Illana Allake Stanley

candidate for the degree of Doctor of Philosophy and hereby certify that it is worthy of acceptance.

Signature: _____

Typed Name: Dr. Gary Yellen

Signature: _____

Typed Name: Dr. Suzanne Gaudet

Signature: _____

Typed Name: Dr. David Hockenbery

_____

Dr. Susan Dymecki, Program Head

Date: August 22, 2014

_____

Dr. David Lopes Cardozo, Director of Graduate Studies

Metabolic Heterogeneity in Molecular Subsets of Diffuse Large B-cell Lymphoma

A dissertation presented

by

Illana Allake Stanley

to

The Division of Medical Sciences

in partial fulfillment of the requirements

for the degree of

Doctor of Philosophy

in the subject of

Cell Biology

Harvard University

Cambridge, Massachusetts

August 2014

Metabolic Heterogeneity in Molecular Subsets of Diffuse Large B-cell Lymphoma

ABSTRACT

Cells adapt their metabolism to satisfy changing bioenergetic and biosynthetic needs. Investigation of metabolic reprogramming in cancer has provided insight into the metabolic control of proliferation and survival. While the predominant focus of this field has been aerobic glycolysis (the Warburg effect), increasing evidence points to a complex landscape of tumor metabolic circuitries beyond aerobic glycolysis, including varied degrees of mitochondrial contribution to tumor metabolism.

To investigate alternative metabolic programs compatible with tumor growth, we turned to Diffuse Large B-cell Lymphoma (DLBCL), a highly heterogeneous disease encompassing discrete clusters or subtypes defined by tumor-intrinsic genetic distinctions. In one classification scheme, a B-cell receptor (BCR)/proliferation cluster identified BCR-dependent DLBCLs with elevated expression of BCR signaling components. A second subset, OxPhos-DLBCL, displayed increased expression of mitochondrial oxidative phosphorylation genes, and was insensitive to BCR inhibition. However, the functional attributes of OxPhos-DLBCLs and the nature of their BCR-independent survival were unknown.

Upon integrative analyses of DLBCL subtypes, we uncovered quantitative proteome- and metabolome-level signatures associated with differences in nutrient and energy metabolism. Specifically, BCR-DLBCLs have greater glycolytic flux typical of the Warburg phenotype. Unlike BCR-DLBCLs, OxPhos-DLBCLs channel the majority of glucose-derived pyruvate into mitochondria, display elevated mitochondrial electron transport chain (ETC) activity, ATP production, and fatty acid oxidation (FAO). Importantly, these metabolic distinctions are associated with subtype-selective survival mechanisms. Moreover, acute inhibition of BCR signaling in BCR-DLBCLs increased their FAO capacity, thus revealing a reciprocal relationship between BCR and FAO.

Further dissection of mitochondrial function in OxPhos-DLBCLs indicates that increased mitochondrial metabolism is integrated with at least two homeostatic mechanisms that help maintain ETC activity and FAO capacity. In particular, OxPhos-DLBCLs harbor robust protein-level enrichment of mitochondrial translation factors required for the synthesis of mitochondrial-DNA-encoded ETC subunits. Inhibition of the mitochondrial translation pathway is selectively toxic to OxPhos-DLBCLs. A second mitochondrial homeostatic pathway, mitochondrial network dynamics, also proved relevant to OxPhos-DLBCLs. Compared to BCR-DLBCLs, OxPhos-DLBCLs display a fragmented mitochondrial network that supports their FAO capacity. Overall, these findings demonstrate previously unappreciated metabolic heterogeneity in molecular subsets of DLBCL and uncover BCR-independent survival mechanisms linked to mitochondrial FAO, protein translation, and network architecture.

Table of Contents

LIST OF FIGURES AND TABLES

FIGURES

TABLES

SUPPLEMENTARY FIGURES AND TABLES

ACKNOWLEDGEMENTS

Getting my PhD has been a long, at times challenging, but ultimately rewarding experience and I am grateful for the support I have received along the way. I first and foremost want to thank my advisor Dr. Nika Danial, who took a leap of faith accepting a 4th year graduate student into her lab. I will be forever grateful for Nika's dedication to training and her tireless efforts to support both my thesis work and my professional development. Under her tutelage I have grown as an independent researcher, gaining experience not only in research at the bench but also writing and scientific presentation skills that have proved invaluable.

I would also like to thank my dissertation advisory committee, Bruce Zetter, Rosalind Segal and Margaret Shipp for their thoughtful and insightful feedback during the course of my dissertation work. They provided much needed support and helped guide my thesis work in a productive and expedient fashion for which I am grateful. Thanks also to my dissertation examiners, David Hockenbery, Suzanne Gaudet and Gary Yellen, for taking the time to critically evaluate my thesis work.

I received excellent guidance from the BBS office, especially with regards to selecting Nika Danial as my new PhD mentor. I cannot imagine a staff more dedicated to student welfare.

My dissertation work would not have been possible without the help of my esteemed colleagues including Margaret Shipp, Bjoern Chapuy, Linfeng Chen, Stefano Monti, and Scott Rodig, who assisted with procuring DLBCL cell lines, patient samples and patient expression profiles. I am also indebted to Jarrod Marto and Scott Ficarro who provided essential support in the characterization of DLBCL mitochondrial proteomes. Thanks also to Craig Braun who has assisted with an ongoing investigation of specific mitochondrial dynamics factors in DLBCL.

The imaging studies presented in this dissertation were the result of a close and productive collaboration with Orian Shirihai and Marc Liesa. Thanks also to Kiana Mahdaviani who showed me how to visualize lipid droplets.

I would also like to thank Ben Szlyk and Eric Smith for their assistance with the graphical art presented in this dissertation.

My colleagues in the lab have been a tremendous resource. Pilar Caro, Amar Kishan, Erik Norberg, and technicians Klaudia Polak, Elaura Patton and Ana Lako worked with me on the DLBCL project. I would also like to thank current and past lab members, Alfredo Giménez-Cassina, Meghan Tedoldi, Sofia Ribeiro, Luisa Garcia-Haro, Accalia Fu, Elizabeth Lane, and Sanda Ljubicic for their support and friendship during my thesis work.

I could not have done this without the support of my family. I would like to thank my mother, Paula, who was never more than a phone call away when I needed to hear a friendly voice. My sister, Yemonja, who provided emotional support as we both embarked on challenging career paths. My brother, Cedar, who I watched grow up during my graduate education and who always gave me a reason to smile. I want to especially thank my father, Thomas, for proofreading this dissertation and passing on the wisdom of his own PhD experience. I would also like to thank my grandmother, Joan Stanley, a former biologist, who has provided endless motivation and support to my education. And I especially want to thank my partner, Vivek Shenoy. He stood by me through the difficult process of changing mentors and all that has followed since joining Nika's lab. Without his support this PhD would not have been possible.

Chapter 1

INTRODUCTION

Carbon substrate metabolism in the programming of cell fate and function

Different cell states have distinct anabolic and catabolic needs that can be fulfilled by processing specific carbon substrates such as glucose, fatty acids, amino acids, and ketone bodies. The cell's choice of carbon substrates not only fuels biosynthetic pathways, but also enables programmatic adaptations to stress conditions that go beyond compensating for changes in nutrient availability. Recent advances in metabolomics and metabolic flux analysis combined with high throughput interrogation of the genome and proteome have provided some insights into molecular determinants of fuel choice and its contribution to cell fate and function in both normal and disease states. In particular, the cell's choice of carbon substrates can influence transitions between quiescence and proliferation, modulate cellular differentiation and lineage specification, produce resistance or sensitivity to oxidative stress, facilitate DNA and tissue repair, and allow adaptation to nutrient changes [1-3]. Furthermore, metabolism of particular carbon substrates can influence cell identity and behavior through programmatic alterations in gene expression and epigenetic modifications, at least in part, by affecting the activity of chromatin modifying enzymes [4]. Understanding how cells choose to preferentially utilize a particular carbon substrate and defining its specific metabolic outputs can provide a molecular handle on metabolic control of cellular proliferation, differentiation and survival in normal physiology and under pathologic conditions.

The following sections highlight the contributions of substrate metabolism to biosynthetic and bioenergetic needs of cell growth. Within this context, the emphasis is placed on metabolic pathways in charge of generation and utilization of precursors central to anabolic reactions and the contribution of mitochondria to both anabolic and bioenergetic requirements of cell growth. In aggregate, these considerations are meant to showcase the breadth and diversity of metabolic solutions to the specific demands of cellular proliferation and survival, particularly as it relates to cancer.

Meeting the biosynthetic requirements of proliferation: The role of aerobic glycolysis

The specific needs of the proliferative state for lipids, amino acids, reducing equivalents, and nucleotides necessitate reprogramming of carbon substrate utilization and production of metabolic precursors for biosynthetic reactions [2]. Moreover, given the requirement for reducing potential in order to generate biomass, the metabolic program in the proliferative state includes increased NADPH production [2]. Aerobic glycolysis or the Warburg effect, which refers to increased glycolytic conversion of glucose to lactate over mitochondrial glucose oxidation even in the presence of sufficient oxygen, was originally recognized as a chief metabolic alteration in cancer cells, and recently appreciated as a metabolic feature of proliferating cells in general [2, 5, 6]. It is increasingly recognized that the predominant contribution of aerobic glycolysis to proliferation is the provision of biosynthetic intermediates for new biomass rather than energy production [7]. For example, increased flux through the pentose phosphate pathway (PPP), a biosynthetic branch point of glycolysis at glucose-6-phosphate (Figure 1.1), contributes to NADPH synthesis, and thereby supports fatty acid and cholesterol synthesis as well as anti-oxidant mechanisms. The PPP also generates precursors for nucleotide biosynthesis (ribose-5-phosphate) [2] (Figures 1.1 and 1.2). Another glycolytic intermediate, 3-phosphoglycerate (3PG), can contribute to *de novo* serine biosynthesis via phosphoglycerate dehydrogenase (PHGDH) [8, 9] (Figures 1.1 and 1.2). Serine can in turn influence purine biosynthesis by generating glycine and one-carbon donors such as N^{10}-formyl-THF (Figure 1.2). The availability of glycolytically-derived metabolites for the biosynthetic reactions described above is dependent on glycolytic flux as well as the regulated entry of glucose-derived pyruvate into the mitochondrial tricarboxylic acid (TCA) cycle. Several metabolic control points allow proliferating cells to enrich for upstream glycolytic intermediates at the expense of pyruvate utilization by mitochondria. The conversion of phosphoenolpyruvate (PEP) to pyruvate by pyruvate kinase (PK), the final step of glycolysis, is a prime example of such a control point (Figure 1.1).

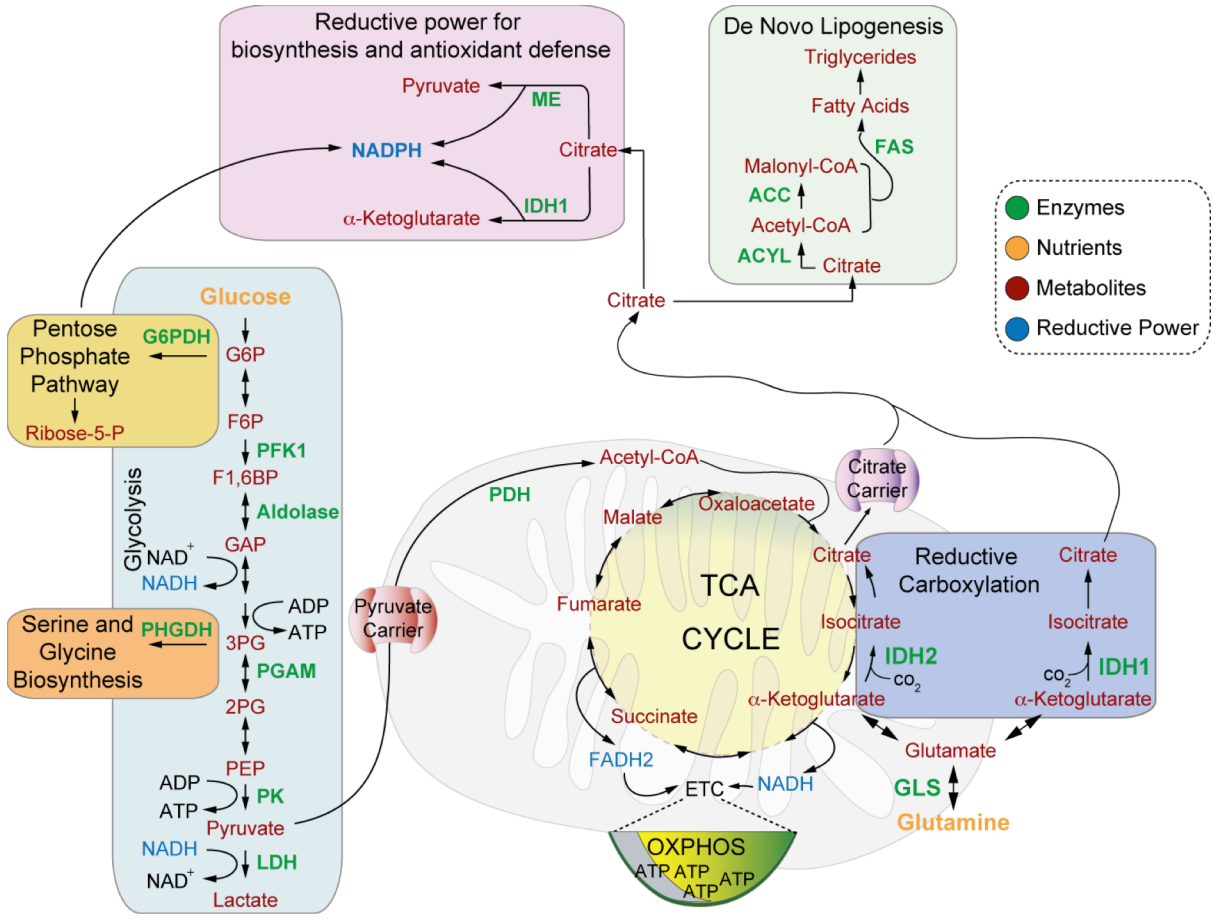

Figure 1.1. Schematic of select pathways in charge of glucose and glutamine metabolism, as well as metabolic outputs of citrate that relate to biosynthesis and antioxidant capacity

Glucose-derived metabolites can be used to generate pyruvate or to supply precursors for the pentose phosphate pathway and *de novo* serine synthesis. Pyruvate can be metabolized to lactate in the cytosol or transported into mitochondria via the pyruvate carrier. Mitochondrial pyruvate can then be used for the synthesis of acetyl-CoA and citrate. Under certain circumstances, citrate can also be generated by reductive carboxylation of glutamine. Biosynthetic reactions also require reducing equivalents in the form of NADPH, which can be supplied by cytosolic citrate, via isocitrate dehydrogenase (IDH) and the malic enzyme (ME), or by the pentose phosphate pathway.

Abbreviations: FAS – Fatty acid synthase, ACC – Acetyl-CoA carboxylase, ACYL – ATP Citrate lyase, ME – Malic enzyme, IDH – Isocitrate dehydrogenase, GLS – Glutaminase, G6PDH – Glucose-6-phosphate dehydrogenase, PFK1 – Phosphofructokinase 1, PHGDH – Phosphoglycerate dehydrogenase, PGAM – Phosphoglycerate mutase, PK – Pyruvate kinase, LDH – Lactate dehydrogenase, PDH – Pyruvate dehydrogenase, ETC – Electron transport chain, OXPHOS – Oxidative phosphorylation, TCA – Tricarboxylic acid cycle.

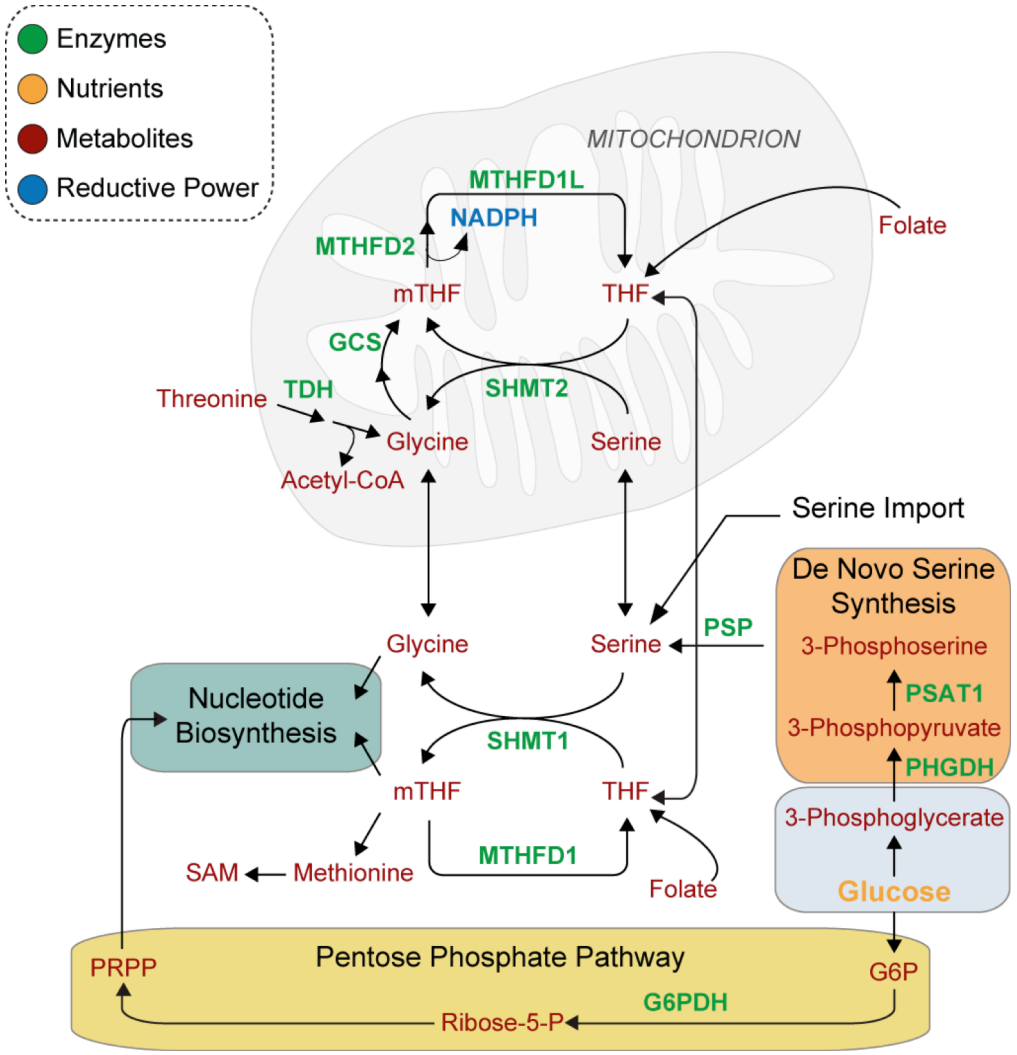

Figure 1.2. Nucleotide biosynthesis and the contribution of serine and glycine to one-carbon metabolism

Nucleotide biosynthesis requires input of carbons from tetrahydrofolate (THF), glycine, and phosphoribosyl pyrophosphate (PRPP). Folate-derived THF can be metabolized in the cytosol or in mitochondria by the indicated enzymes. THF is converted to mTHF (methylene-tetrahydrofolate) in a cycle that is coupled to the conversion of serine to glycine. Mitochondrial glycine can also contribute to mTHF via the glycine cleavage system (GCS). Serine, a major one-carbon donor for the synthesis of mTHF, can be imported from the extracellular milieu, synthesized from glycine, or from glucose-derived carbons. Glycine can be generated from serine or from threonine. In addition to nucleotide biosynthesis, one-carbon metabolism involving mTHF supports methionine and SAM production as well as NADPH synthesis.

Abbreviations: SHMT1 – Serine hydroxymethyltransferase 1, SHMT2 – Serine hydroxymethyltransferase 2, MTHFD1L – 10-formyl-tetrahydrofolate synthetase , MTHFD1 – Methylenetetrahydrofolate dehydrogenase 1, MTHFD2 – Methylenetetrahydrofolate dehydrogenase 2, PSP – Phosphoserine phosphatase, TDH – Threonine dehydrogenase, PSAT1 – Phosphoserine aminotransferase, PHGDH – 3-Phosphoglycerate dehydrogenase, mTHF – Methylene-tetrahydrofolate, THF – Tetrahydrofolate, SAM – S-Adenosyl-methionine, G6PDH – Glucose-6-phosphate dehydrogenase, PRPP – Phosphoribosyl pyrophosphate, GCS – Glycine cleavage system.

In certain settings, a preferential switch to the less active PKM2 isoform over the constitutively active PKM1 or loss of PK activity can facilitate diversion of glycolytic intermediates to the PPP and *de novo* serine biosynthesis [10-12]. In terms of pathway flux, however, these metabolic shifts are not absolute, and a percentage of PEP can generate pyruvate that subsequently enters the mitochondria.

Meeting the biosynthetic requirements of proliferation: The role of mitochondrial metabolism

Despite the clear importance of glycolytic intermediates for proliferation, glycolysis is not the only source of biosynthetic precursors for new biomass. Mitochondria make several important anabolic contributions, including citrate synthesis and folate metabolism. As described below, these are in turn integrated with metabolism of a variety of substrates including amino acids and fatty acids.

Pyruvate, citrate and de novo lipogenesis. Generation of citrate from pyruvate in mitochondria is dependent on both regulated mitochondrial transport of pyruvate through the pyruvate carrier and the activity of pyruvate dehydrogenase (PDH), which decarboxylates pyruvate to acetyl-CoA for entry into the TCA cycle (Figure 1.1). PDH activity is regulated through several mechanisms, including allosteric modulation and phosphorylation. Pyruvate dehydrogenase kinases (PDKs) phosphorylate and inhibit PDH, while pyruvate dehydrogenase phosphatases (PDPs) remove this inhibitory post-translational modification [13]. Several oncogenes and oncogenic signaling pathways converge on regulation of PDH phosphorylation [14-18]. PDH activity is highly varied across different cancer types. In certain cancers, increased PDH activity may serve as a metabolic adaptation to support citrate synthesis [19, 20]. Citrate produced by the PDH reaction is transported to the cytosol by the mitochondrial citrate carrier [21], and subsequently used for *de novo* fatty acid synthesis, a chief anabolic requirement of membrane biogenesis and cellular proliferation. *De novo* fatty

acid synthesis is regulated by the coordinate function of acetyl-CoA carboxylase (ACC) and fatty acid synthase (FAS) (Figure 1.1). Cytosolic acetyl-CoA used for fatty acid synthesis is produced from citrate through the reaction catalyzed by ATP citrate lyase (ACLY) (Figure 1.1).

***Glutamine-mediated anaplerosis*.** The lipogenic fate of glucose-derived carbons and the attendant export of citrate from mitochondria necessitate replenishment of TCA cycle intermediates (also known as anaplerosis). This is fulfilled by extracellular glutamine, which provides important anaplerotic input into the TCA cycle once it is metabolized through glutaminase (GLS) as well as glutamate dehydrogenase to produce α-ketoglutarate and ultimately oxaloacetate (OAA) (Figure 1.1). In addition to anaplerotic provision of OAA, glutamine can be used to generate NADPH through the malic enzyme reaction (ME, Figure 1.1), providing additional reducing power for fatty acid synthesis and other anabolic reactions. The coordinate utilization of glucose- and glutamine-derived carbons to ensure fatty acid synthesis is consistent with high rates of both glucose and glutamine uptake during rapid proliferation [22-24]. While glutaminolysis has a predominant anaplerotic role in replenishment of OAA, under certain nutrient deprivation conditions, it can be used to generate citrate through reductive carboxylation. This involves conversion of glutamine-derived α-ketoglutarate to isocitrate by the reverse reactions of the NADPH dependent isocitrate dehydrogenase (IDH) isoforms [25-27] (Figure 1.1). However, the physiologic contribution of reductive carboxylation to citrate synthesis is not fully known.

Fatty acid β-oxidation. Beyond glutamine, other non-glucose mitochondrial substrates can also support cellular proliferation in a context-specific manner. Fatty acid β-oxidation (FAO) in the mitochondrial matrix serves as an additional source of acetyl-CoA for both ATP synthesis and citrate production (Figure 1.3). For example, in ovarian cancers that metastasize to the omental fat pad, increased mitochondrial FAO is supported by lipids supplied by neighboring adipocytes.

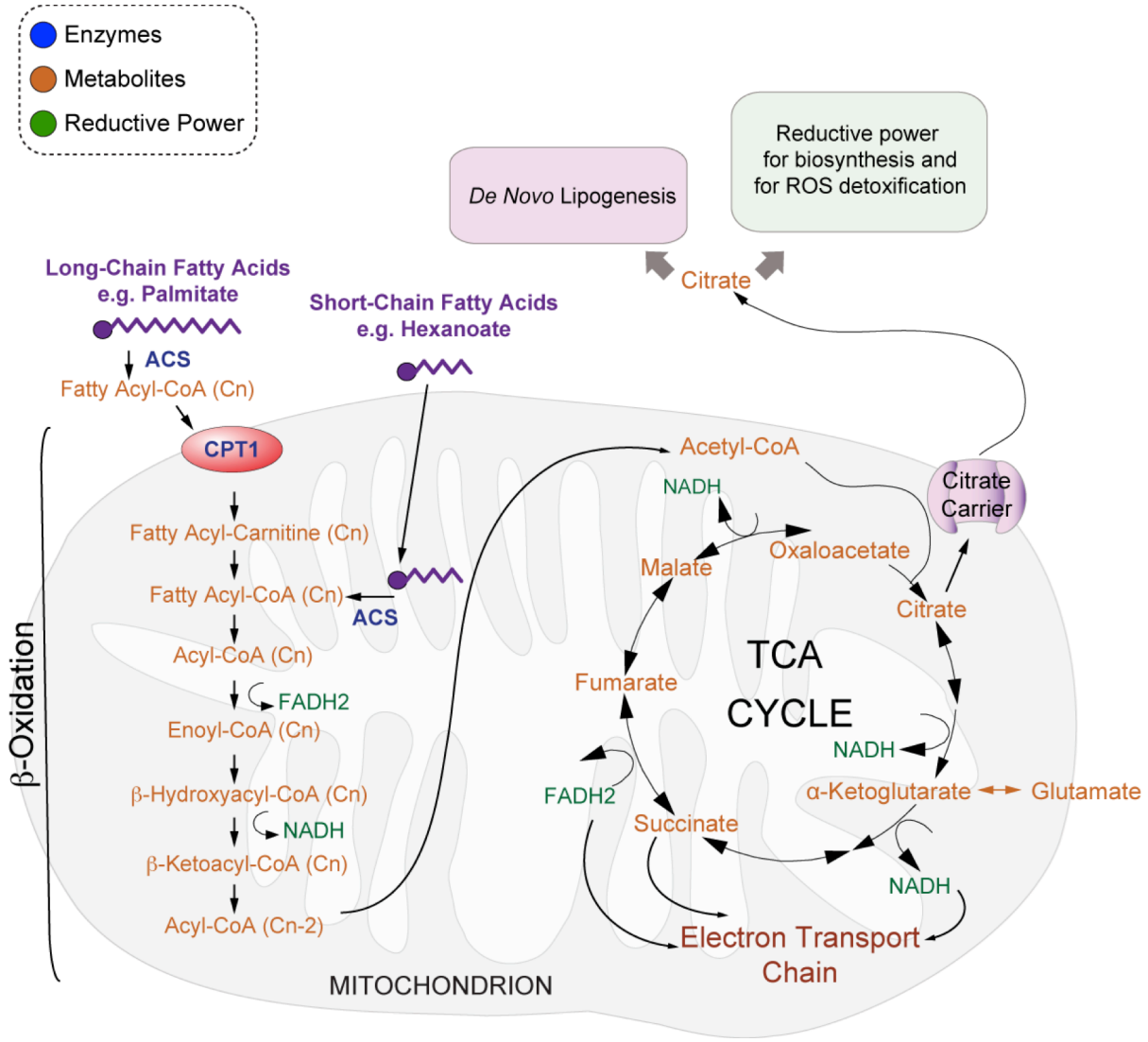

Figure 1.3. Fatty acid oxidation and contribution to the citrate pool
Long chain fatty acids (FAs) are imported into the mitochondria in a CPT1 dependent manner after activation to their fatty acyl-CoA derivatives, while short chain FAs diffuse across the mitochondrial membranes. They are then oxidized to acetyl-CoA units so that the FA chain length is reduced by two carbons in every cycle of β-oxidation. Fatty acid-derived acetyl-CoA units can then enter the TCA cycle and be completely oxidized to generate ATP through OXPHOS or contribute to the citrate pool for export to the cytosol, *de novo* lipogenesis and generation of NADPH for reductive potential.
Abbreviations: ACS – Acyl-CoA synthetase, CPT1 – Carnitine palmitoyl transferase 1. Cn denotes fatty acid chain length, which is reduced by 2 carbons with every cycle of acetyl-CoA production.

The elevated FAO observed in these cells is dependent on AMPK-mediated inhibition of ACC and the attendant increase in fatty acid import into the mitochondria via carnitine palmitoyl transferase (CPT)1 [28] (Figure 1.3). In a 3D culture model of breast cancer, FAO provides pro-survival benefits following matrix-detachment and loss of growth factor-mediated glucose uptake [29]. Increased FAO in this setting appears to be driven by the promyelocytic leukemia protein (PML) in a PGC1α-dependent manner. In this model, FAO-mediated survival under anoikis ultimately allows luminal filling, which precedes breast cancer development [29]. Furthermore, as discussed in Chapter 2, FAO provides pro-proliferative and pro-survival benefits to a subset of diffuse large B-cell lymphomas (DLBCLs) [19].

Mitochondrial one-carbon metabolism. Another important anabolic contribution of mitochondria is made through folate-dependent one-carbon metabolism also known as the mitochondrial glycine biosynthetic pathway. This pathway provides a significant portion of the one-carbon pool required for *de novo* purine biosynthesis [30] (Figure 1.2). The major reactions of one-carbon metabolism occur in both the cytosol and the mitochondria with limited direct exchange of folate metabolites between compartments. Mitochondrial one-carbon metabolism is particularly relevant for cancer cell proliferation as evident from recent global metabolic profiling of the NCI-60 cancer cell lines, which indicated a tight correlation between proliferation and both glycine uptake and the mitochondrial glycine biosynthetic pathway [31]. Consistent with this, proliferation rates across the NCI-60 panel correlated with the expression of three enzymes in the mitochondrial glycine biosynthetic pathway, serine hydroxymethyl transferase (SHMT)2, methylenetetrahydrofolate dehydrogenase (MTHFD)1 and MTHFD2 (Figure 1.2), as opposed to the expression of cytosolic folate metabolizing enzymes [31]. A subsequent study describing mRNA analysis of the most highly expressed metabolic enzymes across a large panel of primary tumors representing 19 cancer types identified *MTHFD2* as a top scoring gene, which correlated with poor survival in breast cancer [32].

Two recent studies have also uncovered the importance of mitochondrial folate metabolism for NADPH production through the MTHFD2 reaction [33, 34] (Figure 1.2). NADPH can be generated by complete oxidation of 10-formyl-tetrahydrofolate in mitochondria to a level that is comparable with NADPH produced from the PPP [34]. Accordingly, inhibition of mitochondrial one-carbon metabolism following depletion of MTHFD2 is associated with oxidative stress [34]. This extends the anabolic benefits of this pathway to both nucleotide synthesis and generation of reducing power.

Folate metabolism may be further integrated with threonine dehydrogenase (TDH) activity, a mitochondrial enzyme that catalyzes the production of glycine from threonine (Figure 1.2). TDH activity was recently shown to be up-regulated in mouse embryonic stem cells compared with their differentiated progeny and to be required for their growth and survival [35, 36]. Overall, the aforementioned observations underscore the relevance of the mitochondrial one-carbon pathway to cell growth in both non-malignant and malignant cells.

Meeting the energy and redox requirements of cell growth: The role of mitochondrial homeostatic mechanisms

In addition to biosynthetic intermediates necessary for generating new biomass, proliferating cells must also satisfy energetic demands and maintain redox balance. Mitochondria can directly impact these parameters as they are the main source of ATP and major producers of reactive oxygen species (ROS). Several homeostatic pathways converge on the functional quality of mitochondria in terms of energy and ROS metabolism. Among these, the assembly, organization, and functional fidelity of the mitochondrial electron transport chain (ETC) can have a profound impact on mitochondrial ATP generation and calcium buffering, as well as the activity of several calcium-regulated TCA cycle dehydrogenases and the capacity of mitochondria to metabolize fuel substrates, ultimately affecting cellular proliferation and survival.

The ETC, which is comprised of a series of large multi-subunit protein complexes housed within the mitochondrial inner membrane, carries out redox reactions involving the transfer of electrons from NADH and $FADH_2$ supplied by the TCA cycle. Oxygen is consumed during this process to provide a final electron acceptor. Electron transfer is accompanied by proton extrusion from the mitochondrial matrix to the inner membrane space, producing an electrochemical gradient. The energy stored in the protons as they flow back to the matrix is then used to combine inorganic phosphate with ADP to generate ATP by the enzymatic action of the mitochondrial ATP synthase complex.

A functional ETC requires the proper synthesis, localization and assembly of a large number of protein subunits encoded by both the nuclear and mitochondrial genomes. This requires transcription and translation of mitochondrial DNA (mtDNA)-encoded genes by a dedicated mitochondrial translation machinery independent of the pathway in charge of translating mRNAs encoded by the nuclear genome [37]. In addition, a host of chaperones and proteases exist to ensure proper folding and assembly of ETC complexes, as well as to clear excess or misfolded components. For example, the inner membrane m-AAA and i-AAA proteases are central to degrading unassembled or damaged ETC complexes, and their loss of function is associated with profound ETC defects in several human pathologies [38-40]. In addition to proper assembly of subunits within ETC complexes, the organization of ETC complexes into supercomplexes has been shown to impact mitochondrial bioenergetics. In particular, dynamic assembly of ETC complexes I, III and IV into supercomplexes was shown to be tightly integrated with the pattern and kinetics of electron flow through the ETC, ultimately influencing the efficiency of carbon substrate oxidation [41]. In addition, the assembly and organization of ETC complexes is integrated with mitochondrial morphology and dynamics [42].

Mitochondria are also a major source of cellular ROS generated by incomplete reduction of oxygen due to electron slippage, predominantly from respiratory chain complexes I and III [43-45]. Low levels of ROS, particularly hydrogen peroxide (H_2O_2), can be important for pro-

proliferative signals. For example, certain KRAS-driven cancer cells require mitochondrial ROS for proliferation, suggesting that mitochondrial redox signaling can support oncogenic growth pathways [46]. However, excessive ROS can cause irreversible damage to cellular lipids, proteins and DNA and push cells towards apoptosis. Mitochondria are particularly susceptible to such damage due to the higher probability of H_2O_2 reacting with iron-containing complexes in the mitochondrial inner membrane and matrix. Several mechanisms are in place to keep mitochondrial ROS in check through modulation of ROS production as well as ROS clearance. In particular, mitophagy has emerged as an important homeostatic pathway of mitochondrial quality control, whereby damaged mitochondria or mitochondria that produce high levels of ROS due to inefficient ETC function, are cleared from the mitochondrial network [47].

The aforementioned pathways are but a few examples of a diverse and complex array of homeostatic mechanisms evolved to ensure the functional fidelity of mitochondrial substrate and energy metabolism. As such, they can indirectly influence cellular proliferation, survival and stress responses.

Metabolic heterogeneity in the context of cancer and an overview of this dissertation

Significant progress has been made in our understanding of how aerobic glycolysis contributes to proliferation and underlying signaling pathways. However, the universal applicability of these findings to all proliferating cell types has not been established and, in fact, as discussed above, there is substantial evidence to suggest that other metabolic pathways also make important contributions to proliferation in a cell type- and context-dependent manner. The diversity and complexity of metabolic solutions to meeting the biosynthetic and bioenergetic requirements of cell growth is also reflected by the heterogeneity of metabolic programs that provide pro-proliferative and pro-survival advantages to cancer cells. Understanding this heterogeneity at the molecular level requires a detailed dissection of metabolic circuits and associated dependencies on fuel utilization and biosynthetic pathways of individual tumor types.

This will ultimately facilitate the development of therapies tailored to specific metabolic vulnerabilities in the relevant tumor types.

The heterogeneity of metabolic fingerprints in tumors may be relevant, not only across different cancers, but also within distinct subtypes of heterogeneous tumors that otherwise share a common initial diagnosis. The following chapters describe the integrative dissection of metabolic circuits in one of the most heterogeneous types of cancer, Diffuse Large B-cell Lymphoma (DLBCL), which uncovered distinct patterns of nutrient and energy metabolism and associated targetable dependencies in separate molecular subtypes of DLBCL. Chapter 2 investigates the metabolic attributes of OxPhos-DLBCLs, a molecular subset of DLBCL previously shown to be genetically distinct from B-cell receptor (BCR)-dependent DLBCLs (BCR-DLBCLs). OxPhos-DLBCLs do not require a functional BCR, which normally promotes the survival of BCR-DLBCLs through a PI3K-dependent mechanism [48, 49]. They also display increased expression of mitochondrial oxidative phosphorylation genes [50]. However, the functional attributes OxPhos-DLBCLs and the nature of their BCR-independent survival mechanisms was not known. This investigation identified clear differences in glucose and fatty acid metabolism, as well as mitochondrial ETC activity among the two DLBCL subtypes. Specifically, BCR-DLBCLs have greater glycolytic flux typical of the Warburg phenotype. Unlike BCR-DLBCLs, OxPhos-DLBCLs channel the majority of glucose-derived pyruvate into mitochondria, display elevated mitochondrial ETC activity, ATP production, and FAO. Importantly, these metabolic distinctions are associated with subtype-selective survival mechanisms and predictable vulnerabilities. Chapter 3 characterizes the contribution of the mitochondrial translation pathway to the metabolic phenotype of OxPhos-DLBCLs and provides evidence for its pro-survival benefits selective to OxPhos- but not Warburg-type/BCR-DLBCLs. Chapter 4 identifies alterations in mitochondrial morphology and network architecture that are required for increased FAO in OxPhos-DLBCLs without affecting mitochondrial oxidation of other substrates. In summary, the findings described in the following chapters demonstrate

previously unappreciated metabolic heterogeneity in molecular subsets of DLBCLs and uncover BCR-independent survival mechanisms that are linked to mitochondrial FAO, protein translation and network architecture.

REFERENCES

1. Folmes, C.D., et al., *Metabolic plasticity in stem cell homeostasis and differentiation.* Cell Stem Cell, 2012. **11**(5): p. 596-606.

2. Lunt, S.Y. and M.G. Vander Heiden, *Aerobic glycolysis: meeting the metabolic requirements of cell proliferation.* Annu Rev Cell Dev Biol, 2011. **27**: p. 441-64.

3. Stanley, I.A., et al., *Changing appetites: the adaptive advantages of fuel choice.* Trends Cell Biol, 2014. **24**(2): p. 118-27.

4. Kaelin, W.G., Jr. and S.L. McKnight, *Influence of metabolism on epigenetics and disease.* Cell, 2013. **153**(1): p. 56-69.

5. Koppenol, W.H., P.L. Bounds, and C.V. Dang, *Otto Warburg's contributions to current concepts of cancer metabolism.* Nat Rev Cancer, 2011. **11**(5): p. 325-37.

6. Michalek, R.D., et al., *Cutting edge: distinct glycolytic and lipid oxidative metabolic programs are essential for effector and regulatory CD4+ T cell subsets.* J Immunol, 2011. **186**(6): p. 3299-303.

7. Vander Heiden, M.G., L.C. Cantley, and C.B. Thompson, *Understanding the Warburg effect: the metabolic requirements of cell proliferation.* Science, 2009. **324**(5930): p. 1029-33.

8. Possemato, R., et al., *Functional genomics reveal that the serine synthesis pathway is essential in breast cancer.* Nature, 2011. **476**(7360): p. 346-50.

9. Locasale, J.W., et al., *Phosphoglycerate dehydrogenase diverts glycolytic flux and contributes to oncogenesis.* Nat Genet, 2011. **43**(9): p. 869-74.

10. Christofk, H.R., et al., *Pyruvate kinase M2 is a phosphotyrosine-binding protein.* Nature, 2008. **452**(7184): p. 181-6.

11. Israelsen, W.J., et al., *PKM2 isoform-specific deletion reveals a differential requirement for pyruvate kinase in tumor cells.* Cell, 2013. **155**(2): p. 397-409.

12. Ye, J., et al., *Pyruvate kinase M2 promotes de novo serine synthesis to sustain mTORC1 activity and cell proliferation.* Proc Natl Acad Sci U S A, 2012. **109**(18): p. 6904-9.

13. Patel, M.S., et al., *The Pyruvate Dehydrogenase Complexes: Structure-based Function and Regulation.* J Biol Chem, 2014. **289**(24): p. 16615-16623.

14. Hitosugi, T., et al., *Tyrosine phosphorylation of mitochondrial pyruvate dehydrogenase kinase 1 is important for cancer metabolism.* Mol Cell, 2011. **44**(6): p. 864-77.

15. Fan, J., et al., *Tyr phosphorylation of PDP1 toggles recruitment between ACAT1 and SIRT3 to regulate the pyruvate dehydrogenase complex.* Mol Cell, 2014. **53**(4): p. 534-48.

16. Papandreou, I., et al., *HIF-1 mediates adaptation to hypoxia by actively downregulating mitochondrial oxygen consumption.* Cell Metab, 2006. **3**(3): p. 187-97.

17. Kim, J.W., et al., *HIF-1-mediated expression of pyruvate dehydrogenase kinase: a metabolic switch required for cellular adaptation to hypoxia.* Cell Metab, 2006. **3**(3): p. 177-85.

18. Kim, J.W., et al., *Hypoxia-inducible factor 1 and dysregulated c-Myc cooperatively induce vascular endothelial growth factor and metabolic switches hexokinase 2 and pyruvate dehydrogenase kinase 1.* Mol Cell Biol, 2007. **27**(21): p. 7381-93.

19. Caro, P., et al., *Metabolic signatures uncover distinct targets in molecular subsets of diffuse large B cell lymphoma.* Cancer Cell, 2012. **22**(4): p. 547-60.

20. Marin-Valencia, I., et al., *Analysis of tumor metabolism reveals mitochondrial glucose oxidation in genetically diverse human glioblastomas in the mouse brain in vivo.* Cell Metab, 2012. **15**(6): p. 827-37.

21. Gnoni, G.V., et al., *The mitochondrial citrate carrier: metabolic role and regulation of its activity and expression.* IUBMB Life, 2009. **61**(10): p. 987-94.

22. DeBerardinis, R.J., et al., *Beyond aerobic glycolysis: transformed cells can engage in glutamine metabolism that exceeds the requirement for protein and nucleotide synthesis.* Proc Natl Acad Sci U S A, 2007. **104**(49): p. 19345-50.

23. Gao, P., et al., *c-Myc suppression of miR-23a/b enhances mitochondrial glutaminase expression and glutamine metabolism.* Nature, 2009. **458**(7239): p. 762-5.

24. Yuneva, M.O., et al., *The metabolic profile of tumors depends on both the responsible genetic lesion and tissue type.* Cell Metab, 2012. **15**(2): p. 157-70.

25. Wise, D.R., et al., *Hypoxia promotes isocitrate dehydrogenase-dependent carboxylation of alpha-ketoglutarate to citrate to support cell growth and viability.* Proc Natl Acad Sci U S A, 2011. **108**(49): p. 19611-6.

26. Mullen, A.R., et al., *Reductive carboxylation supports growth in tumour cells with defective mitochondria.* Nature, 2012. **481**(7381): p. 385-8.

27. Metallo, C.M., et al., *Reductive glutamine metabolism by IDH1 mediates lipogenesis under hypoxia.* Nature, 2012. **481**(7381): p. 380-4.

28. Nieman, K.M., et al., *Adipocytes promote ovarian cancer metastasis and provide energy for rapid tumor growth.* Nat Med, 2011. **17**(11): p. 1498-503.

29. Carracedo, A., et al., *A metabolic prosurvival role for PML in breast cancer.* J Clin Invest, 2012. **122**(9): p. 3088-100.

30. Tibbetts, A.S. and D.R. Appling, *Compartmentalization of Mammalian folate-mediated one-carbon metabolism.* Annu Rev Nutr, 2010. **30**: p. 57-81.

31. Jain, M., et al., *Metabolite profiling identifies a key role for glycine in rapid cancer cell proliferation.* Science, 2012. **336**(6084): p. 1040-4.

32. Nilsson, R., et al., *Metabolic enzyme expression highlights a key role for MTHFD2 and the mitochondrial folate pathway in cancer.* Nat Commun, 2014. **5**: p. 3128.

33. Lewis, C.A., et al., *Tracing compartmentalized NADPH metabolism in the cytosol and mitochondria of Mammalian cells.* Mol Cell, 2014. **55**(2): p. 253-63.

34. Fan, J., et al., *Quantitative flux analysis reveals folate-dependent NADPH production.* Nature, 2014. **510**(7504): p. 298-302.

35. Wang, J., et al., *Dependence of mouse embryonic stem cells on threonine catabolism.* Science, 2009. **325**(5939): p. 435-9.

36. Alexander, P.B., J. Wang, and S.L. McKnight, *Targeted killing of a mammalian cell based upon its specialized metabolic state.* Proc Natl Acad Sci U S A, 2011. **108**(38): p. 15828-33.

37. Smits, P., J. Smeitink, and L. van den Heuvel, *Mitochondrial translation and beyond: processes implicated in combined oxidative phosphorylation deficiencies.* J Biomed Biotechnol, 2010. **2010**: p. 737385.

38. Kotiadis, V.N., M.R. Duchen, and L.D. Osellame, *Mitochondrial quality control and communications with the nucleus are important in maintaining mitochondrial function and cell health.* Biochim Biophys Acta, 2014. **1840**(4): p. 1254-65.

39. Anand, R., T. Langer, and M.J. Baker, *Proteolytic control of mitochondrial function and morphogenesis.* Biochim Biophys Acta, 2013. **1833**(1): p. 195-204.

40. Rugarli, E.I. and T. Langer, *Mitochondrial quality control: a matter of life and death for neurons.* EMBO J, 2012. **31**(6): p. 1336-49.

41. Lapuente-Brun, E., et al., *Supercomplex assembly determines electron flux in the mitochondrial electron transport chain.* Science, 2013. **340**(6140): p. 1567-70.

42. Cogliati, S., et al., *Mitochondrial cristae shape determines respiratory chain supercomplexes assembly and respiratory efficiency.* Cell, 2013. **155**(1): p. 160-71.

43. Sena, L.A. and N.S. Chandel, *Physiological roles of mitochondrial reactive oxygen species.* Mol Cell, 2012. **48**(2): p. 158-67.

44. Murphy, M.P., et al., *Unraveling the biological roles of reactive oxygen species.* Cell Metab, 2011. **13**(4): p. 361-6.

45. Finkel, T., *Signal transduction by reactive oxygen species.* J Cell Biol, 2011. **194**(1): p. 7-15.

46. Weinberg, F., et al., *Mitochondrial metabolism and ROS generation are essential for Kras-mediated tumorigenicity.* Proc Natl Acad Sci U S A, 2010. **107**(19): p. 8788-93.

47. Gottlieb, R.A. and A.B. Gustafsson, *Mitochondrial turnover in the heart.* Biochim Biophys Acta, 2011. **1813**(7): p. 1295-301.

48. Chen, L., et al., *SYK inhibition modulates distinct PI3K/AKT- dependent survival pathways and cholesterol biosynthesis in diffuse large B cell lymphomas.* Cancer Cell, 2013. **23**(6): p. 826-38.

49. Chen, L., et al., *SYK-dependent tonic B-cell receptor signaling is a rational treatment target in diffuse large B-cell lymphoma.* Blood, 2008. **111**(4): p. 2230-7.

50. Monti, S., et al., *Molecular profiling of diffuse large B-cell lymphoma identifies robust subtypes including one characterized by host inflammatory response.* Blood, 2005. **105**(5): p. 1851-61.

Chapter 2

Metabolic Signatures Uncover Distinct Targets in Molecular Subsets of Diffuse Large B-cell Lymphoma

SUMMARY

Molecular signatures have identified several subsets of Diffuse Large B-cell Lymphoma (DLBCL) and rational targets within the B-cell receptor (BCR) signaling axis. The OxPhos-DLBCL subset, which harbors the signature of genes involved in mitochondrial metabolism, is insensitive to inhibition of BCR survival signaling, but is functionally undefined. We show that compared with BCR-DLBCLs, OxPhos-DLBCLs display enhanced mitochondrial energy transduction, greater incorporation of nutrient-derived carbons into the TCA cycle and increased glutathione levels. Importantly, perturbation of the fatty acid oxidation program and glutathione synthesis proved selectively toxic to this tumor subset. Our analysis provides evidence for distinct metabolic fingerprints and associated survival mechanisms in DLBCL and may have therapeutic implications.

INTRODUCTION

Tumors often rewire their metabolism to ensure a steady supply of intermediary metabolites for synthesis of new biomass, as well as generation of ATP and reducing equivalents [1-3]. This metabolic reprogramming is a dynamic process shaped by oncogenes and tumor suppressors [1, 4, 5]. One of the first metabolic alterations identified in tumors is elevated glycolysis even in the presence of sufficient oxygen. This program, also known as the Warburg effect or aerobic glycolysis, fulfills important biosynthetic needs [1, 6, 7]. The Warburg effect has often been interpreted as an indication of impaired mitochondrial respiration [6]. However, the relevance of mitochondrial respiration in tumors is varied depending on tumor type, and evidence for an oxidative class of tumors and tumors with dual capacity for glycolytic and oxidative metabolism exists [8, 9]. Moreover, the importance of mitochondria in tumor cell survival and proliferation, including utilization of alternative oxidizable substrates such as glutamine and fatty acids has been increasingly appreciated [10-12]. The diversity of carbon substrate utilization pathways in tumors is indicative of metabolic heterogeneity that may not only be relevant across different types of cancer but also manifest within a group of tumors that otherwise share a common diagnosis.

Diffuse Large B-cell Lymphomas (DLBCLs) are a genetically heterogeneous group of tumors and the most common non-Hodgkin lymphomas in adults [13, 14]. However, the spectrum of fuel utilization pathways and the metabolic fingerprints within DLBCL and other similarly heterogeneous groups of tumors have not been fully elucidated. To date, efforts to capture the molecular heterogeneity of DLBCL have relied on gene expression profiling that has uncovered coordinate signaling and survival paradigms in distinct subsets of DLBCL. In one approach, comparison of the genetic signatures across DLBCLs using genome-wide arrays and multiple clustering algorithms captured tumor-intrinsic distinctions in three separate and reproducible clusters [15].

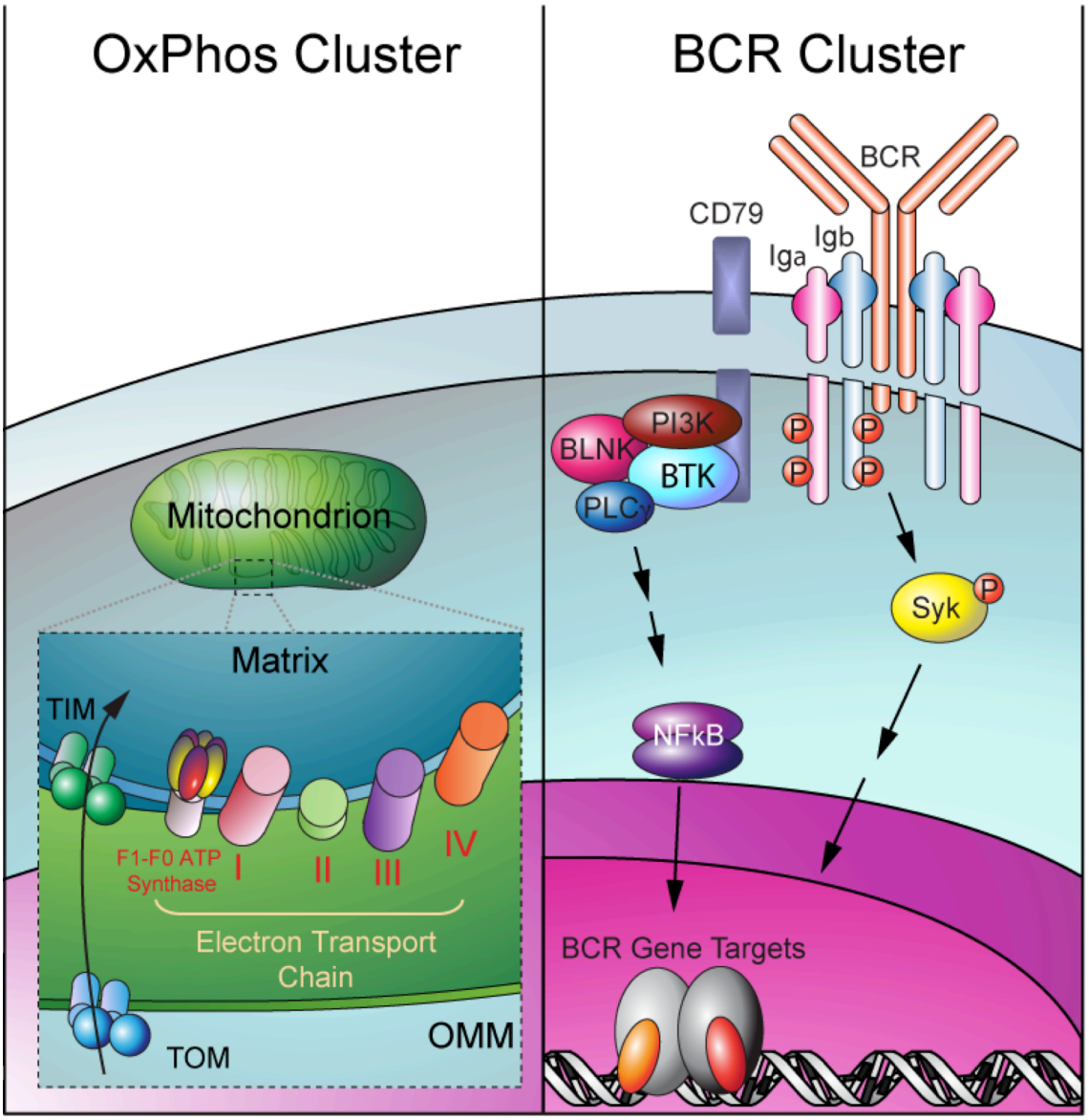

Figure 2.1. Schematic illustration of OxPhos- and BCR-DLBCL subsets identified by consensus cluster classification
Graphics are courtesy of Eric Smith.

Groups of DLBCLs identified by this consensus cluster classification (CCC) scheme are the BCR/proliferation cluster (BCR-DLBCL) displaying up-regulation of genes encoding B-cell receptor (BCR) signaling components, the OxPhos cluster (OxPhos-DLBCL), which is significantly enriched in genes involved in mitochondrial oxidative phosphorylation (OxPhos) (Figure 2.1), and the host response (HR) tumors largely characterized by a brisk host inflammatory infiltrate [15]. Another classification framework known as cell-of-origin (COO) delineated DLBCL subsets that shared components of their transcriptional profiles with normal B-cell subtypes, including Germinal Center B-cell (GCB)-like and Activated B-cell (ABC)-like [16], and a third undefined category, designated “type 3” [17]. CCC and COO classifications capture largely different molecular aspects of DLBCL [15].

Unlike tumors that rely on signaling pathways downstream of the B-cell receptor, OxPhos-DLBCLs do not display active/functional BCR signaling [18]. However, the nature of survival pathways in this group of tumors is not known and beyond the original CCC assignment, the actual functional attributes of the OxPhos molecular signature have not been fully examined. This signature includes multiple subunits of mitochondrial respiratory chain complexes I (NADH dehydrogenase) and V (mitochondrial ATP synthase) that may suggest alterations in mitochondrial energy transduction. However, given the integrative aspect of cellular metabolism and the requirement of both nuclear and mitochondria-encoded genes for proper functioning of the electron transport machinery, the precise metabolic landscape of this molecular subset could not be predicted.

In the present study, we conducted an integrative analysis to dissect the metabolic fingerprints of DLBCL and to delineate subtype-specific differences that may selectively contribute to growth and survival of DLBCL subsets.

RESULTS

Subtype-specific differences in the DLBCL mitochondrial proteome

The up-regulation of select genes encoding for subunits of electron transport chain (ETC) complexes in OxPhos-DLBCLs predicts potential differences in mitochondrial oxidative metabolism compared with other DLBCL groups. However, as ETC activity is linked to the supply of carbon substrates and reducing equivalents, the OxPhos signature is likely part of a broader spectrum of changes in mitochondrial nutrient metabolism that may shed light on the actual functional attributes of an "OxPhos" program in this DLBCL subset. To search for additional components of this metabolic program, we initially performed two dimensional differential gel electrophoresis (2D-DIGE) to compare the proteome of mitochondria purified from representative OxPhos- and BCR-DLBCL cell lines Karpas 422 and OCI-Ly1, respectively [18]. Mitochondrial proteins that were ≥ 2.5 fold more abundant in the OxPhos cell line were identified by mass spectrometry (Figure 2-S1). Among 2D-DIGE candidates were subunits of mitochondrial respiratory chain complex I (NADH dehydrogenase), complex II (succinate dehydrogenase, also a TCA cycle enzyme), complex V (ATP synthase), subunits of the pyruvate dehydrogenase (PDH) complex and several other TCA cycle enzymes, mitochondrial ROS detoxification enzyme manganese superoxide dismutase (MnSOD or SOD2), as well as enzymes involved in mitochondrial β-oxidation of fatty acids and metabolism of ketone bodies and amino acids (Figure 2-S1).

We next wished to interrogate the mitochondrial protein signature defined by 2D-DIGE in a larger panel of OxPhos- and BCR-DLBCL cell lines. This required an independent proteomics approach amenable to multiplexing- isobaric tags for relative and absolute quantification (iTRAQ) (Figure 2-S2) [19, 20] for simultaneous quantitative comparison of multiple unique tryptic peptides per candidate mitochondrial protein across three pairs of OxPhos- and BCR-DLBCL cell lines.

Figure 2.2. Comparison of mitochondrial proteome in OxPhos- and BCR-DLBCLs
(A and B) Multiplex iTRAQ analysis of mitochondria derived from three OxPhos- (Karpas 422, Toledo, and Pfeiffer) and three BCR- (OCI-Ly1, SU-DHL-4, and SU-DHL-6) DLBCL cell lines. Log-log plots of reporter ions abundance ratios vs. reporter ion intensities for proteins detected in replicate nanoflow LC-MS/MS analyses are shown (A). Proteins within the mitochondrial signature that are enriched in OxPhos-DLBCLs are shown as red circles in (A) and grouped per metabolic pathway in (B). Red lines in (A) represent global thresholds based on a ±1.5-fold change between OxPhos and BCR subtypes.

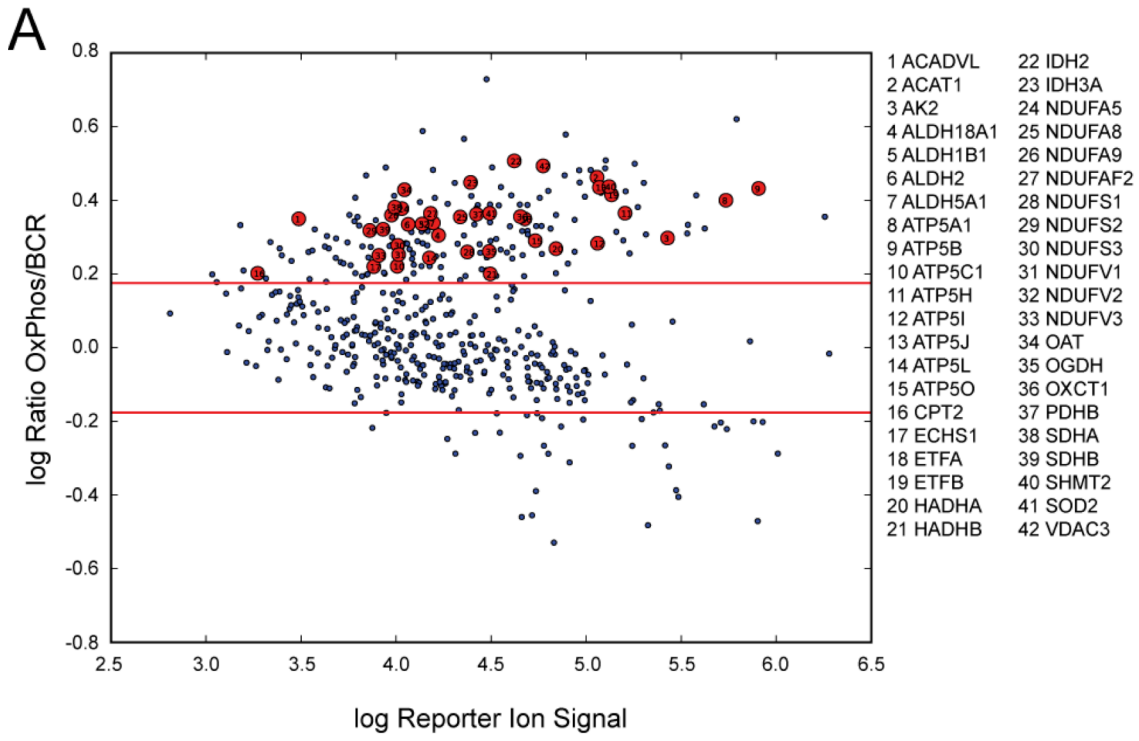

B

TCA Cycle
Pyruvate dehydrogenase (PDH) B
Isocitrate dehydrogenase (IDH) 2 ($NADP^+$)
Isocitrate dehydrogenase (IDH) 3A (NAD^+)
α-Ketoglutarate dehydrogenase (OGDH)
Succinate dehydrogenase (SDH) subunits A and B

Electron Transport and OxPhos Apparatus
Complex I, a subcomplex subunits (NDUFA) 5, 8, 9
Complex I, a subcomplex assembly factor (NDUFAF) 2
Complex I, Fe-S protein (NDUFS) 1, 2, 3
Complex I, flavoprotein (NDUFV) 1, 2, 3
ATP synthase (ATP5) F1 complex subunits
ATP synthase (ATP5) F0 complex subunits

β-Oxidation
Acyl-CoA dehydrogenase (ACAD) VL
Carnitine palmitoyltransferease (CPT) 2
Enoyl-CoA hydratase, short chain (ECHS) 1
Electron-transfer-flavoprotein (ETF) A and B
Hydroxyacyl-CoA dehydrogenase (HADH) A and B

Ketone Body Metabolism
3-oxoacid CoA transferase (OXCT1) 1
Mitochondrial acetoacetyl-CoA thiolase (ACAT1)

Amino Acid and One Carbon Metabolism
Mitochondrial aldehyde dehydrogenase (ALDH) 2
Aldehyde dehydrogenase (ALDH) 1B1
Succinate semialdehyde dehydrogenase (ALDH5A1)
Pyrroline-5-carboxylate synthetase (ALDH18A1)
Mitochondrial serine hydroxymethyltransferase (SHMT2)
Ornithine aminotransferase (OAT)

ROS Detoxification
Manganese Superoxide dismutase (SOD2)

Figure 2.2. (continued)

This analysis confirmed significant quantitative enrichment of mitochondrial β-oxidation enzymes, multiple subunits of respiratory chain complexes, as well as TCA cycle enzymes and MnSOD in OxPhos-DLBCL mitochondria (Figure 2.2 and Table 2.1).

Beyond confirming the differential expression of complex I and V components that were in the original OxPhos-DLBCL cluster signature [15], the 2D-DIGE and iTRAQ proteomic analyses identified additional components of the OxPhos-DLBCL mitochondrial signature that were not fully captured by the previous RNA profile analysis of total tumors. To examine whether these observations could also be substantiated in primary OxPhos-DLBCLs, we examined tumor biopsies for differences in the abundance of these newly identified components of the mitochondrial signature at both protein and RNA levels. The small en bloc primary DLBCL biopsies precluded isolation of tumor mitochondria; however, iTRAQ-based quantification in a limited number of primary cases that produced protein samples of suitable purity and grade for LC-MS/MS indicated increased expression of several TCA cycle and mitochondrial β-oxidation enzymes, as well as MnSOD (Table 2.1). The RNA abundance for candidate components of the mitochondrial proteome signature was also queried in two extensive primary DLBCL expression profile data sets [15, 21] with CCC designations (Tables 2-S1 and 2-S2) and found to be significantly higher in primary OxPhos- than in BCR-DLBCLs in both data sets (Figure 2.3). These observations confirm that the differences in mitochondrial signature identified in DLBCL cell lines translate to primary tumor biopsies.

The functional categories of proteins in the OxPhos-DLBCL mitochondrial signature predict differences in mitochondrial handling of fatty acids and pyruvate, ETC activity, mitochondrial energy production, and ROS content. We next set out to validate each of these predictions.

Table 2.1 OxPhos-DLBCL mitochondrial protein signature in cell lines and primary biopsies

Gene Name	Protein Name	Total Peptides	log Ratio (OxPhos/BCR)	log Intensity	Ratio (OxPhos/BCR)
Mitochondria isolated from DLBCL cell lines					
ACADVL	Very long chain acyl-CoA dehydrogenase	6	0.35	3.49	2.24
ACAT1	Acetoacetyl-CoA thiolase	21	0.46	5.06	2.90
AK2	Adenylate kinase 2	11	0.30	5.43	1.99
ALDH18A1	Aldehyde dehydrogenase 18 family member A1	11	0.31	4.22	2.02
ALDH1B1	Aldehyde dehydrogenase 1 family member B1	7	0.34	4.14	2.16
ALDH2	Mitochondrial aldehyde dehydrogenase 2	9	0.33	4.06	2.16
ALDH5A1	Mitochondrial succinate semialdehyde dehydrogenase	4	0.34	4.20	2.18
ATP5A1	ATP synthase F1 complex alpha subunit 1	26	0.40	5.74	2.51
ATP5B	ATP synthase F1 complex beta polypeptide	27	0.43	5.91	2.71
ATP5C1	ATP synthase F1 complex gamma polypeptide 1	8	0.22	4.01	1.66
ATP5H	ATP synthase F0 complex subunit d	11	0.37	5.20	2.32
ATP5I	ATP synthase F0 complex subunit E	4	0.28	5.06	1.92
ATP5J	ATP synthase F0 complex subunit F6	4	0.44	5.07	2.72
ATP5L	ATP synthase F0 complex subunit G	6	0.24	4.18	1.75
ATP5O	ATP synthase F1 complex subunit O	7	0.29	4.73	1.95
CPT2	Carnitine palmitoyltransferase 2	4	0.20	3.27	1.59
ECHS1	Short-chain enoyl-CoA hydratase 1	5	0.22	3.88	1.66
ETFA	Electron-transfer-flavoprotein alpha polypeptide	8	0.35	4.68	2.24
ETFB	Electron-transfer-flavoprotein beta polypeptide	11	0.42	5.13	2.60
HADHA	Hydroxyacyl-Coenzyme A dehydrogenase alpha subunit	22	0.27	4.84	1.86
HADHB	Hydroxyacyl-Coenzyme A dehydrogenase beta subunit	15	0.20	4.50	1.59
IDH2	Isocitrate dehydrogenase 2 (NADP+)	12	0.51	4.62	3.21
IDH3A	Isocitrate dehydrogenase 3 (NAD+) alpha	6	0.45	4.39	2.81
NDUFA5	NADH dehydrogenase (ubiquinone) 1 alpha subcomplex subunit 5	3	0.38	4.03	2.39
NDUFA8	NADH dehydrogenase (ubiquinone) 1 alpha subcomplex subunit 8	5	0.35	4.34	2.26
NDUFA9	NADH dehydrogenase (ubiquinone) 1 alpha subcomplex subunit 9	6	0.36	3.98	2.29
NDUFAF2	NADH dehydrogenase (ubiquinone) 1 alpha subcomplex assembly factor 2	4	0.36	4.18	2.32
NDUFS1	NADH dehydrogenase (ubiquinone) Fe-S protein 1	9	0.26	4.37	1.82
NDUFS2	NADH dehydrogenase (ubiquinone) Fe-S protein 2	5	0.32	3.86	2.08
NDUFS3	NADH dehydrogenase (ubiquinone) Fe-S protein 3	5	0.28	4.01	1.90
NDUFV1	NADH dehydrogenase (ubiquinone) flavoprotein 1	4	0.25	4.01	1.79
NDUFV2	NADH dehydrogenase (ubiquinone) flavoprotein 2	4	0.34	4.14	2.17
NDUFV3	NADH dehydrogenase (ubiquinone) flavoprotein 3	6	0.25	3.91	1.78
OAT	Ornithine aminotransferase	8	0.43	4.04	2.68
OGDH	Oxoglutarate (alpha-ketoglutarate) dehydrogenase	9	0.26	4.49	1.83
OXCT1	3-oxoacid CoA transferase 1	16	0.36	4.65	2.27
PDHB	Pyruvate dehydrogenase E1 component subunit beta	7	0.36	4.42	2.30
SDHA	Succinate dehydrogenase complex subunit A	3	0.38	3.99	2.41
SDHB	Succinate dehydrogenase complex subunit B	5	0.32	3.93	2.10
SHMT2	Mitochondrial serine hydroxymethyl transferase	20	0.44	5.12	2.74
SOD2	Mitochondrial superoxide dismutase	5	0.36	4.49	2.32
VDAC3	Voltage-dependent anion channel 3	4	0.49	4.77	3.12
Primary DLBCL biopsies					
ALDH2	Mitochondrial aldehyde dehydrogenase 2	7	0.33	3.42	2.12
HADHA	Hydroxyacyl-Coenzyme A dehydrogenase alpha subunit	12	0.20	3.86	1.58
HADHB	Hydroxyacyl-Coenzyme A dehydrogenase beta subunit	11	0.24	3.54	1.73
IDH2	Isocitrate dehydrogenase 2 (NADP+)	15	0.51	3.56	3.23
OXCT1	3-oxoacid CoA transferase 1	5	0.26	3.11	1.83
SOD2	Mitochondrial superoxide dismutase	7	0.25	3.74	1.80

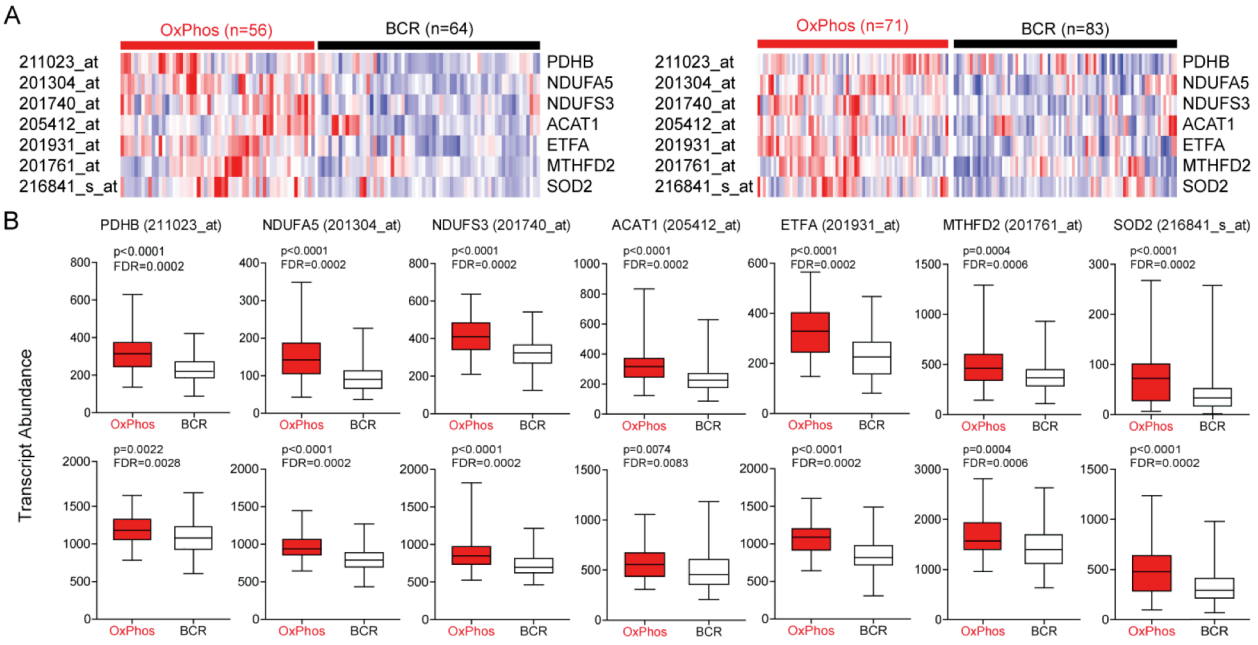

Figure 2.3. Increased abundance of transcripts encoding mitochondrial proteins in primary DLBCL tumor biopsies

(A) Heat map representation of the relative mRNA levels of genes corresponding to the components of the mitochondrial proteome signature using the Monti et al. (left) and Lenz et al. (right) expression array data sets of primary DLBCL cases with OxPhos and BCR consensus cluster assignments. (B) Transcript abundance (probe intensity) of the indicated genes in primary OxPhos- and BCR- DLBCLs from the Monti et al. (top) and Lenz et al. (bottom) data sets. Differential expression was determined by a two-sided Mann Whitney test and p values were corrected for multiple hypothesis testing using the false discovery rate (FDR) procedure. Abbreviations: PDH – pyruvate dehydrogenase; NDUFA5 – NADH dehydrogenase (ubiquinone) 1α subcomplex subunit 5; NDUFS3 – NADH dehydrogenase (ubiquinone) Fe-S protein 3; ETF – electron-transfer-flavoprotein; ACAT – acetoacetyl-CoA thiolase; MTHFD2 – methylenetetrahydrofolate dehydrogenase 2; SOD2 – manganese superoxide dismutase.

Mitochondrial substrate oxidation in DLBCL subsets

To assess potential differences in mitochondrial carbon substrate utilization, mitochondrial oxygen consumption rate (OCR) was measured in real time in the absence or presence of exogenously added substrates such as glucose, glutamine or palmitate using a panel of 3-4 independent OxPhos and "non-OxPhos" DLBCL cell lines. The "non-OxPhos" panel included cell lines with known CCC assignment as BCR-DLBCLs [22] and COO classification as GCB-, ABC-, or Type 3-DLBCLs [16, 17] (Table 2.2). Basal OCR in response to exogenously supplied palmitate was significantly higher in OxPhos-DLBCLs relative to "non-OxPhos" DLBCL cell lines [no substrate (NS) vs. palmitate (Figure 2.4A)]. Basal OCR values per individual DLBCL cell line are shown in Figure 2-S3. The "non-OxPhos" DLBCLs displayed either no increase in OCR or an increase that was significantly less than that observed in the OxPhos-DLBCLs (Figures 2.4A and 2-S3). Importantly, the majority of palmitate-stimulated OCR in OxPhos-DLBCLs was sensitive to the mitochondrial ATP synthase inhibitor oligomycin, indicating that mitochondrial fatty acid oxidation (FAO) in this setting is associated with ATP synthesis (Figures 2.4A and 2-S3). These observations provide quantitative evidence for increased mitochondrial FAO in OxPhos-DLBCLs. Analysis of other oxidizable substrates showed that none of the DLBCL subsets respire on glucose (NS vs. glucose, Figures 2.4A and 2-S3). However, in response to glutamine, all DLBCL subsets exhibited a comparable increase in basal and ATP-associated (oligomycin inhibitable) OCR (NS vs. glutamine, Figures 2.4A and 2-S3). Taken together, comparison of the three carbon substrates across and within DLBCL subsets indicates that palmitate is a predominant respiratory fuel in OxPhos-DLBCLs.

A marked increase in palmitate-induced OCR in OxPhos-DLBCL compared with "non-OxPhos" DLBCL cell lines parallels the absence or presence of functional BCR signaling in these subsets, respectively [18]. This prompted examination of a potential reciprocal relationship between active BCR signaling and mitochondrial FAO.

Table 2.2. CC and COO classification assignments for DLBCL cell lines used in this study

Cell Line	Classification	
	CC	COO
SU-DHL-4	BCR	GCB
SU-DHL-6	BCR	GCB
OCI-Ly1	BCR	GCB
OCI-Ly7	BCR	Type 3
Karpas 422	OxPhos	GCB
OCI-Ly4	OxPhos	Type 3
Pfeiffer	OxPhos	Type 3
Toledo	OxPhos	Type 3
OCI-Ly3	BCR	ABC
OCI-Ly10	BCR	ABC
HBL-1	BCR	ABC
U2932	BCR	ABC

Consensus cluster (CC) and Cell type of origin (COO) classifications for the indicated cell lines have been previously described [18, 22, 33].

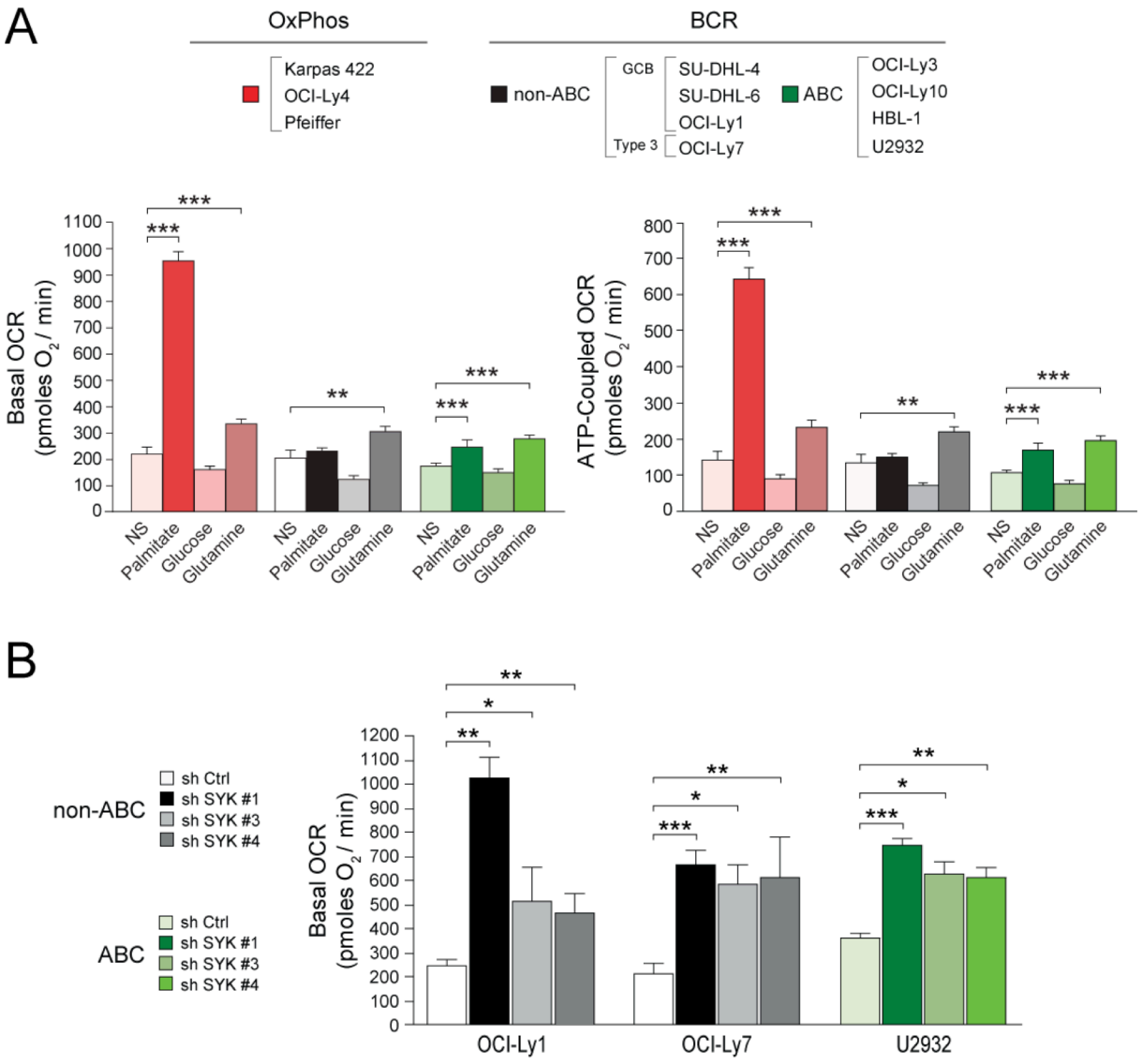

Figure 2.4. Mitochondrial carbon substrate oxidation in DLBCL subsets and its regulation by BCR signaling

(A) Basal (left) and ATP-coupled (right) OCR in DLBCL subsets. OCR values shown are average of all cell lines per DLBCL subtype indicated on top. For each cell line, 7-13 independent OCR measurements were taken. NS denotes no substrate added exogenously. (B) Palmitate-stimulated basal OCR in "non-OxPhos" DLBCL cell lines after acute knockdown of SYK. Error bars, ± SEM. *p < 0.05; **p < 0.01; ***p < 0.001; two-tailed Student's t-test.

Such a scenario would predict that inhibition of BCR signaling in non-OxPhos/BCR DLBCLs may manifest in increased mitochondrial FAO. Indeed, acute interference with BCR signaling using multiple independent shRNAs against SYK or CD79B, upstream components of this signaling axis, was associated with significant elevation of basal palmitate-induced OCR (Figures 2.4B and 2-S4). Notably, OCR measurements were taken after 24 hr treatment with shRNAs, which enabled sufficient depletion of SYK and CD79B (Figure 2-S5 and data not shown) without affecting cell viability (data not shown). These observations suggest an underlying metabolic plasticity that governs the pattern of fuel oxidation in DLBCL subsets.

To provide independent and parallel evidence for differential utilization of fatty acids in DLBCL subsets, a targeted ^{13}C isotopomer approach was undertaken. A total of eight cell lines with known designation as OxPhos or BCR were cultured in media containing uniformly labeled ^{13}C-palmitate (U^{13}C-palmitate), and ^{13}C enrichment was assessed in a defined set of intermediates derived from fatty acid metabolism. The complete oxidation of ^{13}C-palmitate by mitochondria yields 8 acetyl units that can donate carbons to the TCA cycle in the form of citrate labeled on two carbons ($^{13}C2$-citrate), which can in turn lead to the formation of $^{13}C2$-α-ketoglutarate that is in isotopic equilibrium with $^{13}C2$-glutamate (Figure 2.5A). The relative level of ^{13}C enrichment in both $^{13}C2$-citrate and $^{13}C2$-glutamate was significantly higher in the OxPhos-DLBCL cell lines (Figure 2.5B). This is consistent with greater entry of palmitate carbons into the TCA cycle.

In addition to oxidative metabolism for energy production, palmitate may have important biosynthetic roles, including direct incorporation into phosphatidyl choline (PC) to yield U^{13}C-Palmitate-PC (Figure 2.5A). Alternatively, palmitate-derived citrate can be exported from mitochondria and its carbons subsequently incorporated into the head group of PC ($^{13}C2$-Acetyl-PC, Figure 2.5A). In both DLBCL subtypes, direct incorporation of palmitate into PC (U^{13}C-Palmitate-PC) was observed. In addition, a larger enrichment of palmitate carbons in $^{13}C2$-Acetyl-PC was detected in OxPhos cell lines (Figure 2.5B).

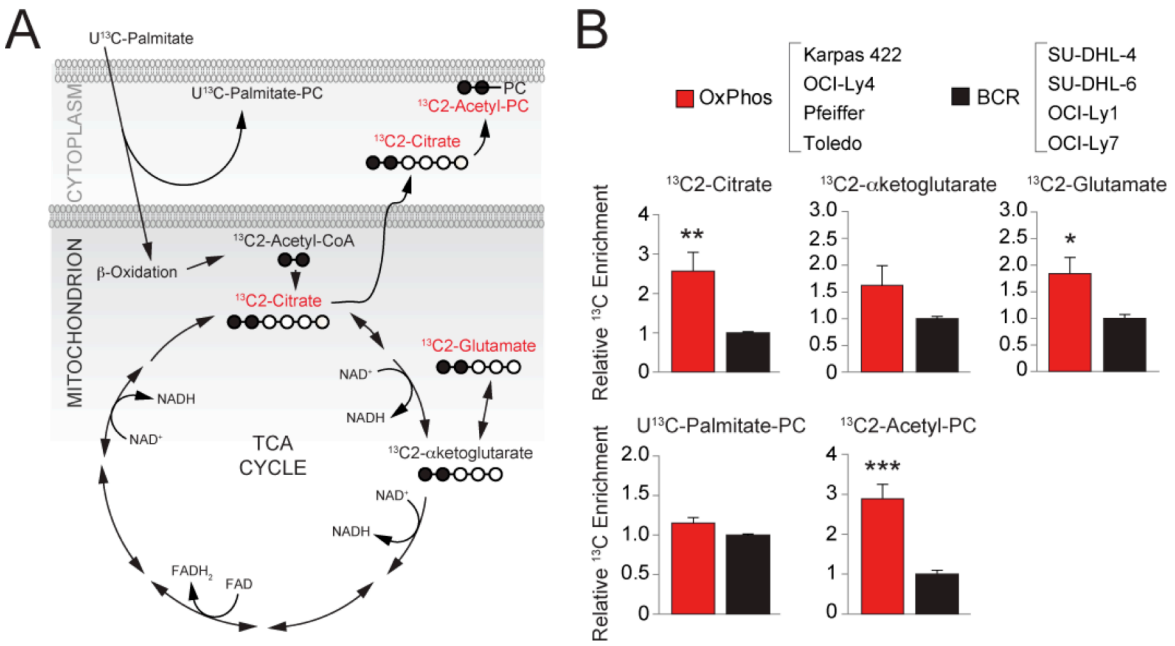

Figure 2.5. Differential fate of palmitate-derived carbons in DLBCL subsets
(A and B) ^{13}C isotopomer analysis of uniformly labeled palmitate ($U^{13}C$-Palmitate). (A) Schematics depicting the number of carbons labeled (filled circles) in a defined set of metabolites derived from palmitate. Metabolites marked in red are selectively elevated in OxPhos-DLBCL cell lines. (B) ^{13}C enrichment in palmitate-derived metabolites. For each metabolite, cumulative data obtained from all four OxPhos-DLBCL cell lines are shown relative to the mean value of that metabolite in all four BCR-DLBCL cell lines listed on top. Error bars, ± SEM. *p < 0.05; **p < 0.01; ***p < 0.001; two-tailed Student's t-test.

Figure 2.6. Effect of palmitate metabolism on DLBCL proliferation and survival
(A) Effect of palmitate supplementation on the proliferation of DLBCL cell lines. Control denotes serum-free media containing all amino acids except L-glutamine. (B) Effects of acute bromocrotonic acid treatment on palmitate-stimulated basal OCR in DLBCL cell lines. The indicated cell lines were treated with 7.5 μM bromocrotonic acid (BrCA) for 4 hr and basal OCR was measured in response to palmitate as the only exogenously added substrate. (C) Survival of DLBCL subsets cultured in the absence or presence of BrCA for 24 hr. Error bars, ± SEM. **p < 0.01; ***p < 0.001; two-tailed Student's t-test.

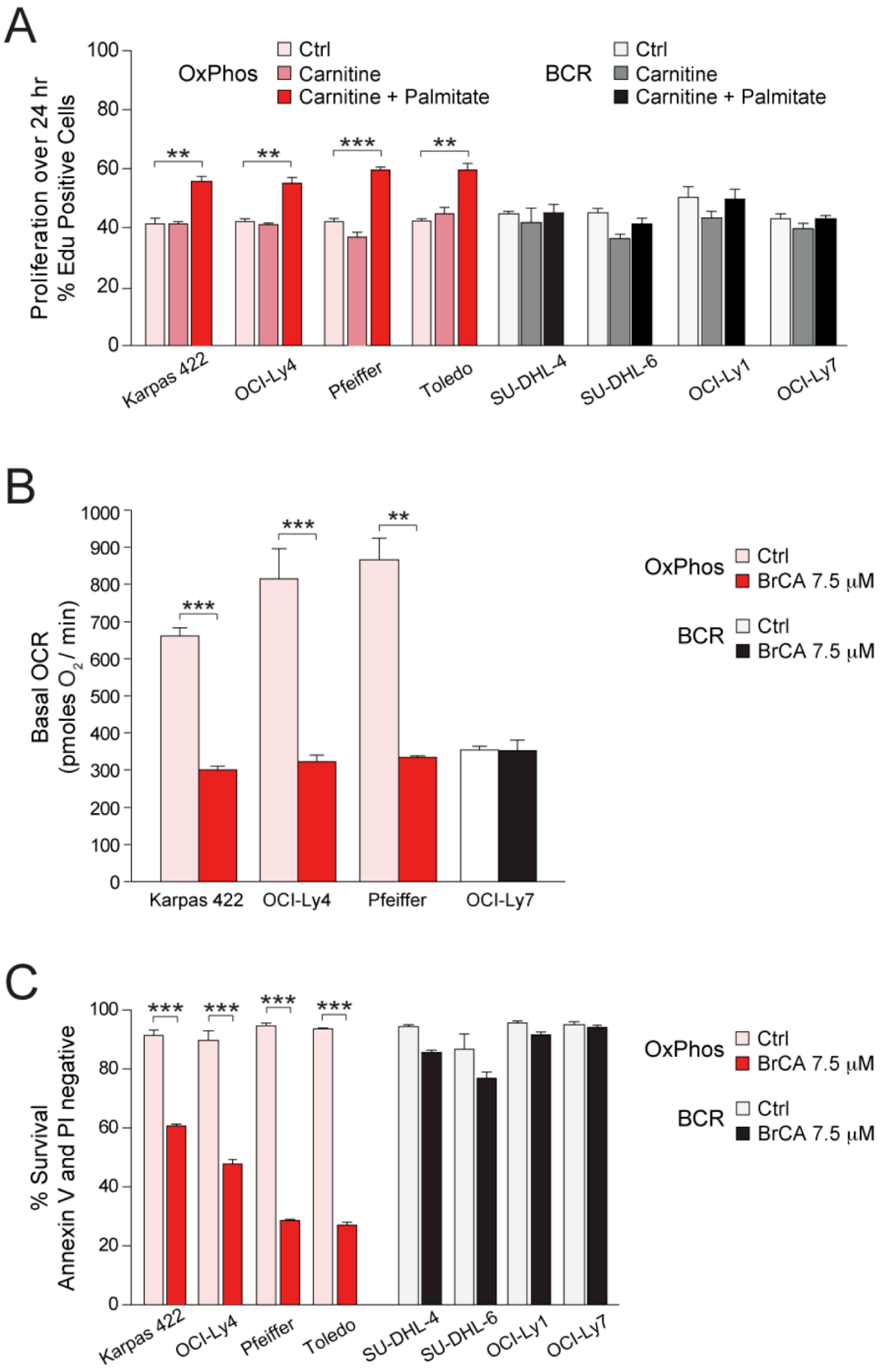

Figure 2.6. (continued)

A preferential increase in palmitate utilization in OxPhos-DLBCLs prompted examination of its effect on proliferation in these cells. Supplementation of serum-free media containing amino acids with palmitate and carnitine led to a modest but significant and selective increase in the proliferation of OxPhos-DLBCLs (Figure 2.6A). In the absence of palmitate, carnitine, which is required for mitochondrial import of long-chain fatty acids, did not influence proliferation (Figure 2.6A).

To probe the pro-survival benefit of mitochondrial FAO in DLBCL subsets, this program was inhibited using 4-bromocrotonic acid (BrCA), which irreversibly inhibits mitochondrial β-oxidation of both long- and short-chain fatty acids [23]. Acute treatment of DLBCL cell lines (4 hr) with BrCA interfered with palmitate stimulation of basal OCR in OxPhos-DLBCL cell lines (Figure 2.6B), while longer treatment (24 hr) was selectively toxic to this subset compared with BCR-DLBCLs (Figure 2.6C). These results suggest that the mitochondrial FAO program provides pro-survival benefits to OxPhos-DLBCLs.

Programmatic regulation of Fatty Acid Oxidation and its relevance to OxPhos-DLBCL survival

The concomitant increase in the abundance of several mitochondrial FAO enzymes in OxPhos-DLBCLs is consistent, at least in part, with a programmatic increase in the transcriptional regulation of this pathway. These observations warranted systematic interrogation of the primary DLBCL transcript data sets for the prevalence of a defined list of transcriptional regulators of this pathway. Nuclear receptor peroxisome proliferator-activated receptor (*PPAR*) γ transcripts were found to be significantly more abundant in primary OxPhos-DLBCLs in two independent cohorts of DLBCL tumors (Figure 2.7A).

Figure 2.7. Programmatic regulation of FAO and its relevance to DLBCL survival
(A) Increased transcript abundance of *PPARγ* in the Monti et al. (left) and Lenz et al. (right) data sets of primary DLBCL cases with OxPhos and BCR consensus cluster assignments. Differential expression was determined by a two-sided Mann Whitney test and p-values were corrected for multiple hypothesis testing using the false discovery rate (FDR) procedure. (B) Effect of siRNA-mediated depletion of PPARγ on the survival of DLBCL subsets. (C and D) Survival of the indicated DLBCL cell lines cultured in the absence or presence of increasing concentrations of PPARγ antagonists (C) T0070907 or (D) GW9662 for 96 hr. Error bars, ± SEM. **p < 0.01; ***p < 0.001; two-tailed Student's t-test.

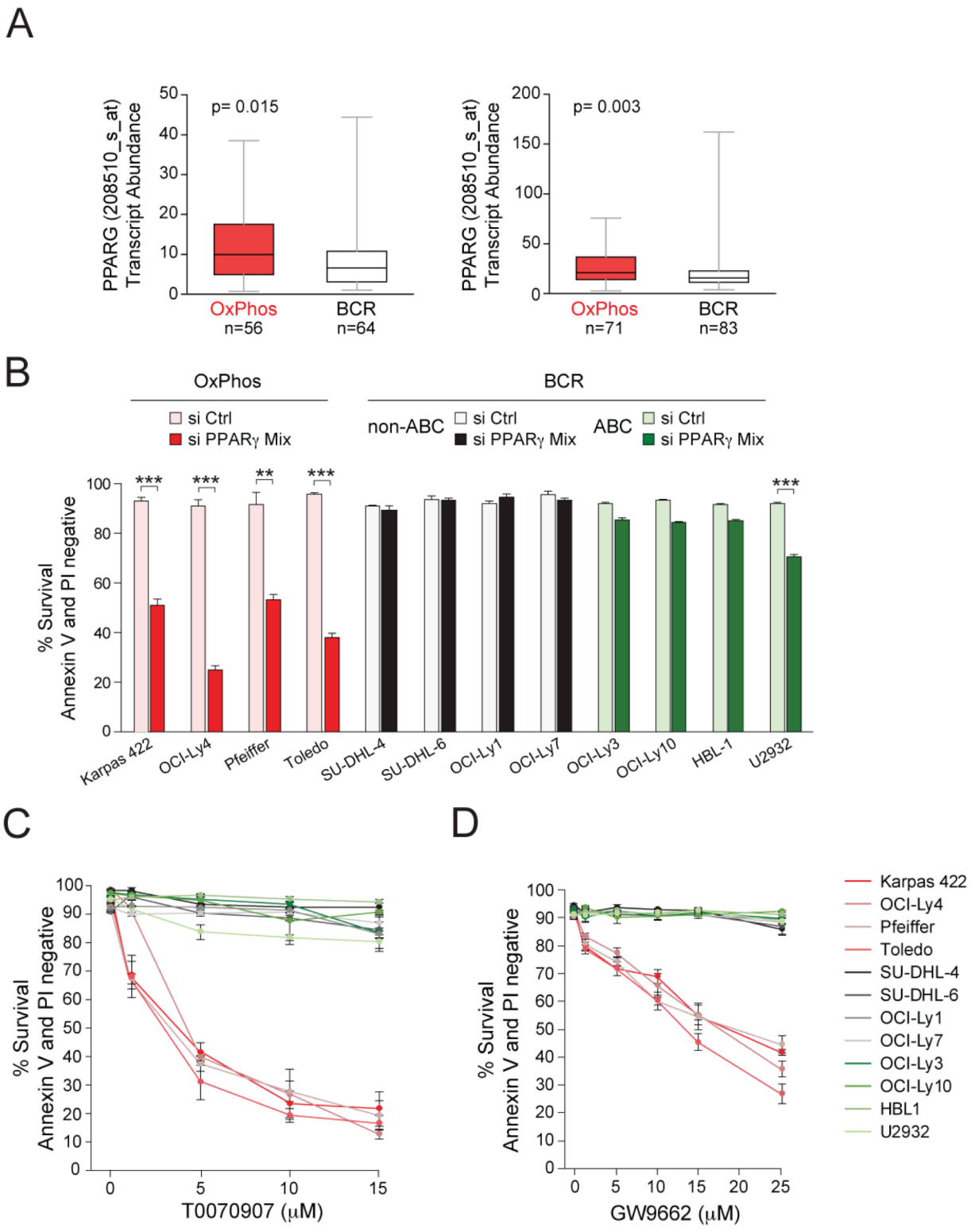

Figure 2.7. (continued)

Importantly, several enzymes identified in the mitochondrial protein signature of OxPhos-DLBCLs such as ETF, ACAD and HADH, as well as multiple subunits of mitochondrial respiratory chain complexes I, II, and ATP synthase are downstream targets of PPARγ [24]. To probe the functional relevance of PPARγ in DLBCL subsets, we tested the effect of its depletion using three independent siRNAs and their corresponding mixture (Figures 2.7B and 2-S6A). The most robust decrease in PPARγ protein levels was achieved using the siRNA mix (Figure 2-S6B) and was accompanied by significant apoptosis in OxPhos-DLBCLs compared with the BCR subset (Figure 2.7B).

To provide a pharmacologic correlate to these findings, we also tested the effect of two selective PPARγ antagonists T0070907 and GW9662 [25, 26]. Short term treatment of DLBCL cell lines with these compounds blocked palmitate stimulation of OCR (data not shown). Upon longer incubation periods (96 hr), these compounds proved selectively toxic to OxPhos-DLBCLs (Figures 2.7C and 2.7D). The above genetic and pharmacologic approaches to PPARγ inhibition complement and extend the results shown in Figure 2.6C that pharmacologic inhibition of the mitochondrial β-oxidation program is toxic to OxPhos-DLBCLs, and are collectively congruent with the idea that a sustained mitochondrial FAO program may be relevant for the survival of OxPhos-DLBCLs.

Differential utilization of glucose-derived carbons in DLBCL subsets

Identification of PDH as a component of the mitochondrial proteome signature in OxPhos-DLBCLs predicts differential mitochondrial handling of pyruvate. Indeed, biochemical analysis of isolated mitochondria derived from a panel of DLBCL cell lines indicated a significant increase in PDH enzyme activity in OxPhos-DLBCLs (Figure 2.8A). Increased PDH activity would further predict diminished availability of glucose-derived pyruvate for lactate synthesis. Biochemical quantification of glucose-derived lactate, secreted by OxPhos-DLBCL cell lines compared to

"non-OxPhos"/BCR counterparts, indicated that this is indeed the case (Figure 2.8A). These observations prompted a more detailed examination of the fate of glucose carbons in DLBCL subsets.

Beyond generation of pyruvate, glucose-derived metabolites are central to several biosynthetic pathways (Figures 1.1 and 2.8B). For example, glucose-6-phosphate can enter the pentose phosphate pathway to yield ribose sugars for nucleic acid synthesis and NADPH generation for lipid synthesis and ROS detoxification [3, 7]. Dihydroxyacetone phosphate, which is in equilibrium with glyceraldehyde-3-phosphate, is used in glycerol synthesis, providing a necessary backbone for membrane phospholipids. Finally, glucose-derived citrate and aspartate, a surrogate for oxaloacetate (OAA), can be used in lipid and nucleotide synthesis, respectively. To examine differences in the terminal fate of glucose-derived pyruvate and the branch points at which glucose carbons divert to biosynthetic pathways in different DLBCL subsets, we carried out a targeted ^{13}C isotopomer analysis using uniformly labeled ^{13}C-glucose ($U^{13}C$-glucose).

Glucose uptake was comparable in DLBCL cell lines as evident from the similar levels of remaining $U^{13}C$-glucose in the media following 8 hr incubation (Figure 2.8C). The BCR cell lines displayed a larger contribution of glucose-derived carbons to the synthesis of pentose sugars compared with the OxPhos cell lines ($U^{13}C$-pentose, Figure 2.8C). This is consistent with reduced levels of $U^{13}C$-glucose-6-phosphate precursor observed in this subset (Figure 2.8C), provided that the oxidative branch of the pentose phosphate pathway is utilized to derive pentose sugars. In addition, the contribution of glucose carbons to glycerol incorporation into PC was significantly higher in BCR cell lines (^{13}C-glycerol-PC, Figure 2.8C).

The overall glycolytic capacity was assessed by comparing both intracellular and extracellular (secreted) $U^{13}C$-lactate and $U^{13}C$-alanine (a surrogate for pyruvate). BCR cell lines had significantly higher intracellular and secreted $U^{13}C$-alanine and $U^{13}C$-lactate (Figure 2.8C).

Figure 2.8. Utilization of glucose-derived carbons in DLBCL subsets
(A) PDH enzyme activity (top) and lactate production from glucose (bottom) in DLBCL subsets. Data are cumulative from independent DLBCL cell lines listed on top. (B-C) ^{13}C isotopomer analysis of uniformly labeled glucose ($U^{13}C$-glucose). (B) Schematics depicting the number of carbons labeled (filled circles) in intermediary metabolites of glucose metabolism. (C) ^{13}C enrichment in glucose-derived metabolites. For each metabolite, cumulative data obtained from all four OxPhos-DLBCL cell lines (Karpas 422, OCI-Ly4, Pfeiffer and Toledo; red bars) are shown relative to the mean value of that metabolite in all four BCR-DLBCL cell lines (SU-DHL-4, SU-DHL-6, OCI-Ly1 and OCI-Ly7; black bars). Error bars, ± SEM. *$p < 0.05$; **$p < 0.01$, ***$p < 0.001$; two-tailed Student's *t*-test.

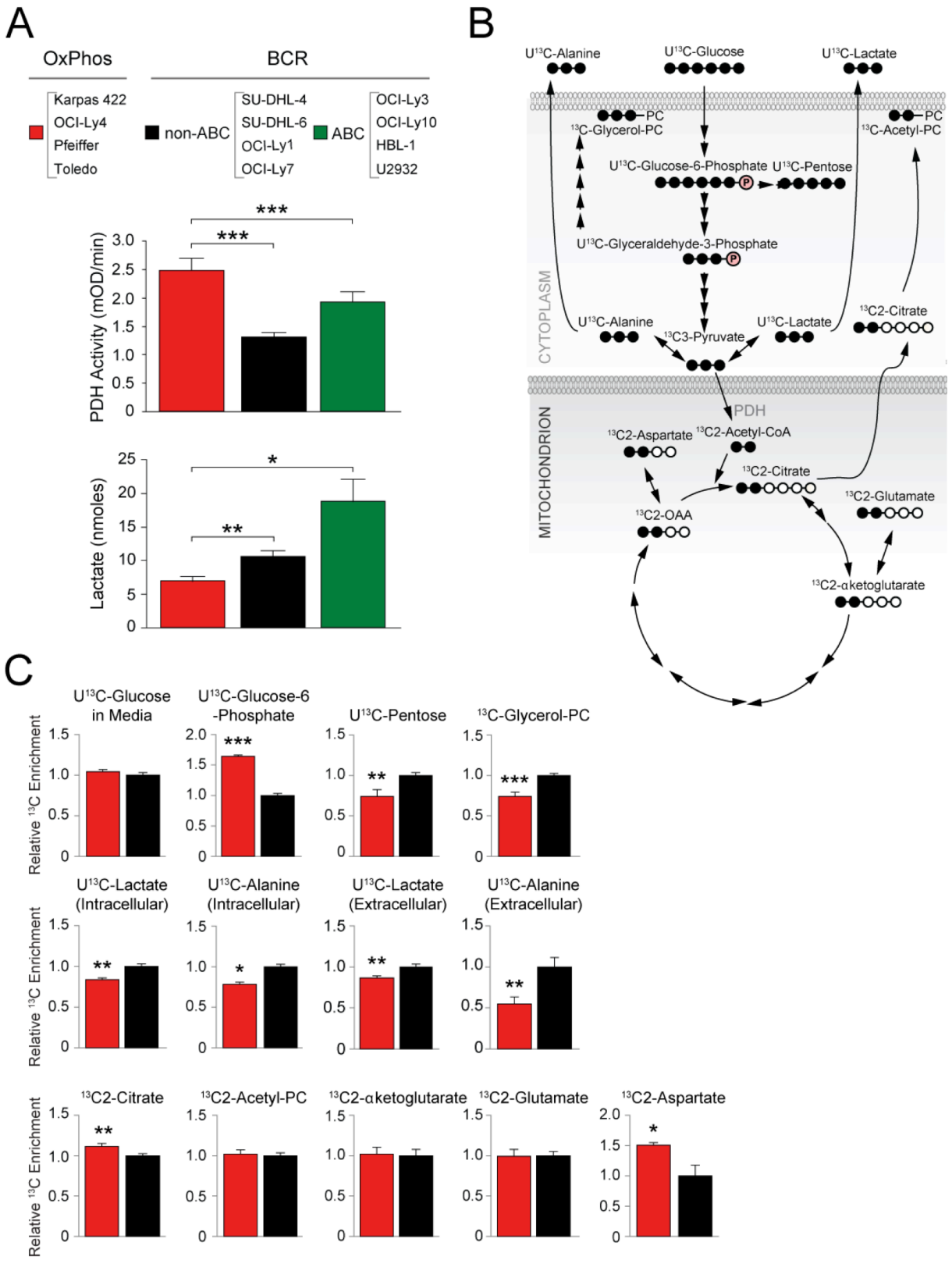

Figure 2.8. (continued)

These data are consistent with biochemical evidence that glucose-derived lactate is higher in these cells (Figure 2.8A), suggesting a higher glycolytic flux.

Glucose-derived pyruvate can enter the TCA cycle through a PDH-catalyzed reaction yielding citrate or through a pyruvate carboxylase (PC)-mediated anaplerotic reaction that generates OAA [27]. The ratio of PDH and PC activities in tumors is variable [27, 28], suggesting significant diversity and tumor type specificity in the mode of TCA cycle entry of glucose-derived carbons. The PDH reaction can be traced by the pattern of carbon labeling in citrate as ^{13}C2-citrate. The relative ^{13}C enrichment in this metabolite was significantly higher in OxPhos cell lines (Figure 2.8C), indicating a greater overall diversion of glucose carbons to the TCA cycle. Elevated PDH-catalyzed formation of ^{13}C2-citrate in OxPhos-DLBCLs is consistent with increased levels of PDH and enzyme activity in this subset. Among other TCA cycle intermediates measured in this analysis, ^{13}C enrichment in aspartate (surrogate for OAA) was relatively higher in OxPhos compared with BCR cell lines (^{13}C2-asparate, Figure 2.8C).

Despite elevated PDH activity in OxPhos-DLBCLs and higher enrichment of glucose carbons in the aforementioned TCA cycle intermediates, glucose is not fully oxidized to stimulate mitochondrial OCR in these cells (Figures 2.4A and 2-S3). This may be due to greater diversion of glucose-derived TCA intermediates to biosynthetic pathways. Overall, the distinct enrichment patterns of carbons in glucose-derived metabolites indicate relative diminution of lactate production in OxPhos-DLBCL and an attendant increase in the entry of glucose carbons in the TCA cycle via citrate.

Contribution of mitochondrial metabolism to cellular ATP budget in DLBCL subsets

The observed differences in utilization of palmitate- and glucose-derived carbons as well as ATP generation through mitochondrial oxidation of palmitate (ATP-coupled respiration) in DLBCL subsets warranted comparison of mitochondrial and non-mitochondrial contributions to the cellular energy budget.

Figure 2.9. Contribution of mitochondrial metabolism to cellular ATP and energy transduction in DLBCL subsets

(A) Percent contribution of glycolysis and mitochondrial metabolism to total cellular ATP. For each subtype, cumulative data from four OxPhos-DLBCL (Karpas 422, OCI-Ly4, Pfeiffer, and Toledo) and four BCR-DLBCL (SU-DHL-4, SU-DHL-6, OCI-Ly1, and OCI-Ly7) cell lines are shown. (B) Mitochondrial ATP synthesis rate. Cumulative data from four OxPhos-DLBCL (red bar) and four BCR-DLBCL (black bar) cell lines are shown as in (A). (C) Average copy number of 110 mitochondrial SNP probes for 39 primary OxPhos-DLBCL and 33 primary BCR-DLBCL cases. Differences were tested using a Man-Whitney U-test and found to be non-significant. (D-F) OCR in isolated mitochondria in different respiratory states. (D) Schematics of mitochondrial respiratory complexes and substrates as well as mitochondrial inhibitors used to measure their specific activities. (E) Representative OCR traces in mitochondria isolated from DLBCL cell lines indicating respiratory states examined. (F) OCR in isolated mitochondria measured using complex I- or complex II-linked substrates. Data are derived from four cell lines per DLBCL subset listed on top. Error bars in A, B and F, ± SEM. **$p < 0.01$; ***$p < 0.001$; two-tailed Student's *t*-test.

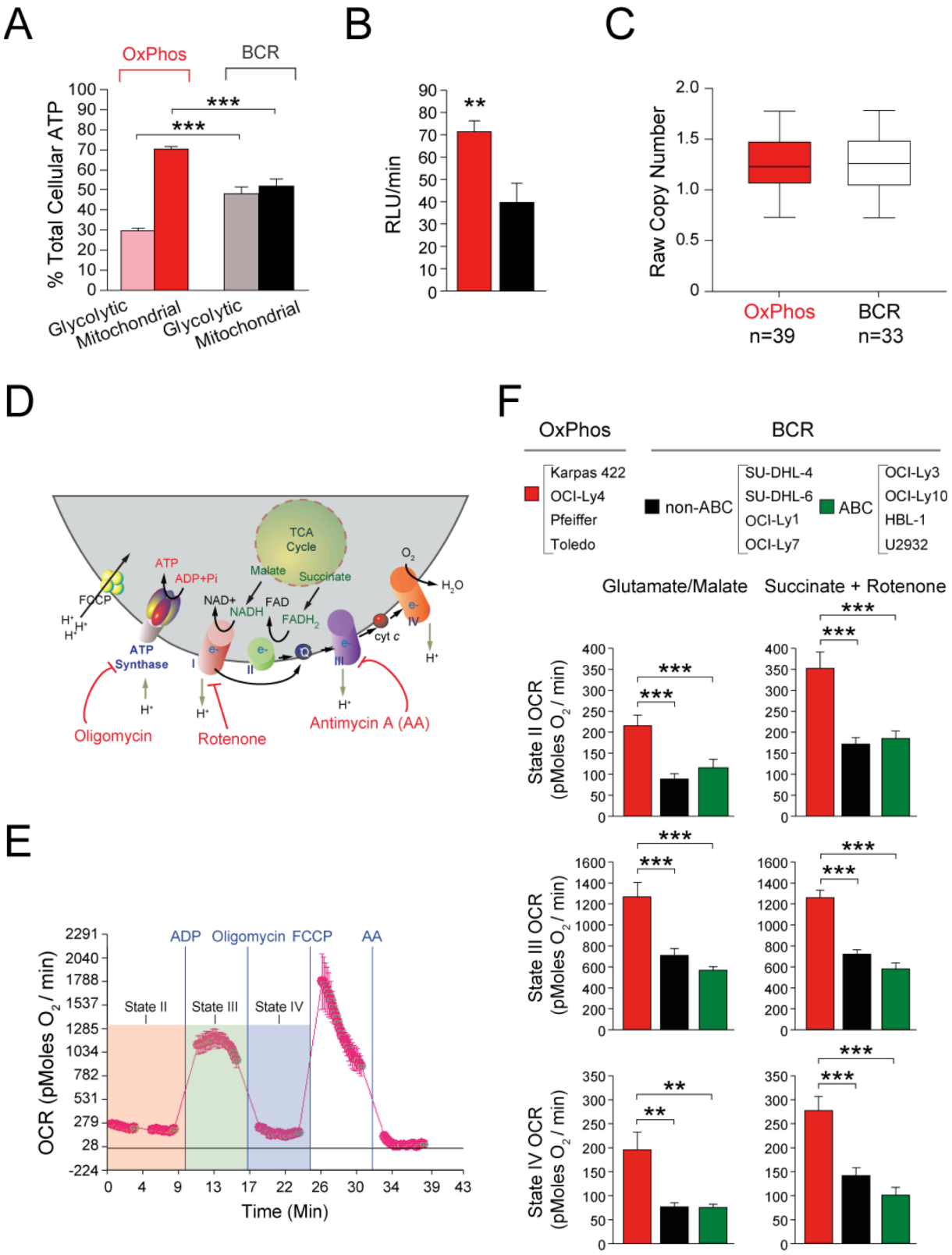

Figure 2.9. (continued)

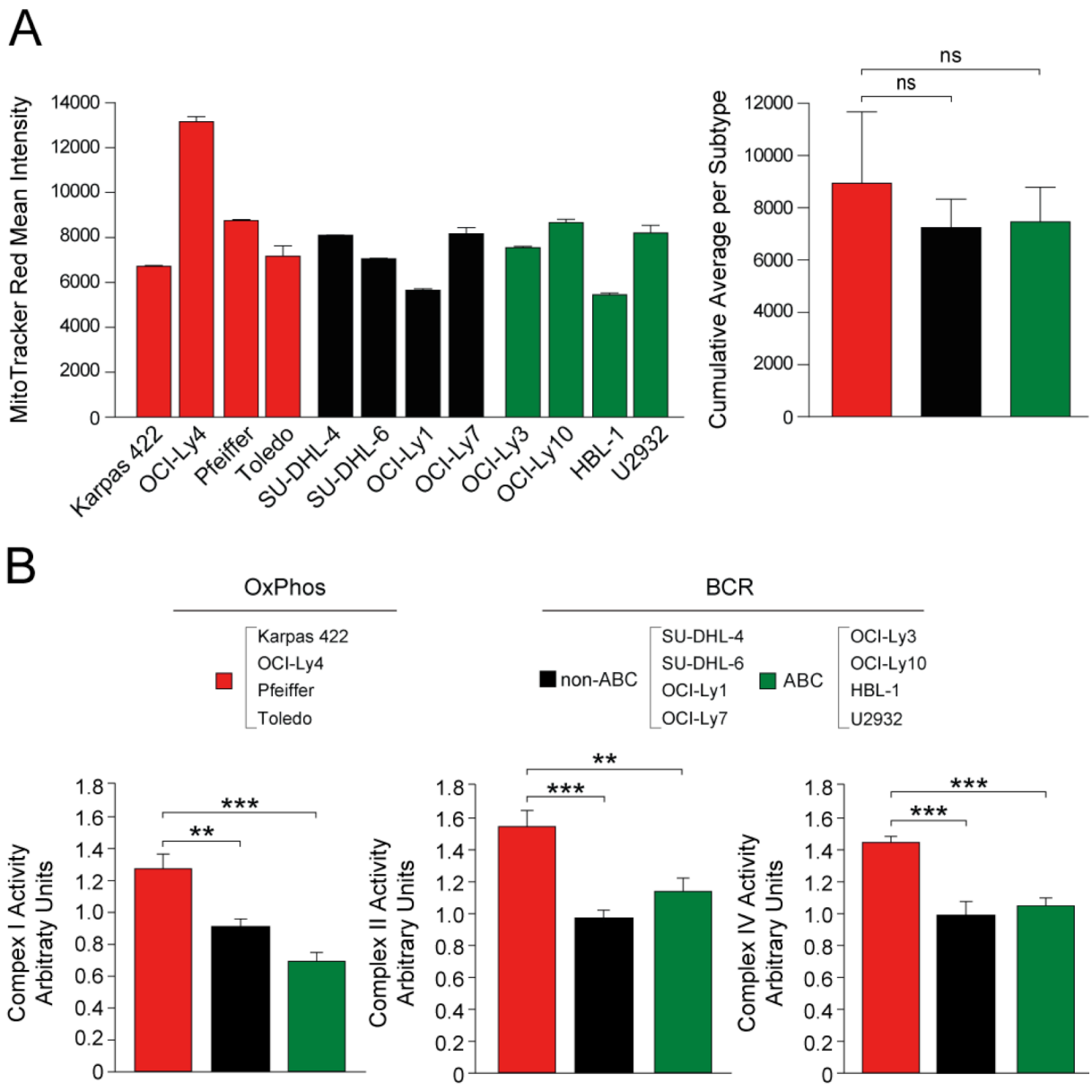

Figure 2.10. Mitochondrial content and electron transport chain activity in DLBCL cell lines

(A) Mitochondrial content in DLBCL cell lines measured using MitoTracker Red. Values per individual cell line (left) and cumulative average per subtype (right) are shown. (B) Activity of respiratory chain complexes I (NADH dehydrogenase), II (succinate dehydrogenase) and IV (cytochrome c oxidase) in mitochondria isolated from four independent DLBCL cell lines per subtype (listed on top) using immune-capture-based enzyme activity assays (MitoScience, Eugene, OR). The amount of mitochondria used was 100 μg for complexes I and IV and 10 μg for complex II activity measurements. Data show cumulative values from 4-8 independent experiments with 3-4 replicates for each cell line. Error bars, ± SEM. ns, non-significant; **p < 0.01, ***p < 0.001; two-tailed Student's t-test.

To this end, the portion of total cellular ATP that is sensitive to inhibition of glycolysis versus mitochondrial metabolism was assessed [29]. Compared to BCR-DLBCLs, the OxPhos subset derives a significantly higher portion of its total energy (~70%) from mitochondrial oxidative metabolism than from glycolysis (Figure 2.9A). The higher contribution of mitochondria to total cellular ATP in OxPhos-DLBCLs is concordant with increased expression of mitochondrial ATP synthase (complex V) subunits (Figures 2.2, 2-S1 and Table 2.1), and an elevated rate of mitochondrial ATP synthesis in OxPhos-DLBCL cell lines (Figure 2.9B). These observations could potentially be explained by differences in mitochondrial content in DLBCL subtypes. However, assessment of the steady state content of mitochondria in DLBCL cell lines did not reveal any subtype-specific differences (Figure 2.10A). In addition, mitochondrial SNP copy number analysis in a cohort of primary biopsies with OxPhos or BCR assignments did not reveal any differences (Figure 2.9C). Consistent with the significant mitochondrial contribution to total cellular energy budget in OxPhos-DLBCLs, the survival of this subtype was selectively sensitive to hypoxia, which limits mitochondrial function and diminishes oxidative phosphorylation (Figure 2.11A). Conversely, viability in galactose containing media, which forces cells to use oxidative phosphorylation over glycolysis, was maintained in OxPhos-DLBCL cells but was significantly compromised in the more glycolytic BCR-DLBCL subset (Figure 2.11B).

Increased contribution of mitochondria to total cellular ATP may not only reflect distinct channeling of carbon substrates in mitochondria but also differential activity or efficiency of mitochondrial ETC complexes. Studies in isolated mitochondria derived from DLBCL cell lines enabled direct assessment of mitochondrial respiration at the organelle level independent of the cytosolic processing of carbon substrates. Mitochondrial respiratory states were assessed using glutamate/malate and succinate as complex I- and II-linked substrates, respectively (Figures 2.9D and 2.9E). When measuring complex II activity, rotenone was included with succinate to inhibit the reverse flow of electrons to complex I. Respiratory rates in the presence of substrate alone (also known as state II respiration) were higher in OxPhos-DLBCL mitochondria

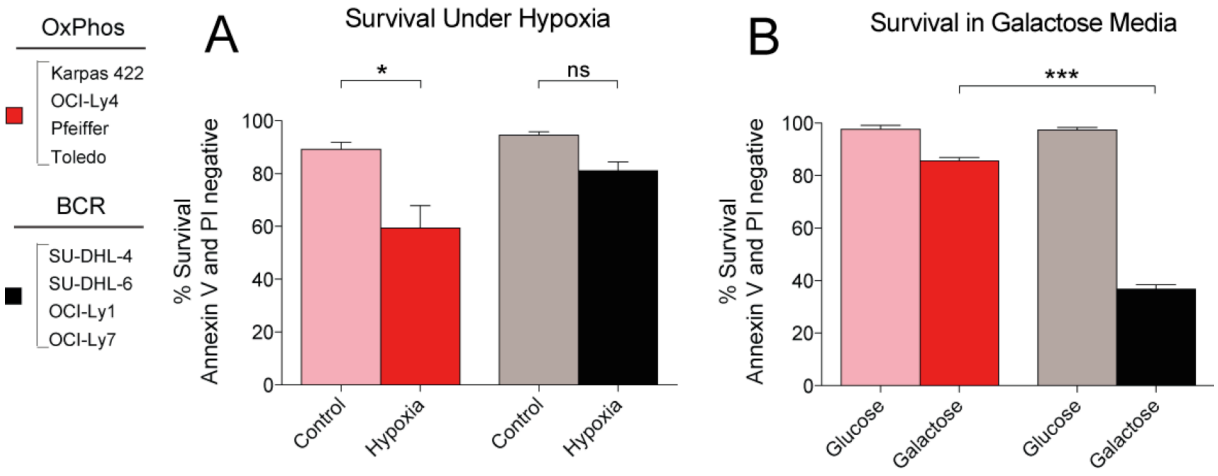

Figure 2.11. Differential sensitivity of DLBCL cell lines to hypoxia and galactose
(A) Viability of DLBCL cell lines after incubation for 72 hr in 1% O_2. (B) Viability of DLBCL cell lines grown in serum-free RPMI containing 2 g/L D-glucose or 2 g/L D-galactose for 72 hr. Error bars, ± SEM. *p <0.05; ***p < 0.001; two-tailed Student's t-test.

(Figure 2.9F). Addition of ADP which mimics a state of energy demand driving high rates of respiration (also known as state III respiration) elicited significantly higher OCR in OxPhos-DLBCL mitochondria supplied with either complex I or II substrates (Figure 2.9F). This increased respiration is used for ATP synthesis and is sensitive to oligomycin. Accordingly, OCR values in the presence of substrate, ADP and oligomycin (state IV respiration) were also significantly higher in OxPhos- compared with BCR-DLBCLs (Figure 2.9F). These results provide a direct link between the OxPhos signature and an actual quantitative increase in ETC activity in this DLBCL subset. Moreover, independent biochemical measurements of mitochondrial complex I, II and IV in immunocapture assays provided corroborative biochemical evidence for significant elevation of these enzyme activities in OxPhos-DLBCLs (Figure 2.10B). In aggregate, our observations both at the level of intact cells (Figures 2.4A, 2.9A, 2.9B and 2.11) and isolated mitochondria (Figures 2.9F and 2.10B) demonstrate that the OxPhos signature captures a program of mitochondrial metabolism and energy transduction that is selectively activated in this DLBCL subset.

The relevance of ROS content and glutathione synthesis in DLBCL subtypes

Mitochondria are a predominant source of reactive oxygen species (ROS). While ROS signaling is important for a myriad of cellular functions, excessive mitochondrial superoxide can damage mtDNA, modify proteins and lipids, and inhibit aconitase activity, thus limiting oxidative phosphorylation. Elevated ETC activity in OxPhos-DLBCLs, particularly of complex I, predicted increased accumulation of mitochondrial superoxide. However, MnSOD is also concomitantly elevated in this subset (Figures 2.2, 2.3, and 2-S1), potentially as a mechanism to counteract the increased burden of mitochondrial superoxide. Efficient clearance of ROS would also ensure that oxidative phosphorylation could remain elevated in OxPhos-DLBCLs. Assessment of mitochondrial superoxide using MitoSOX Red revealed lower steady state levels in OxPhos-DLBCLs (Figure 2.12A, left panel).

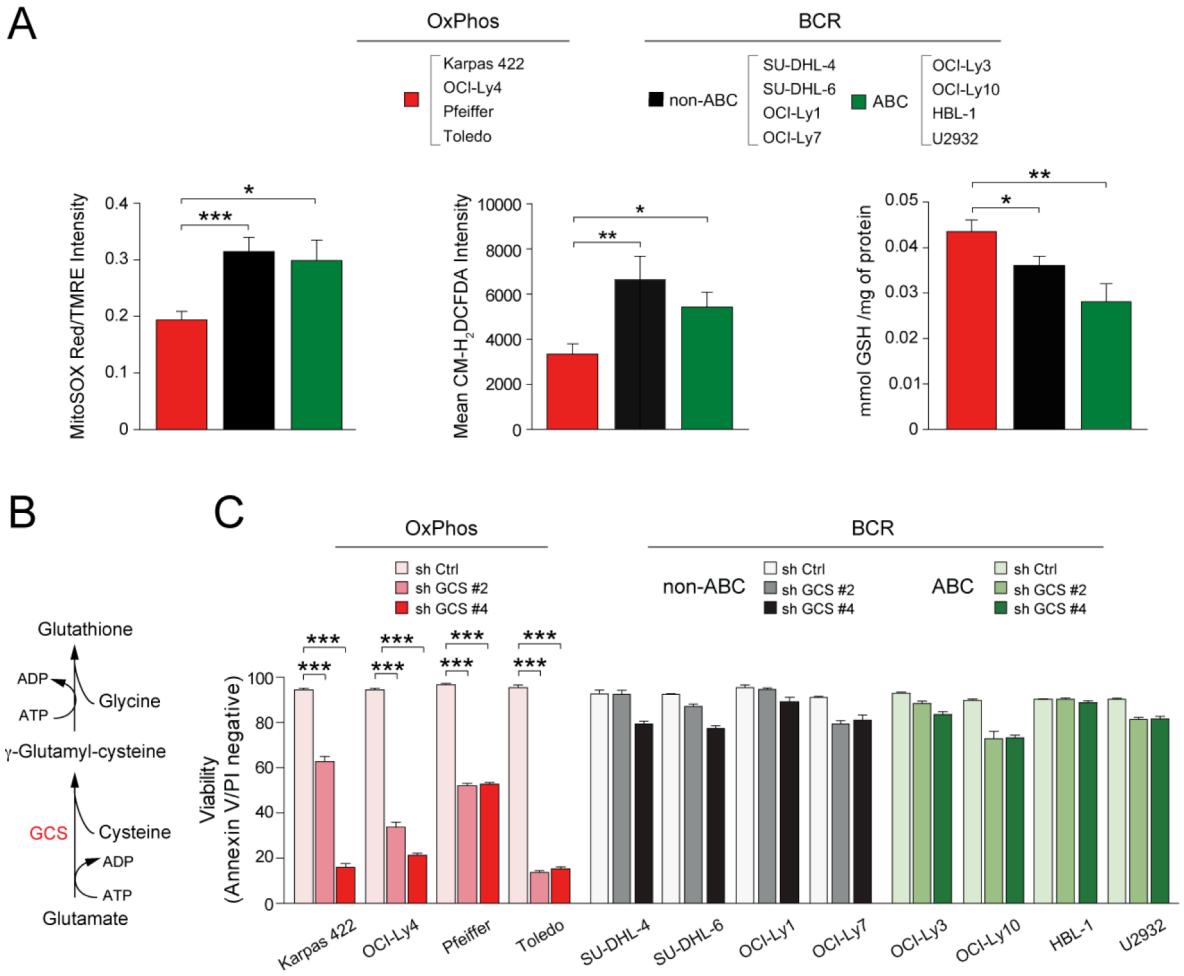

Figure 2.12. Differential contribution of ROS detoxification to survival of DLBCL subsets

(A) Mitochondrial superoxide (left), total cellular ROS (middle) and GSH (right) levels in DLBCL subtypes. Data are derived from four cell lines per DLBCL subset listed on top. (B-C) *De novo* GSH synthesis pathway (B) and the effect of GCS depletion on DLBCL survival. Cell viability was assessed 72 hr after knockdown. GCS, γ-glutamyl cysteine synthase. Error bars, ± SEM. *p < 0.05; **p < 0.01, ***p < 0.001; two-tailed Student's *t*-test.

These observations were further integrated with the total cellular ROS levels using CM-H_2DCFDA, a fluorescent probe that is sensitive to oxidation by peroxyl, alkoxyl, peroxynitrite, $NO2^{\cdot}$, $CO3^{\cdot -}$, and $OH^{\cdot}$ radicals and can thus serve as an indicator of overall "oxidative stress". The CM-H_2DCFDA signal intensity was also significantly lower in OxPhos-DLBCLs (Figure 2.12A, middle panel). A potential explanation for these observations is increased diversion of peroxide generated from the SOD-catalyzed reaction into the antioxidant glutathione system. Consistent with this possibility, glutathione (GSH) levels were significantly higher in OxPhos-DLBCLs (Figure 2.12A, right panel), suggesting increased capacity for ROS detoxification.

Given the quantitative differences in ROS and GSH content in DLBCL cell lines, we hypothesized that the capacity to maintain a large GSH pool may be required for the survival of OxPhos-DLBCLs. To test this possibility, *de novo* GSH synthesis was inhibited by shRNA-mediated depletion of γ-glutamyl cysteine synthase (GCS), a rate limiting enzyme that catalyzes the introduction of an amide linkage between the γ-carboxyl group of glutamate and cysteine (Figure 2.12B). OxPhos-DLBCL cell lines were significantly more sensitive to GCS knockdown compared with the BCR subset (Figures 2.12C and 2-S7), suggesting that they may be more reliant on GSH for survival.

DISCUSSION

Our integrative analysis using proteomics, mitochondrial respirometry and metabolomics have unraveled metabolic distinctions in DLBCL subsets. We show that compared with "non-OxPhos"/BCR-DLBCLs, nutrient and energy metabolism in OxPhos-DLBCLs has a significant mitochondrial component, marked by elevated oxidative phosphorylation, increased contribution of mitochondria to total cellular energy budget, greater incorporation of fatty acid- and glucose-derived carbons into the TCA cycle, and increased lipogenesis from these carbon substrates. In comparison, the "non-OxPhos" DLBCLs have greater glycolytic flux. These studies also provide

a clear example of heterogeneity in fuel utilization pathways even within the same disease entity.

The differential utilization of glucose- and fatty acid-derived carbons in OxPhos versus “non-OxPhos” DLBCLs appears to parallel the absence or presence of functional BCR signaling, respectively. This is consistent with our observations that acute inhibition of BCR signaling upon SYK and CD79B depletion is sufficient to enhance palmitate-induced mitochondrial OCR in BCR-DLBCL cell lines. BCR-derived signals are critical for growth and survival of mature B-cells as well as multiple B-cell lymphomas [30]. These signals also trigger glucose utilization in a PI3K-dependent manner that is marked by an initial increase in lactate production and a subsequent shift to the pentose phosphate pathway during progression to S phase [31]. Reduction in glycolytic flux and incorporation of glucose carbons into the pentose pool in OxPhos compared with “non-OxPhos” DLBCLs is consistent with published observations that OxPhos-DLBCLs do not display the full phospho-pattern of signaling intermediates following BCR crosslinking and are insensitive to inhibitors of BCR signaling [18].

The common metabolic profile of “non-OxPhos” DLBCLs is striking given that these tumors rely on multiple components of BCR signaling [18, 32, 33]. This may suggest that proliferation and survival mechanisms in these tumors may converge on glycolysis. The clear distinction between the metabolic profiles of OxPhos- and BCR-DLBCLs suggests that the specific pattern of nutrient metabolism in the former may provide an alternative survival program independent of the BCR network. Moreover, the OxPhos metabolic signature may have broader implications for other tumor types that are independent or have lost dependency on the components of BCR signaling.

Several independent approaches to inhibiting the mitochondrial FAO program significantly compromised the survival of OxPhos-DLBCL. Within this context, BrCA-mediated inhibition of mitochondrial FAO and pharmacologic or genetic interference with PPARγ were selectively toxic to OxPhos-DLBCLs. The relevance of PPARγ in multiple cancer models and the

anti-tumor effects of its inhibition have been reported [34]. Increased PPARγ activity has been recently implicated in differentiation and stimulation of antibody production in normal human B-lymphocytes [35]. Whether this is accompanied by increased FAO in normal lymphocytes remains to be determined. Nevertheless, it is possible that the metabolic signature of OxPhos-DLBCL represents pathways relevant to B-lymphocytes that are further modified to fulfill the nutrient and energy requirements of these tumors.

Findings in other cancer models have suggested that FAO may serve as an alternative survival pathway that is triggered by glucose deprivation or lack of glucose uptake [1, 36]. Moreover, a recent report showed increased FAO in solid tumors contributes to rapamycin resistance [12]. The survival-promoting effect of fatty acid metabolism has also been reported in a leukemia model [37]. In this model, increased fatty acid metabolism was decoupled from oxidative phosphorylation, which appears to be distinct from enhanced ATP-coupled OCR in response to palmitate in OxPhos-DLBCLs.

Concomitant utilization of palmitate-derived acetyl-CoA for ATP production and citrate synthesis in OxPhos-DLBCLs suggests FAO and fatty acid synthesis may be concurrent pathways in these cells. This may be surprising in light of the inhibitory effect of citrate-derived malonyl-CoA on mitochondrial transport of long-chain fatty acids through carnitine palmitoyltransferase (CPT)1. However, several possibilities may explain these observations. The potency of inhibition by malonyl-CoA differs between the two CPT1 isoforms and is likely further influenced by their relative abundance [38]. CPT1A is ~80 fold less sensitive to malonyl-CoA than CPT1B and the ratio of CPT1A to 1B expression is higher in OxPhos-DLBCLs. The relative abundance of CPT1A and the possibility that malonyl-CoA may be used rapidly prior to its accumulation may explain how mitochondrial FAO could proceed unhindered in these cells. A scenario for rapid utilization of malonyl-CoA is active fatty acid synthesis as would be expected in a proliferating cell. In addition, fatty acid synthesis may serve as a “sink” for excess acetyl CoA/citrate generated due to enhanced FAO and increased entry of acetyl-CoA into the

TCA cycle. Concurrent FAO and fatty acid synthesis in other tumors has been observed [39, 40]. It is also interesting to note that increased FAO in AML has been linked to a quiescent pool of tumor-initiating cells [37]. The precise molecular basis for concomitant use of fatty acids for ATP production and citrate synthesis in OxPhos-DLBCLs awaits future studies.

Parallel activation of an antioxidant defense mechanism with increased mitochondrial FAO in OxPhos-DLBCLs is intriguing. A link between FAO and antioxidant capacity has been previously suggested. For example, mitochondrial FAO may serve as a source of NADPH to regenerate GSH [41]. On the other hand, a reduced cellular redox state may be important for completion of β-oxidation [36, 42]. It is also possible that elevated GSH in OxPhos-DLBCL is secondary to its increased synthesis from glutamate. This is consistent with higher enrichment of fatty acid-derived glutamate in this subtype. While increased GSH and MnSOD levels are in agreement with lower ROS content, additional mechanisms contributing to ROS handling in OxPhos-DLBCLs cannot be excluded.

Our findings provide functional validation of quantifiable metabolic differences associated with transcriptionally defined subsets of DLBCL. These observations also indicate that the OxPhos molecular signature is a bona fide metabolic program that is selectively activated in these lymphomas, providing distinct growth and survival benefits. Detailed fingerprints of the DLBCL metabolome may uncover important insights into the molecular pathogenesis and underlying heterogeneity of these lymphomas as well as additional roadmaps to subtype-specific therapeutic targets.

MATERIALS AND METHODS

Primary DLBCL biopsies

Protein samples were prepared from frozen biopsy specimens of newly diagnosed, previously untreated primary DLBCLs with > 80% tumor involvement according to Institutional Review Board-approved protocols from two institutions (Brigham & Women's Hospital and Dana-Farber Cancer Institute). A waiver to obtain informed consent was granted by the IRBs because otherwise discarded tissue was used. The frozen biopsy specimens from which total RNA and high molecular weight DNA were extracted for transcript abundance and SNP analysis have been described in a recent study [43].

Classification of DLBCL primary tumor biopsies based on RNA profiles

Primary DLBCL samples were assigned to consensus clusters using their transcriptional profiles and an ensemble classification scheme previously described [22]. In particular, 13 independent classifiers were trained on the original 141-sample series of DLBCL samples [15] and applied to the 233 R-CHOP treated samples to be classified [21]. Class membership was determined by majority voting, and samples with fewer than 10 of 13 classifiers in agreement were left unassigned. The number and identity of the predictive features (probe sets) used to build each of the 13 classifiers were determined by leave-one-out cross-validation in the training set.

Cell culture, inhibitor, hypoxia and galactose treatments and viability assays

DLBCL cell lines used in this study (Karpas 422, OCI-Ly4, Pfeiffer, Toledo, SU-DHL-4, SU-DHL-6, OCI-Ly1, OCI-Ly7, OCI-Ly3, OCI-Ly10, HBL-1 and U2932) have been previously described [18, 33]. The consensus cluster (CC) assignments of these DLBCL cell lines have been previously defined [18, 22]. The cell-of-origin (COO) designation was determined based on the previously described linear predictive score (LPS) method [17], built upon the 23 (of 27) COO probe sets represented in the microarray. Cell lines were assigned to the GCB class if their

classification probability was greater than 0.9, to the ABC class if their probability was less than 0.1, and to Type 3 otherwise. Intact BCR signaling and dependency on BCR-mediated survival signaling has been confirmed for the HBL-1 and U2932 “ABC-type” DLBCL cell lines [[44] and Margaret Shipp, personal communication].

All cell lines were grown in RPMI supplemented with 10% fetal bovine serum, 2 mM glutamine, and 1% penicillin/streptomycin with the following exceptions. HBL-1 cells were cultured in the above medium containing 1% sodium pyruvate. OCI-Ly3 and OCI-Ly10 cells were cultured in IMDM supplemented with 20% fetal bovine serum or human serum AB (Gemini, West Sacramento, CA), respectively. For inhibitor studies, $2.5x10^6$ cells were treated with 4-bromocrotonic acid (International Lab, San Francisco, CA) at 7.5 μM for 24 hr or with T0070907 (Sigma) or GW9662 (Sigma) at indicated concentrations for 96 hr at 37°C. For assessment of cell viability under hypoxia, cells were grown in 1% O_2 or atmospheric O_2 for 72 hr at 37°C in complete media. For assessment of viability in galactose containing media, cells were grown in serum-free RPMI (US-Biologicals) supplemented with all amino acids except L-glutamine and either 2 g/L D-glucose (Sigma) or 2 g/L D-galactose (Sigma) for 72 hr at 37°C. Cell viability was measured using the Annexin V/FITC Apoptosis Detection Kit (BD Bioscience) followed by flow cytometry.

Mitochondria isolation

Cells were resuspended in mitochondria isolation buffer (MIB; 200 mM mannitol, 70 mM sucrose; 1 mM EGTA; 10 mM HEPES, pH 7.4) containing protease inhibitors, homogenized with 20 strokes of a teflon-glass homogenizer, and resuspended in MIB. The nuclei and cell debris were removed by two consecutive centrifugations at 1000 g for 10 min and the supernatant containing crude mitochondria was centrifuged twice at 9000 g for 20 min. The resultant pellet contained mitochondria-enriched heavy membrane (HM) fraction. For

respirometry and enzyme activity assays, the HM fraction was resuspended in MIB. For 2D-DIGE analysis (Figure 2-S1), the pellet containing the HM fraction was resuspended in MOPS/mannitol buffer (5 mM MOPS, 300 mM mannitol, pH 7.5), carefully overlaid onto a 30/70 % percoll/MOPS/mannitol gradient and centrifuged at 20,000 g for 40 min. Purified mitochondria were collected at the interface between the 30 and 70% percoll gradients, resuspended and washed three times in MOPS/mannitol buffer containing 1 mg/ml defatted BSA.

Sample preparation and labeling for iTRAQ analysis

Mitochondria isolated from DLBCL cell lines or Trizol-purified primary biopsy proteins were solubilized in 7.2 M guanidine hydrochloride, 100 mM ammonium bicarbonate. Protein concentration was determined by the Bradford assay (Bio-Rad, Hercules, CA) and equal amounts of protein were reduced with 10 mM DTT for 30 min at 56ºC, and alkylated with 22.5 mM iodoacetamide for 30 min at room temperature in the dark. DTT was added to a final concentration of 20 mM to quench the remaining iodoacetamide. Proteins were digested overnight with trypsin (1:20) at 37ºC after addition of 100 mM ammonium bicarbonate solution to dilute the concentration of guanidine hydrochloride to 1 M. Digests were acidified with 10% TFA and desalted by C18. Aliquots of peptides were stored at -80ºC.

Mitochondria derived peptides (50 µg) from three OxPhos (Karpas 422, Toledo, and Pfeiffer) and three BCR (OCI-Ly1, SU-DHL-4, and SU-DHL-6) cell lines were solubilized in 100 µL of 30% 500 mM triethylammonium bicarbonate, pH 8.5/70% ethanol and 1 unit of iTRAQ 8-plex reagent was added to each sample (Karpas 422-113, Toledo-114, Pfeiffer-115, OCI-Ly1-117, SU-DHL-4-118, SU-DHL-6-119; note 116 and 121 reagents were not used). The solution was incubated for 1 hr at room temperature, and the reactions were combined and dried by vacuum centrifugation. Labeled peptides were desalted by C18, dried again by vacuum centrifugation, and stored at -80ºC. The same procedure was used to label 100 µg aliquots of primary DLBCL

biopsy-derived peptides with iTRAQ 4-plex reagent [biopsy #32 (OxPhos)-114; biopsy #39 (OxPhos)-115; biopsy #42 (BCR)-116)].

LC-MS/MS analysis of iTRAQ-labeled samples

Approximately 500 ng of iTRAQ labeled peptides were analyzed in duplicate by nano LC-MS/MS [45] using a NanoAcquity UPLC system (Waters, Milford, MA) and quadrupole time-of-flight mass spectrometer (TripleTof 5600, ABSciex, Framingham, MA) equipped with a Digital PicoView ESI source (New Objective, Woburn, MA). Peptides were resolved on a 25 µm analytical column packed with 100 cm 5 µm monitor C18 and introduced to the mass spectrometer at a flow rate of ~10 nL/min using an HPLC gradient (4-55% B in 600 min; spray voltage=2800V) [46]. The mass spectrometer was operated in data dependent mode, with the top 50 precursors (charge state +2 to +5, >50 counts) in each MS scan (800 ms, scan range 350-1500 m/z) subjected to MS/MS (minimum time 100 ms, scan range 100-1800 m/z).

LC-MS/MS data processing for iTRAQ analysis

Data files were converted to .mgf using MSDataConverter version 4.0.404 (ABSciex) with the protein pilot peak generation algorithm, and re-calibrated using parameters derived from fitting experimentally observed masses in high confidence peptide identifications. Files were searched using Mascot version 2.2.1 against a forward-reversed human (38190 forward entries) NCBI refseq database (downloaded Nov. 2009) with an appended cRAP [common repository of adventitious proteins [47]] database of 752 entries. Precursor and product ion tolerances were both 0.5 Da. Search parameters included trypsin specificity, up to 2 missed cleavages, fixed carbamidomethylation (C), variable oxidation (M) and fixed iTRAQ modification (N-term, K). After searching, an excel spreadsheet containing the Mascot search results was generated using Multiplierz version 0.8.3 [48]. Data were first processed to remove reverse database hits and forward hits with FDR >1.0%, and then to remove identifications with mass deviations

greater than 25 ppm. iTRAQ reporter ion intensities were corrected for isotopic impurities as well as minor variations in source protein concentration. Abundance ratios were derived by summing reporters for all peptides mapping to unique genes across replicates, and only genes represented by 2 or more unique peptides are reported.

Mitochondrial respirometry

OCR was measured in real time using the XF24 extracellular flux analyzer instrument and the AKOS algorithm v1.5.069 software (Seahorse Bioscience Inc., North Billerica, MA). For whole cell studies, cells were seeded on XF24 V7 plates coated with Cell-Tak (BD Biosciences) at $3x10^5$ cells/well in 600 μl of sodium bicarbonate-free RPMI medium alone or supplemented with 10 mM glucose, 2 mM glutamine or 0.2 mM palmitate. When palmitate was tested, 0.5 mM carnitine was included in the incubation/equilibration medium to ensure import of BSA-conjugated palmitate into mitochondria. The plates were spun at 500 rpm (breaks off) and incubated at 37°C for 10 min to ensure cell attachment. Measurements were taken for a total of 60 min, including a 12 min incubation period prior to starting baseline measurements. Within this assay time, OCR was measured for 3 min periods with 5 min intervals between measurements. After baseline measurements, 2.5 μM oligomycin was added in a single 75 μl injection. In all experiments, parallel samples were run in the absence of oligomycin to ensure stable baselines as a quality control parameter for the bioenergetic health of the cells.

Determination of oxygen consumption rate (OCR) in isolated mitochondria

OCR was measured in real time using the XF24 extracellular flux analyzer instrument and the AKOS algorithm v1.5.069 software (Seahorse Bioscience Inc., North Billerica, MA). Briefly, the heavy membrane fraction containing mitochondria was prepared as above and loaded on XF24 V7 plates at 15 μg/well in 100 μL of mitochondria assay solution (MAS; 70 mM sucrose,

220 mM mannitol, 10 mM KH_2PO_4, 5 mM $MgCl_2$, 2 mM HEPES pH 7.2, 1 mM EGTA, 0.2% defatted BSA). The plates were spun at 3400 rpm for 10 min at 4ºC. An additional 300 μl MAS was added and the plates were incubated at 37°C for 10 min in the absence of CO_2. Mitochondrial respiration was measured in different respiratory states as previously established [49]. Briefly, OCR measurements were taken in 4 or 6 min periods with 30 s intervals between measurements for a total assay time of 37 min. State II respiration (non-phosphorylating state) was measured upon addition of glutamate/malate or succinate as respiratory substrates at 5 mM each in 100 μl MAS. Glutamate/malate donate electrons to complex I via NADH, and succinate donates electrons to complex II via $FADH_2$. Succinate was combined with 2.5 μM rotenone to inhibit the reverse flow of electrons to complex I. For measurement of state III and IV, 2 mM ADP and 4 μM oligomycin were sequentially delivered using the instrument's individual injection ports. After oligomycin administration, two additional inhibitors were consecutively injected for routine quality control assessment in all experiments. These included 4 μM of the uncoupler FCCP to examine the maximal ETC activity rate when the electron transport was uncoupled from ATP synthesis, and 4 μM of antimycin A (AA) to inhibit the flow of electrons through complex III, preventing the oxidation of both NADH and succinate by mitochondria.

^{13}C Isotopomer-based metabolomics analysis

$10x10^6$ cells were incubated for 8 hr at 37°C in glutamine-free un-buffered RPMI medium containing 10 mM malate, 0.5 mM carnitine, 10 mM β-hydroxybutyrate, 10% (v/v) FBS supplemented with 10 mM glucose, 4 mM glutamine, and 0.2 mM BSA-conjugated palmitate. When tracing glucose or palmitate carbons, the media was supplemented with U-^{13}C-glucose or U-^{13}C-palmitate isotopomers (Cambridge Isotope Laboratories) to the final concentrations

indicated above. Cell pellets and 1 ml aliquots of media were frozen on dry ice and processed for LC-MS/MS and GC/MS.

Cell pellets were lysed in methanol:water (1:1 v/v) via 3 cycles of freeze-thawing. The resulting extraction mixture was vortexed for 30 min and insoluble debris were removed by centrifugation. The supernatants were taken for LC-MS analysis. Intracellular and media ^{13}C-labelled intermediates were quantified using LC-MS/MS with an API4000 triple quadrupole MS system (AB Sciex, Framingham, MA). Analytes of interest were individually tuned and the most sensitive MRM was selected for each analyte. Waters Acquity UPLC HSS T3 2.1x100 mm, 1.8 µm was used for all LC-MS/MS analysis. For TCA cycle intermediates, 5 mM dibutylamine acetate was used as mobile phase A and acetonitrile was mobile phase B. A gradient of 6 min at 0.20 mL/min from 1% to 30% of mobile phase B was employed. Amino acids were prepared for analysis using the AccQ-fluor reagent kit (Waters Corp, Milford, MA). The derivatized amino acids were separated on the Waters Acquity UPLC HSS T3 2.1x100mm, 1.8 µm column with a 13.5 min gradient from 2% to 30% acetonitrile with 0.1% formic acid. The mobile A phase was 0.1% formic acid in water. For the measurement of media U^{13}C-glucose, a three fold excess of acetonitrile was added to the conditioned media. The per-*O*-trimethylsilyl-*O*-methyl derivative of U^{13}C-glucose was generated using methoxamine (MOX) reagent and BSTFA in 1% TMCS (Thermo Fisher Scientific, Pittsburgh PA). Derivatized U^{13}C-glucose was measured by capillary GC/MS using Finnigan trace ultra gas chromatograph interfaced to a Finnigan trace DSQ mass spectrometer (Austin, TX). GC was performed on a Restek Rtx-5Sil MS capillary column (15 m X 0.25 mm i.d., 0.25 µm film thickness; flow-rate 1.0 ml/min He carrier gas; column temperature 70°C for 1 min, programmed to 300°C at 20°C per min, held for 2 min). Mass spectra were obtained in single-ion monitoring (SIM) mode (323.2 *m/z*). At least three separate injections were measured per sample and the percent enrichment of ^{13}C-labeled metabolites in the total metabolite pool was calculated for each metabolite. To facilitate comparison across a panel of eight cell lines and independent experiments, mean values for ^{13}C enrichment were determined

for all OxPhos and BCR cell lines, and these means were normalized to the composite mean percent enrichment of the four BCR cell lines.

Knockdown studies

The following lentiviral vectors containing short hairpins against SYK [50], GCS and CD79B were purchased from The RNAi Consortium (TRC, the Broad Institute); SYK (TRCN0000196401 (#1), TRCN0000003163 (#3), and TRCN0000003164 (#4)), GCS (TRCN0000048484 (#2) and TRCN0000048486 (#4)), CD79B (TRCN0000057650 (#1) and TRCN0000057652 (#3)). In all experiments, shGFP was used as control. Viral supernatants were produced according to the TRC standard protocols and used to spinfect 500,000 cells for 2 hr at 460 g at room temperature. The effect of SYK or CD79B knockdown on palmitate-induced basal OCR was assessed after 24 hr. The effect of GCS knockdown on cell viability were assessed after 72 hr.

For siRNA-mediated depletion of PPARγ, the following siRNAs were used; J-003436-09 (#1), J-003436-08 (#2), and J-003436-07 (#3) (ONTARGETplus, Dharmacon). $5x10^5$ cells were plated in 500 μl medium/well in a 12-well plate. For each transfection, siRNAs (final concentration 50 nM) were mixed with 18 μl Interferin transfection reagent (Polyplus-transfection, Illkirch, France) in 50 μl OPTI-MEM (Life Technologies). The mixture was vortexed for 10 s and incubated at room temperature for 10 min. The mixture was then added dropwise to the cells and the plate was gently swirled. On the following day, 500 μl of cell culture medium was added. Cell viability and knockdown efficiency was assessed 72 hr after transfection.

Palmitate treatment and proliferation assays

Cells were grown in amino acid-free and serum-free RPMI medium supplemented with amino acids except L-glutamine to final concentrations as in RPMI standard culture medium. This

medium was subsequently supplemented with either 0.5 mM carnitine alone or in combination with 0.2 mM palmitate. Cell proliferation was analyzed using the ClickIT EdU Flow Cytometry Assay kit (Invitrogen) following manufacturer's instruction.

Lactate measurements

Extracellular lactate was measured using the Synchron Systems lactate reagent kit per manufacturer's instructions (Beckman Coulter). To derive the portion of lactate produced by glycolysis, cells were seeded exactly as they were in the whole cell respirometry assays and treated with 2.5 μM oligomycin, 20 mM 2-deoxyglucose (2DG), or 10 mM oxamate [51] for 2 hr at 37°C prior to sample collection. Glycolytically derived lactate was defined as the difference between lactate produced in the presence and absence of glycolytic inhibitors.

Enzyme complex activity assays

Complex I, II IV and PDH activity were assessed in isolated mitochondria (100 μg for Complexes I, IV and PDH, 10 μg for Complex II) from each DLBCL cell line in 5-6 independent experiments using microplate assay kits (MitoSciences, Eugene, OR) per manufacturer's instructions.

Analysis of cellular ATP content, mitochondrial ATP synthesis, and energy budget calculations

ATP content was measured using the CellTiter Glo Luminescent Assay per manufacturer's instructions (Promega, Fitchburg, WI). The rate of mitochondrial ATP synthesis was determined as previously described [52]. Briefly, $2.5x10^5$ cells were resuspended in 1 ml of buffer containing 150 mM KCl, 25 mM Tris-HCl, 2 mM EDTA, 0.1% BSA, 10 mM K_3PO_4, 0.1 mM $MgCl_2$, 40 μg/ml digitonin, 0.15 mM P_1,P_5-Di(adenosine) pentaphosphate (an inhibitor of adenylate kinase),

10 mM malate, 10 mM pyruvate, and 1 mM ADP, with or without 1 μM oligomycin. Cells were incubated at 37°C for 15 min. At 0, 5, 10, and 15 min, 50 μl aliquots of the reaction mixture were quenched in 450 μl of boiling buffer containing 100 mM Tris-HCl and 4 mM EDTA (pH 7.75) for 2 min. The aliquots were then diluted 1/10 in the quenching buffer and the quantity of ATP determined using CellTiter Glo. The rate of mitochondrial ATP synthesis was calculated from the difference in ATP content in the presence and absence of oligomycin. Each sample was analyzed in triplicate, with two to three independent experiments for each cell line.

For energy budget calculations, the contribution of mitochondria and glycolysis to total cellular ATP was measured as previously reported [29]. Briefly, oxidative ATP turnover was calculated assuming a P/O ratio of 2.36, where P is nmol of ATP produced per nmol of oxygen consumed (O), which was in turn derived from the oligomycin-sensitive portion of OCR. The contribution of glycolysis to energy budget was calculated assuming a 1:1 stoichiometric ratio between glycolytically derived lactate (as described above) and glycolytically derived ATP. OCR and lactate measurements were done over a 2 hr period. For each cell line, nmol of ATP derived from glycolysis or oxidative phosphorylation were then pooled and percent contributions to the total ATP production were calculated.

Mitochondrial copy number analysis

The mitochondrial copy number was assessed using the mitochondrial SNP probes within the Affymetrix HD-SNP array 6.0 data from an independent series of primary DLBCL samples [[43], GEO accession number GSE34171]. The pre-segmentation data processing was performed according to the SNP array 6.0 analytical pipeline described in [53]. Gene expression profiling of the same samples allowed assignment of consensus cluster subtypes [[43], GEO accession number GSE34171]. Subsequently, the average copy number of 110 mitochondrial SNP probes was computed and visualized using a box plot for the 33 “BCR” and 39 “OxPhos” samples. Differences were tested using a Man-Whitney U-test [54].

Measurement of mitochondrial content in DLBCL cell lines

$1x10^6$ cells per cell line were washed once with warm HBSS (with Ca^{2+} and Mg^{2+}). Cell pellets were resuspended in 1 ml of HBSS solution containing 200 nM MitoTracker Red (Invitrogen) and 40 μM verapamil (Sigma) and incubated at 37°C for 15 min. After labeling, cells were washed once with HBSS and resuspended in 1 ml of fresh HBSS. The mean fluorescence intensity at 581 nm was analyzed by flow cytometry for each cell line.

Assessment of mitochondrial superoxide, total cellular ROS levels and GSH content

Steady state and antimycin A-induced mitochondrial superoxide levels were assessed using MitoSOX Red (Molecular Probes) and the ratio of induced to steady state values determined. Throughout these measurements, the effect of mitochondrial membrane potential ($\Delta\Psi_m$) on mitochondrial accumulation of MitoSOX Red was taken into account. Briefly, for steady state mitochondrial ROS measurements, $1x10^6$ cells were washed with HBSS buffer containing Mg^{2+} and Ca^{2+} and incubated for 15 min at 37°C in 1 ml of HBSS solution containing 5 μM MitoSOX Red and 40 μM verapamil (Sigma) to ensure stable maintenance of MitoSOX Red content within cells. In parallel cell samples, $\Delta\Psi_m$ was analyzed using 50 nM tetramethylrhodamine, ethyl ester (TMRE; Molecular Probes) in the presence of 40 μM verapamil in normal culture media at room temperature for 60 min. MitoSOX Red and TMRE intensities were then assessed using flow cytometry. MitoSOX Red intensity values were normalized to TMRE intensity values. For assessment of ROS levels induced by antimycin A, similar measurements were performed in the presence of 1 μM antimycin A (Sigma). The ratio of induced/steady state was calculated in multiple independent experiments using four independent cell lines per DLBCL subtype ran in triplicate and the mean of pooled values per DLBCL subtype was determined.

Total cellular ROS levels were measured using 5-(and-6)-chloromethyl-2',7'-dichlorodihydrofluorescein diacetate, acetyl ester (CM-H_2DCFDA, Molecular Probes). Briefly, $1x10^6$ cells were washed and incubated in PBS containing 2 μM CM-H_2DCFDA and 40 μM

verapamil for 60 min at 37°C. Cells were then resuspended in normal media and incubated for an additional 15 min before flow cytometry measurement. Parallel positive control samples included cells treated with 50 μM tert-butylhydroperoxide, a potent inducer of ROS.

GSH content was measured using a glutathione assay kit (Northwest Life Science Specialties, LLC) per manufacturer's instruction and used to derive GSH concentration.

Statistical analysis

Unless otherwise indicated statistical analysis was performed using two-tailed student's *t*-test, assuming unequal variance. All values are presented as mean ± SEM. Significance indicated by p-values as follows: *$p < 0.05$, **$p < 0.01$, ***$p < 0.001$. Transcript abundance was visualized with box plots (median, line; 25% and 75% quartile, box; whiskers, minimum to maximum).

Contributions:

Illana Stanley isolated mitochondria for quantitative proteomic analysis and worked in collaboration with Scott Ficarro and Jarod Marto (DFCI) to identify the mitochondrial proteome signature of DLBCL subsets. She also worked collaboratively with Pilar Caro in the Danial laboratory on mitochondrial respirometry studies in intact cells and isolated mitochondria, and performed enzyme activity assays. In collaboration with Amar Kishan and Erik Norberg in the Danial laboratory, Illana assessed lactate production, mitochondrial content, and ROS levels in DLBCL cell lines. Erik Norberg performed knockdown studies. Amar Kishan analyzed cellular ATP budget, measured mitochondrial ATP synthesis rate, designed the metabolomics studies and worked collaboratively with John Gounarides at the Novartis Institute of Biomedical Research to analyze metabolites. Analyses of gene expression profiles and mitochondrial SNP probes in primary DLBCL cases were conducted in collaboration with Margaret Shipp, Bjoern Chapuy (DFCI) and Stefano Monti (Boston University). Illana Stanley, together with Pilar Caro, Amar Kishan and Erik Norberg, contributed to the writing and revision of the manuscript describing these studies, which was published in *Cancer Cell* (22:547-60, 2012) and selected as both a featured article and journal cover.

The content of this chapter first appeared in the following publication:

Caro, P., A. U. Kishan, E. Norberg, I. A. Stanley, B. Chapuy, S. B. Ficarro, K. Polak, D. Tondera, J. Gounarides, H. Yin, F. Zhou, M. R. Green, L. Chen, S. Monti, J. A. Marto, M. A. Shipp and N. N. Danial (2012). "*Metabolic signatures uncover distinct targets in molecular subsets of diffuse large B cell lymphoma.*" Cancer Cell **22**(4): 547-560.

REFERENCES

1. Barger, J.F. and D.R. Plas, *Balancing biosynthesis and bioenergetics: metabolic programs in oncogenesis.* Endocr Relat Cancer, 2010. **17**(4): p. R287-304.

2. DeBerardinis, R.J., et al., *The biology of cancer: metabolic reprogramming fuels cell growth and proliferation.* Cell Metab, 2008. **7**(1): p. 11-20.

3. Tennant, D.A., R.V. Duran, and E. Gottlieb, *Targeting metabolic transformation for cancer therapy.* Nat Rev Cancer, 2010. **10**(4): p. 267-77.

4. Morrish, F., et al., *The oncogene c-Myc coordinates regulation of metabolic networks to enable rapid cell cycle entry.* Cell Cycle, 2008. **7**(8): p. 1054-66.

5. Yuneva, M.O., et al., *The metabolic profile of tumors depends on both the responsible genetic lesion and tissue type.* Cell Metab, 2012. **15**(2): p. 157-70.

6. Koppenol, W.H., P.L. Bounds, and C.V. Dang, *Otto Warburg's contributions to current concepts of cancer metabolism.* Nat Rev Cancer, 2011. **11**(5): p. 325-37.

7. Vander Heiden, M.G., L.C. Cantley, and C.B. Thompson, *Understanding the Warburg effect: the metabolic requirements of cell proliferation.* Science, 2009. **324**(5930): p. 1029-33.

8. Marin-Valencia, I., et al., *Analysis of tumor metabolism reveals mitochondrial glucose oxidation in genetically diverse human glioblastomas in the mouse brain in vivo.* Cell Metab, 2012. **15**(6): p. 827-37.

9. Moreno-Sanchez, R., et al., *The bioenergetics of cancer: is glycolysis the main ATP supplier in all tumor cells?* Biofactors, 2009. **35**(2): p. 209-25.

10. Le, A., et al., *Glucose-independent glutamine metabolism via TCA cycling for proliferation and survival in B cells.* Cell Metab, 2012. **15**(1): p. 110-21.

11. Rossignol, R., et al., *Energy substrate modulates mitochondrial structure and oxidative capacity in cancer cells.* Cancer Res, 2004. **64**(3): p. 985-93.

12. Zaugg, K., et al., *Carnitine palmitoyltransferase 1C promotes cell survival and tumor growth under conditions of metabolic stress.* Genes Dev, 2011. **25**(10): p. 1041-51.

13. Abramson, J.S. and M.A. Shipp, *Advances in the biology and therapy of diffuse large B-cell lymphoma: moving toward a molecularly targeted approach.* Blood, 2005. **106**(4): p. 1164-74.

14. Lenz, G. and L.M. Staudt, *Aggressive lymphomas.* N Engl J Med, 2010. **362**(15): p. 1417-29.

15. Monti, S., et al., *Molecular profiling of diffuse large B-cell lymphoma identifies robust subtypes including one characterized by host inflammatory response.* Blood, 2005. **105**(5): p. 1851-61.

16. Alizadeh, A.A., et al., *Distinct types of diffuse large B-cell lymphoma identified by gene expression profiling.* Nature, 2000. **403**(6769): p. 503-11.

17. Wright, G., et al., *A gene expression-based method to diagnose clinically distinct subgroups of diffuse large B cell lymphoma.* Proc Natl Acad Sci U S A, 2003. **100**(17): p. 9991-6.

18. Chen, L., et al., *SYK-dependent tonic B-cell receptor signaling is a rational treatment target in diffuse large B-cell lymphoma.* Blood, 2008. **111**(4): p. 2230-7.

19. Ross, P.L., et al., *Multiplexed protein quantitation in Saccharomyces cerevisiae using amine-reactive isobaric tagging reagents.* Mol Cell Proteomics, 2004. **3**(12): p. 1154-69.

20. Choe, L., et al., *8-plex quantitation of changes in cerebrospinal fluid protein expression in subjects undergoing intravenous immunoglobulin treatment for Alzheimer's disease.* Proteomics, 2007. **7**(20): p. 3651-60.

21. Lenz, G., et al., *Stromal gene signatures in large-B-cell lymphomas.* N Engl J Med, 2008. **359**(22): p. 2313-23.

22. Polo, J.M., et al., *Transcriptional signature with differential expression of BCL6 target genes accurately identifies BCL6-dependent diffuse large B cell lymphomas.* Proc Natl Acad Sci U S A, 2007. **104**(9): p. 3207-12.

23. el-Aleem, S.A. and H. Schulz, *Evaluation of inhibitors of fatty acid oxidation in rat myocytes.* Biochem Pharmacol, 1987. **36**(24): p. 4307-12.

24. Hsiao, G., et al., *Multi-tissue, selective PPARgamma modulation of insulin sensitivity and metabolic pathways in obese rats.* Am J Physiol Endocrinol Metab, 2011. **300**(1): p. E164-74.

25. Lee, G., et al., *T0070907, a selective ligand for peroxisome proliferator-activated receptor gamma, functions as an antagonist of biochemical and cellular activities.* J Biol Chem, 2002. **277**(22): p. 19649-57.

26. Leesnitzer, L.M., et al., *Functional consequences of cysteine modification in the ligand binding sites of peroxisome proliferator activated receptors by GW9662.* Biochemistry, 2002. **41**(21): p. 6640-50.

27. Fan, T.W., et al., *Altered regulation of metabolic pathways in human lung cancer discerned by (13)C stable isotope-resolved metabolomics (SIRM).* Mol Cancer, 2009. **8**: p. 41.

28. DeBerardinis, R.J., et al., *Beyond aerobic glycolysis: transformed cells can engage in glutamine metabolism that exceeds the requirement for protein and nucleotide synthesis.* Proc Natl Acad Sci U S A, 2007. **104**(49): p. 19345-50.

29. Guppy, M., et al., *Contribution by different fuels and metabolic pathways to the total ATP turnover of proliferating MCF-7 breast cancer cells.* Biochem J, 2002. **364**(Pt 1): p. 309-15.

30. Kuppers, R., *Mechanisms of B-cell lymphoma pathogenesis.* Nat Rev Cancer, 2005. **5**(4): p. 251-62.

31. Doughty, C.A., et al., *Antigen receptor-mediated changes in glucose metabolism in B lymphocytes: role of phosphatidylinositol 3-kinase signaling in the glycolytic control of growth.* Blood, 2006. **107**(11): p. 4458-65.

32. Compagno, M., et al., *Mutations of multiple genes cause deregulation of NF-kappaB in diffuse large B-cell lymphoma.* Nature, 2009. **459**(7247): p. 717-21.

33. Davis, R.E., et al., *Chronic active B-cell-receptor signalling in diffuse large B-cell lymphoma.* Nature, 2010. **463**(7277): p. 88-92.

34. Burton, J.D., D.M. Goldenberg, and R.D. Blumenthal, *Potential of peroxisome proliferator-activated receptor gamma antagonist compounds as therapeutic agents for a wide range of cancer types.* PPAR Res, 2008. **2008**: p. 494161.

35. Garcia-Bates, T.M., et al., *Peroxisome proliferator-activated receptor gamma ligands enhance human B cell antibody production and differentiation.* J Immunol, 2009. **183**(11): p. 6903-12.

36. Schafer, Z.T., et al., *Antioxidant and oncogene rescue of metabolic defects caused by loss of matrix attachment.* Nature, 2009. **461**(7260): p. 109-13.

37. Samudio, I., et al., *Pharmacologic inhibition of fatty acid oxidation sensitizes human leukemia cells to apoptosis induction.* J Clin Invest, 2011. **120**(1): p. 142-56.

38. McGarry, J.D. and N.F. Brown, *The mitochondrial carnitine palmitoyltransferase system. From concept to molecular analysis.* Eur J Biochem, 1997. **244**(1): p. 1-14.

39. Ookhtens, M. and N. Baker, *Fatty acid oxidation to H2O by Ehrlich ascites carcinoma in mice.* Cancer Res, 1979. **39**(3): p. 973-80.

40. Ookhtens, M., et al., *Liver and adipose tissue contributions to newly formed fatty acids in an ascites tumor.* Am J Physiol, 1984. **247**(1 Pt 2): p. R146-53.

41. Pike, L.S., et al., *Inhibition of fatty acid oxidation by etomoxir impairs NADPH production and increases reactive oxygen species resulting in ATP depletion and cell death in human glioblastoma cells.* Biochim Biophys Acta, 2010. **1807**: p. 726-34.

42. Korge, P. and J.N. Weiss, *Redox regulation of endogenous substrate oxidation by cardiac mitochondria.* Am J Physiol Heart Circ Physiol, 2006. **291**(3): p. H1436-45.

43. Monti, S., et al., *Integrative analysis reveals an outcome-associated and targetable pattern of p53 and cell cycle deregulation in diffuse large B cell lymphoma.* Cancer Cell, 2012. **22**(3): p. 359-72.

44. Kloo, B., et al., *Critical role of PI3K signaling for NF-kappaB-dependent survival in a subset of activated B-cell-like diffuse large B-cell lymphoma cells.* Proc Natl Acad Sci U S A, 2011. **108**(1): p. 272-7.

45. Ficarro, S.B., et al., *Improved electrospray ionization efficiency compensates for diminished chromatographic resolution and enables proteomics analysis of tyrosine signaling in embryonic stem cells.* Anal Chem, 2009. **81**(9): p. 3440-7.

46. Zhou, F., et al., *Nanoflow low pressure high peak capacity single dimension LC-MS/MS platform for high-throughput, in-depth analysis of mammalian proteomes.* Anal Chem, 2012. **84**(11): p. 5133-9.

47. Craig, R., et al., *Using annotated peptide mass spectrum libraries for protein identification.* J Proteome Res, 2006. **5**(8): p. 1843-9.

48. Parikh, J.R., et al., *multiplierz: an extensible API based desktop environment for proteomics data analysis.* BMC Bioinformatics, 2009. **10**: p. 364.

49. Chance, B. and G.R. Williams, *Respiratory enzymes in oxidative phosphorylation. I. Kinetics of oxygen utilization.* J Biol Chem, 1955. **217**(1): p. 383-93.

50. Hahn, C.K., et al., *Proteomic and genetic approaches identify Syk as an AML target.* Cancer Cell, 2009. **16**(4): p. 281-94.

51. Rodriguez-Enriquez, S., et al., *Energy metabolism transition in multi-cellular human tumor spheroids.* J Cell Physiol, 2008. **216**(1): p. 189-97.

52. Shepherd, R.K., et al., *Measurement of ATP production in mitochondrial disorders.* J Inherit Metab Dis, 2006. **29**(1): p. 86-91.

53. TCGA, *Comprehensive genomic characterization defines human glioblastoma genes and core pathways.* Nature, 2008. **455**(7216): p. 1061-8.

54. Dawson-Saunders, B. and R. Trapp, *Basic and Clinical Biostatistics*, in *Basic and Clinical Biostatistics*. 1994, Appleton & Lange: Norwalk, CT, 1994.

Chapter 3

Differential Contribution of the Mitochondrial Translation Pathway to the Survival of Diffuse Large B-cell Lymphoma Subsets

SUMMARY

Diffuse Large B-cell Lymphomas (DLBCLs) are a highly heterogeneous group of disorders in which subsets of tumors share molecular features revealed by gene expression profiles and metabolic fingerprints. While B-cell receptor (BCR)-dependent DLBCLs are glycolytic, OxPhos-DLBCLs rely on mitochondrial energy transduction and nutrient utilization pathways that provide pro-survival benefits independent of BCR-signaling. Integral to these metabolic distinctions is elevated mitochondrial electron transport chain (ETC) activity in OxPhos-DLBCLs compared to BCR-DLBCLs, which is linked to greater protein abundance of ETC components. Here, we show that, compared to BCR-DLBCLs, the mitochondrial proteome of OxPhos-DLBCLs is enriched in mitochondrial translation factors, and the mitochondrial translation pathway is required for increased ETC activity and mitochondrial energy reserves in this subtype. Importantly, genetic or pharmacological perturbation of the mitochondrial translation pathway is selectively toxic to OxPhos-DLBCL cell lines and primary tumors. These findings provide additional molecular insights into the metabolic characteristics of OxPhos-DLBCLs, and mark the mitochondrial translation pathway as a target in these tumors that may be of therapeutic utility.

INTRODUCTION

The mitochondrial electron transport chain (ETC) is comprised of a series of large multi-subunit complexes housed within the mitochondrial inner membrane, which carry out multiple redox reactions that ultimately lead to reduction of molecular oxygen to water. The initial electron donors for these reactions are supplied by the TCA cycle in the form of NADH and $FADH_2$. Respiratory chain complexes I (NADH dehydrogenase), III (ubiquinol-cytochrome *c* reductase), and IV (cytochrome *c* oxidase) extrude protons across the inner membrane while transferring electrons. The resulting proton gradient is subsequently coupled to ATP synthesis by the activity of the F_0F_1 ATP synthase (complex V), completing the process of oxidative phosphorylation (OXPHOS). Except for complex II (succinate dehydrogenase), the protein constituents of the ETC complexes are encoded by two independently transcribed and translated genomes; nuclear and mitochondrial [1, 2]. The mitochondrial DNA (mtDNA), which encodes 13 subunits of complexes I, III, IV and V, 22 transfer RNAs, and 2 ribosomal RNAs (Figure 3.1), is a remnant of the mitochondrion's evolutionary origin as a symbiotic prokaryotic partner to early eukaryotes. The mechanism for decoding the mitochondrial genome requires a host of nuclear encoded factors, including ribosomes, translation initiation and elongation factors, and tRNA synthetases that are distinct from the cytoplasmic counterparts dedicated to translation of nuclear transcripts [3, 4]. Mutations in mtDNA and mitochondrial translation factors are associated with ETC failure in several human pathologies [5-11], highlighting the functional relevance of the mitochondrial genome. In addition to coordinate synthesis of respiratory chain subunits encoded by the nuclear and mitochondrial genomes, the functional fidelity of the ETC is influenced by proper assembly and organization of ETC complexes in the inner membrane. ETC complex assembly is modulated by dedicated chaperones and assembly factors, mitochondrial membrane dynamics, as well as membrane lipid composition [12-14].

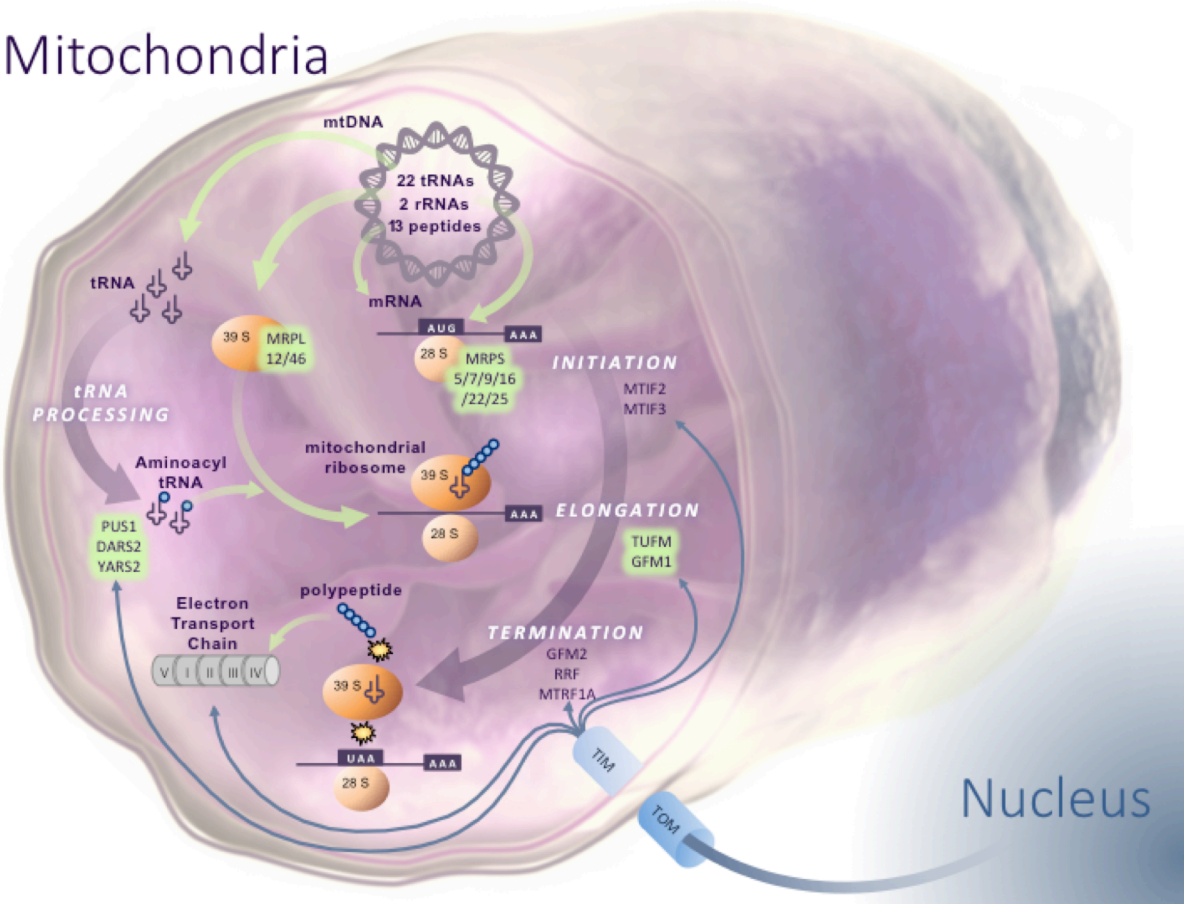

Figure 3.1. Schematic of the mitochondrial translation machinery
Illustration of the three phases of mitochondrial translation; initiation, elongation and termination, as well as the required tRNA processing step to generate aminoacyl-tRNAs for the translation of mtDNA-encoded genes. Key nuclear encoded proteins involved in these processes, which are imported into the mitochondria through the TOM and TIM protein translocation machinery, are also listed. mtDNA in the mitochondrial matrix encodes 22 tRNAs, 2 rRNAs and 13 peptides. Translation of the 13 protein coding genes takes place in the mitochondrial matrix by a dedicated system of mitochondrial ribosomes (large 39S and small 28S subunits) and mitochondrial initiation, elongation and termination factors. During initiation, the mitochondrial mRNA docks with the small 28S mitochondrial ribosomal subunit at the start codon. During elongation, the large 39S subunit docks with the 29S/mRNA complex, and aminoacyl-tRNAs are successively recruited based on base pairing with the mRNA codon. At termination, the small and large subunits dissociate with the assistance of the dedicated termination factors. The released polypeptides, together with nuclear encoded subunits, contribute to the synthesis of complexes I, III, IV and V (ATP synthase). Highlighted in green are proteins that were enriched in the OxPhos-DLBCL proteomic analysis shown in Figure 3.2 and Table 3-S2). Graphics are courtesy of Benjamin Szlyk and Eric Smith.
Abbreviations: mtDNA - mitochondrial DNA, tRNA - transfer RNA, rRNA - ribosomal RNA, mRNA - messenger RNA, TOM - translocase of the outer mitochondrial membrane, TIM - translocase of the inner mitochondrial membrane, I, II, III, IV & V - ETC complexes I, II, III, IV and V.

The balance between OXPHOS and glycolysis, the extent of ETC activity, and the contribution of mitochondria-derived ATP to total energy budget vary widely among tumors [15]. In terms of bioenergetics, some tumors are oxidative, others are glycolytic, and some display both features [15-19]. As described in Chapter 2, the metabolic heterogeneity in the molecular subtypes of Diffuse Large B-cell Lymphoma (DLBCL) includes clear distinctions at the level of mitochondrial function [19]. Specifically, BCR-DLBCLs have greater glycolytic flux typical of the Warburg phenotype [19]. Unlike BCR/Warburg-type DLBCLs, OxPhos-DLBCLs display elevated ETC activity and mitochondrial ATP production, channel the majority of glucose-derived pyruvate into the TCA cycle via increased pyruvate dehydrogenase activity, and exhibit increased mitochondrial oxidation of fatty acids [19]. Importantly, these distinct metabolic and bioenergetic profiles are associated with survival mechanisms and predictable metabolic vulnerabilities. For example, the glycolytic phenotype of BCR-DLBCLs renders them resistant to hypoxia, which blunts OXPHOS, but sensitive to growth in galactose, which shifts metabolism from glycolysis to OXPHOS (Figure 2.11). In comparison, the predominance of mitochondrial metabolism in OxPhos-DLBCLs is consistent with their select sensitivity to hypoxia and resistance to apoptosis in galactose media (Figure 2.11). The differences in ETC activity and OXPHOS dependency among DLBCL subtypes warranted examination of pathways in charge of synthesis and assembly of respiratory chain complexes. Here, we interrogated the mitochondrial translation machinery and its functional contribution to energy metabolism and survival of OxPhos-DLBCLs versus non-OxPhos/BCR-dependent subtypes.

RESULTS

Protein-level signatures capture enrichment of the mitochondrial translation pathway in OxPhos DLBCLs

Our initial quantitative assessment of the mitochondrial proteome from OxPhos- and non-OxPhos/BCR-DLBCLs revealed enrichment of several subunits of the ETC and ETC assembly factors in OxPhos-DLBCLs that is consistent with increased respiratory activity in this subtype (Figure 2.2 and Table 2.1) [19]. However, these analyses, which were performed on an LC-MS/MS platform coupled to a single HPLC column for peptide fractionation (1D LC-MS/MS) [20], captured predominantly protein-level enrichment of nuclear encoded ETC subunits. Because the resulting protein signature was associated with increased activity of several ETC complexes that are encoded by both the nuclear and mitochondrial genomes, we expected that the enrichment of ETC subunits in the OxPhos-DLBCL protein signature should extend to mtDNA-encoded subunits as well. For this reason, we turned to an improved proteomics platform, with higher dynamic range and increased sensitivity (3D LC-MS/MS) [21], in conjunction with iTRAQ labeling, to reassess mitochondria isolated from three independent OxPhos- and three independent BCR-DLBCL cell lines. These analyses not only captured enrichment of mtDNA-encoded ETC subunits in OxPhos-DLBCLs compared to BCR counterparts (Table 3-S1), but also revealed significantly higher levels of numerous nuclear encoded proteins involved in the translation of mitochondrial-encoded transcripts (Figure 3.2A-D, Table 3-S2). Enriched proteins spanned several classes of mitochondrial translation proteins, including mitochondrial elongation factors (TuFM and GFM1), mitochondrial ribosomal proteins (MRP S5, S7, S9, S16, S22, S25, L12, and L46), and mitochondrial tRNA synthetases (DARS2 and YARS2) (Figures 3.1 and 3.2).

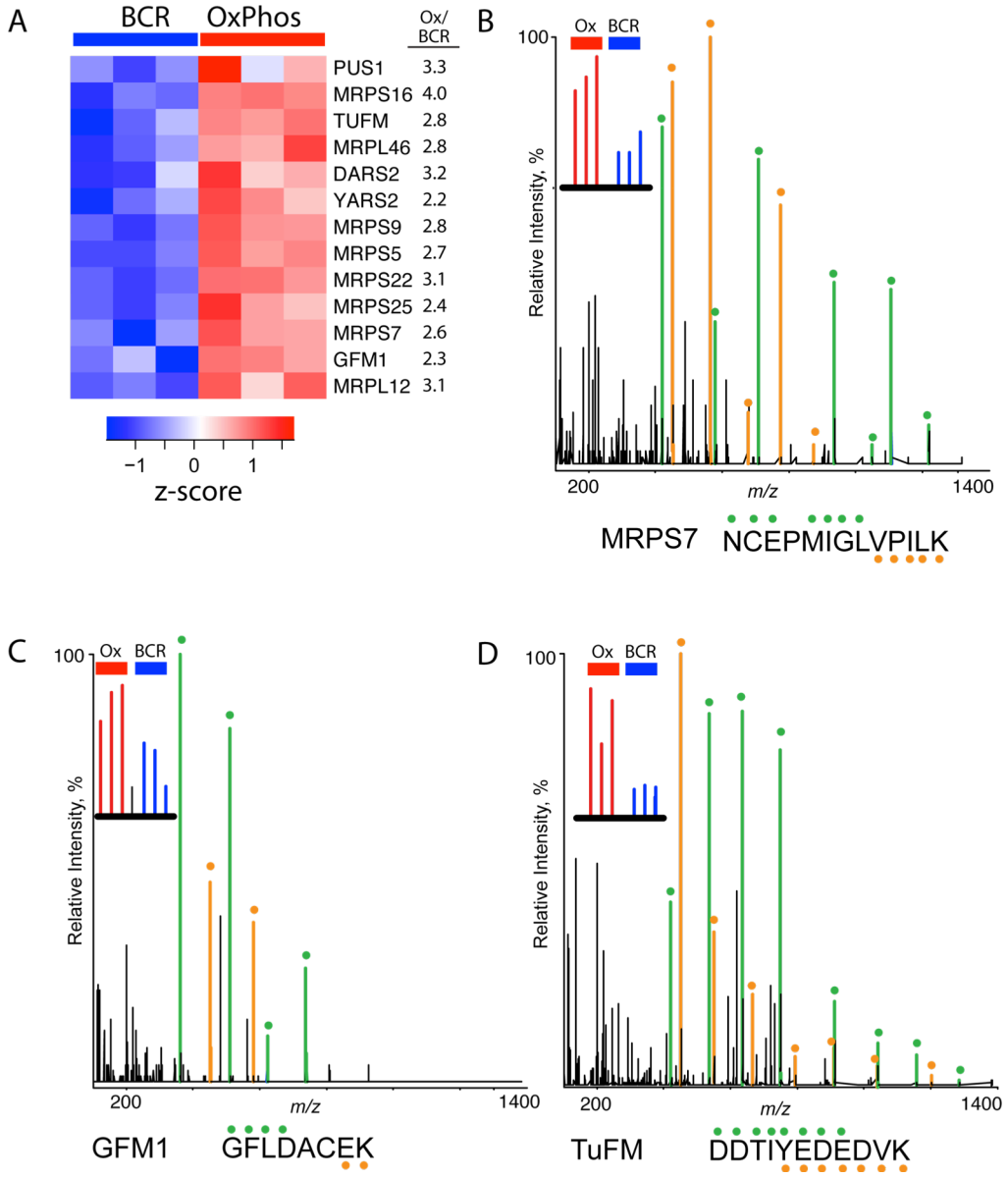

Figure 3.2. Enrichment of mitochondrial translation components in OxPhos-DLBCL mitochondria

Multiplex iTRAQ analysis of isolated mitochondria from three independent OxPhos- (Karpas 422, Pfeiffer, and Toledo) and three non-OxPhos/BCR- (OCI-Ly1, SU-DHL-4, and SU-DHL-6) DLBCL cell lines using the 3D RP-SAX-RP platform (3D LC-MS/MS). (A) Heat map illustrating increased levels of mitochondrial translation proteins in OxPhos-DLBCL cell lines compared to BCR counterparts. OxPhos/BCR ratios on the right indicate abundance ratios derived by summing iTRAQ reporter ion intensities for all peptides mapping to unique genes across replicates per subtype. See also Table 3-S2. (B-D) MS/MS spectra of the indicated unique peptides for MRPS7 (B), GFM1 (C) and TuFM (D) recorded during 3D RP-SAX-RP analysis of mitochondrial proteins shown as an example of differentially enriched peptides. Ions of type b and y are shown in green and orange, respectively. Relative protein ratios in BCR- and OxPhos-DLBCL cell lines are derived from iTRAQ reporter ion intensities shown in inset mass spectrum.

Genetic and pharmacologic inhibition of the mitochondrial translation pathway is selectively toxic to OxPhos-DLBCLs

The robust quantitative enrichment of the mitochondrial translation pathway in OxPhos-DLBCLs warranted examination of its contribution to DLBCL survival. To this end, several independent shRNA hairpins were used to deplete the two elongation factors, GFM1 and TuFM, and the mitochondrial ribosomal protein S7 (MRPS7) in four OxPhos- (Toledo, Pfeiffer, OCI-Ly4 and Karpas 422) and four BCR- (SU-DHL-4, SU-DHL-6, U2932 and HBL-1) DLBCL cell lines, and cell viability was measured. Knockdown of each of these translation factors proved selectively toxic to OxPhos-DLBCL cell lines while sparing the non-OxPhos subset (Figures 3.3A-C and 3-S1A-C). As a common outcome of ETC inhibition is the generation of superoxides, the toxic effects of these knockdowns may be, in part, ROS dependent. This appears to be the case as pre-treatment with the anti-oxidant N-acetyl-cysteine (NAC) prior to knockdown partially, but significantly rescued cell death in this setting (Figure 3.3A-C).

To provide a pharmacologic correlate to these findings, we also tested the effect of tigecycline, a member of the glycylcycline class of antibiotics known to inhibit the prokaryotic ribosome [22, 23], which can also interfere with mitochondrial translation in eukaryotes [24]. Exposure to 1 μM tigecycline for 24 hr was sufficient to lower both cell growth and viability of OxPhos-DLBCLs without affecting BCR-DLBCLs (Figure 3.4A,B). As mitochondrial translation is an essential cellular process and BCR-DLBCLs have functional mitochondria (Figures 2.4A,B and 2.9A), we predicted that tigecycline toxicity in BCR-DLBCLs may manifest at higher doses. Assessment of dose-dependent toxicity of tigecycline over 0.125 to 30 μM concentration range indicated that a significantly higher dose (≥20 μM) of tigecycline was needed to kill BCR-DLBCLs, and that the toxicity dose curve of tigecycline in OxPhos-DLBCLs was shifted to the left (Figure 3.4B). Overall, our genetic and pharmacologic studies demonstrate that OxPhos-DLBCLs are particularly vulnerable to interference of the mitochondrial translation pathway.

Figure 3.3. Differential requirement of the mitochondrial translation pathway for the survival of DLBCL subsets

Effect of shRNA-mediated depletion of the mitochondrial translation elongation factors GFM1 **(**A**)** and TuFM **(**B**),** and mitochondrial ribosomal protein MRPS7 (C) in four OxPhos- (Toledo, Pfeiffer, OCI-Ly4 and Karpas 422) and four BCR- (SU-DHL-4, SU-DHL-6, HBL-1 and U2932) DLBCL cell lines. Blue bars show rescue of cell viability upon pre-treatment of cells with 0.5 mM N-acetyl-cysteine (NAC) prior to shRNA-mediated knockdown. Cell viability was assessed 24 hr after knockdown of the indicated mitochondrial translation factors. Error bars, ± SEM, n=3-4 independent experiments per condition. *$p < 0.05$; **$p < 0.01$; ***$p < 0.001$; two-tailed Student's t-test.

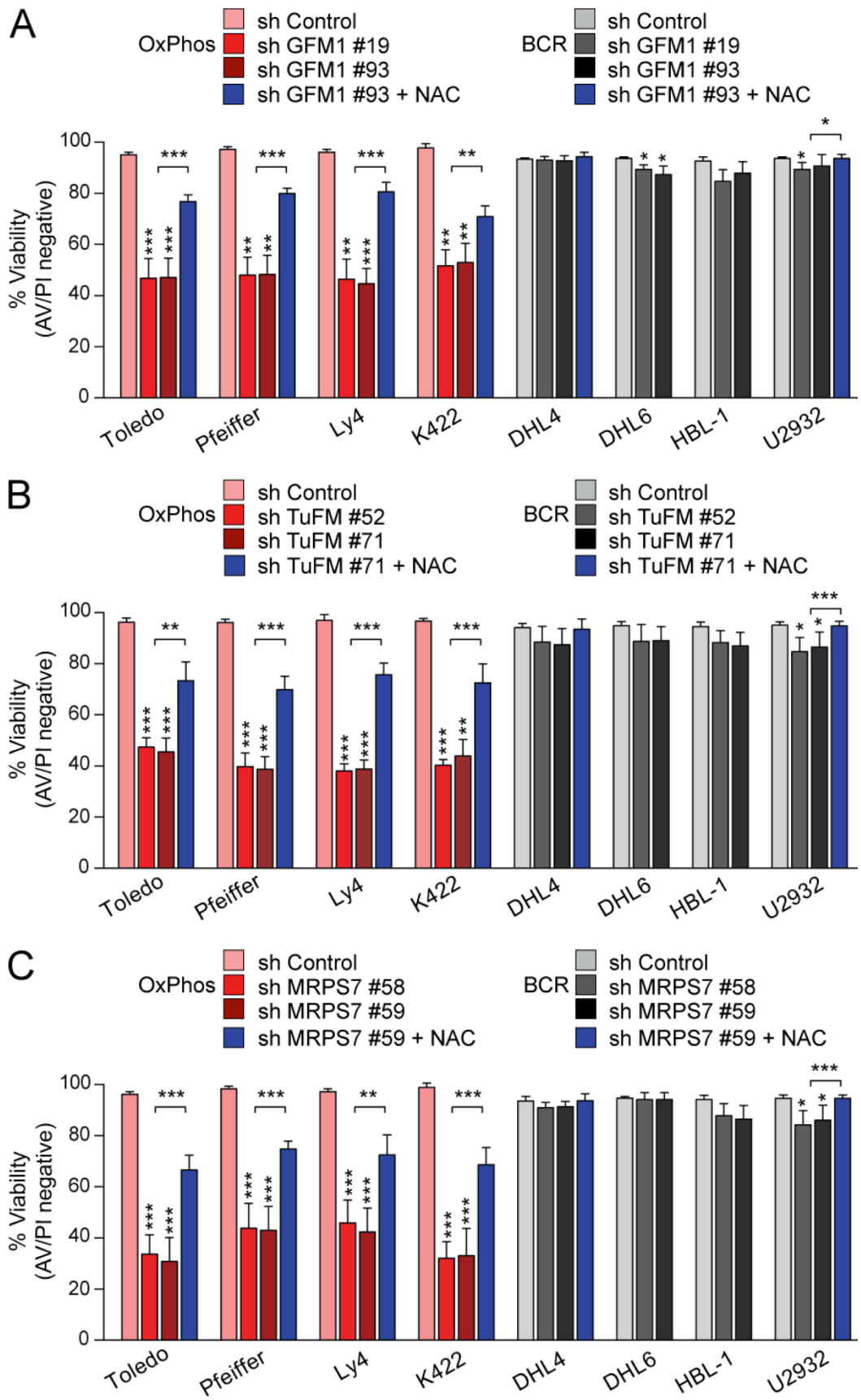

Figure 3.3. (continued)

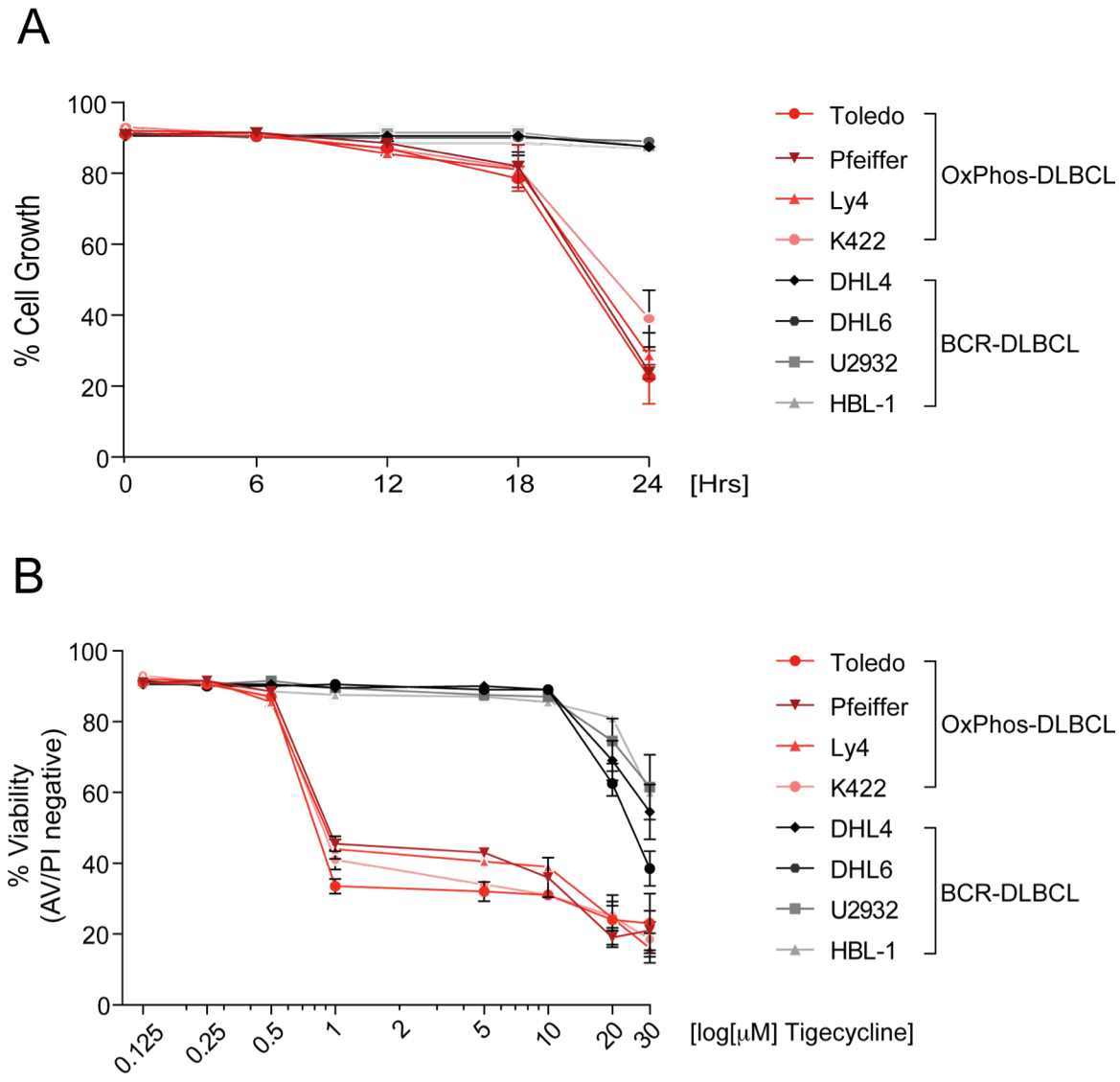

Figure 3.4. Cytostatic and cytotoxic effects of tigecycline in OxPhos-DLBCLs
(A) The effect of 1 μM tigecycline on cell growth over 24 hr period in four OxPhos- (Toledo, Pfeiffer, OCI-Ly4 and Karpas 422) and four BCR- (SU-DHL-4, SU-DHL-6, U2932 and HBL-1) DLBCL cell lines. (B) Survival of DLBCL cell lines, as assessed by Annexin V/PI exclusion, following 24 hr treatment with the indicated doses of tigecycline. n=2-3 independent experiments per tigecycline concentration per cell line.

Tigecycline treatment leads to reduced electron transport activity in ETC complexes containing mitochondrial-encoded subunits

Inhibition of mitochondrial translation is expected to selectively affect the synthesis of peptides encoded by the mitochondrial genome. The vast majority of these peptides are components of the various ETC complexes with the exception of complex II, which is composed solely of nuclear-encoded proteins. To verify that tigecycline treatment selectively affects ETC complexes containing mitochondrial encoded subunits, the biochemical activity of individual ETC complexes was measured in mitochondria isolated from cells treated with 1 μM tigecycline for 20 hr, a time point preceding the appearance of cytostatic and cytotoxic effects of tigecycline in OxPhos-DLBCL cells (Figure 3.4A and data not shown). In particular, mitochondrial respiration on glutamate/malate was used to assay complex I activity, the ETC complex with the largest contribution of subunits from the mitochondrial genome. Meanwhile, succinate was used as the substrate for measuring the activity of complex II (Figure 3.5A). Tigecycline had a larger effect on complex I respiratory rates in OxPhos-DLBCL cells as apparent from diminished rates in response to ADP (state III respiration) and the uncoupler FCCP, which drives maximal respiration (Figures 3.5A,B and 3-S2). In comparison, complex II activity was minimally affected (Figures 3.5A,B and 3-S2). While complex II abundance is not expected to be affected by tigecycline treatment, the slight reduction in respiratory rates in response to succinate can be explained by the fact that complex III and IV, which are subsequent acceptors of electrons from complex II, have mtDNA-encoded subunits that are affected by tigecycline treatment (Figure 3.5A).

In whole cells, selective effects of tigecycline on mitochondrial bioenergetics in OxPhos-DLBCLs were also evident from a significant decline in mitochondrial spare respiratory capacity (SRC) (Figure 3.5C,D). SRC is the difference between mitochondrial basal and maximal respiration (Figure 3.5C) and refers to the mitochondrial reserve capacity to produce energy under cellular stress and increased bioenergetic demand. SRC can significantly affect long-term

cellular function and survival [25, 26]. Compared to BCR-DLBCLs, OxPhos-DLBCLs have significantly larger SRC under steady state conditions (control in Figure 3.5D), which is consistent with higher ETC activity and mitochondrial contribution to total cellular ATP [19]. The significant effect of 1 μM tigecycline on SRC in these cells is consistent with their heightened sensitivity to its toxic effects (Figures 3.4B and 3.5D).

Increased mitochondrial superoxide contributes to tigecycline-mediated death in OxPhos-DLBCLs

Mitochondria are the major intracellular source of reactive oxygen species (ROS), and during normal physiological respiration about 1-2% of the molecular oxygen is converted into superoxide radicals, the precursor for most ROS. Defects in the shuttling of electrons through the ETC complexes lead to electron slippage and ROS production [27]. Consistent with its inhibition of ETC activity, tigecycline treatment was associated with increased mitochondrial superoxide in OxPhos-DLBCLs (Figure 3.6A). NAC treatment blunted the rise in mitochondrial superoxide and significantly rescued tigecycline-induced cell death in OxPhos-DLBCLs (Figure 3.6A,B). These observations are consistent with NAC-mediated rescue of death induced by molecular depletion of mitochondrial translation factors (Figure 3.3A-C), and suggest that tigecycline toxicity in OxPhos-DLBCLs is due, at least in part, to the elevated mitochondrial ROS production that accompanies diminished ETC activity.

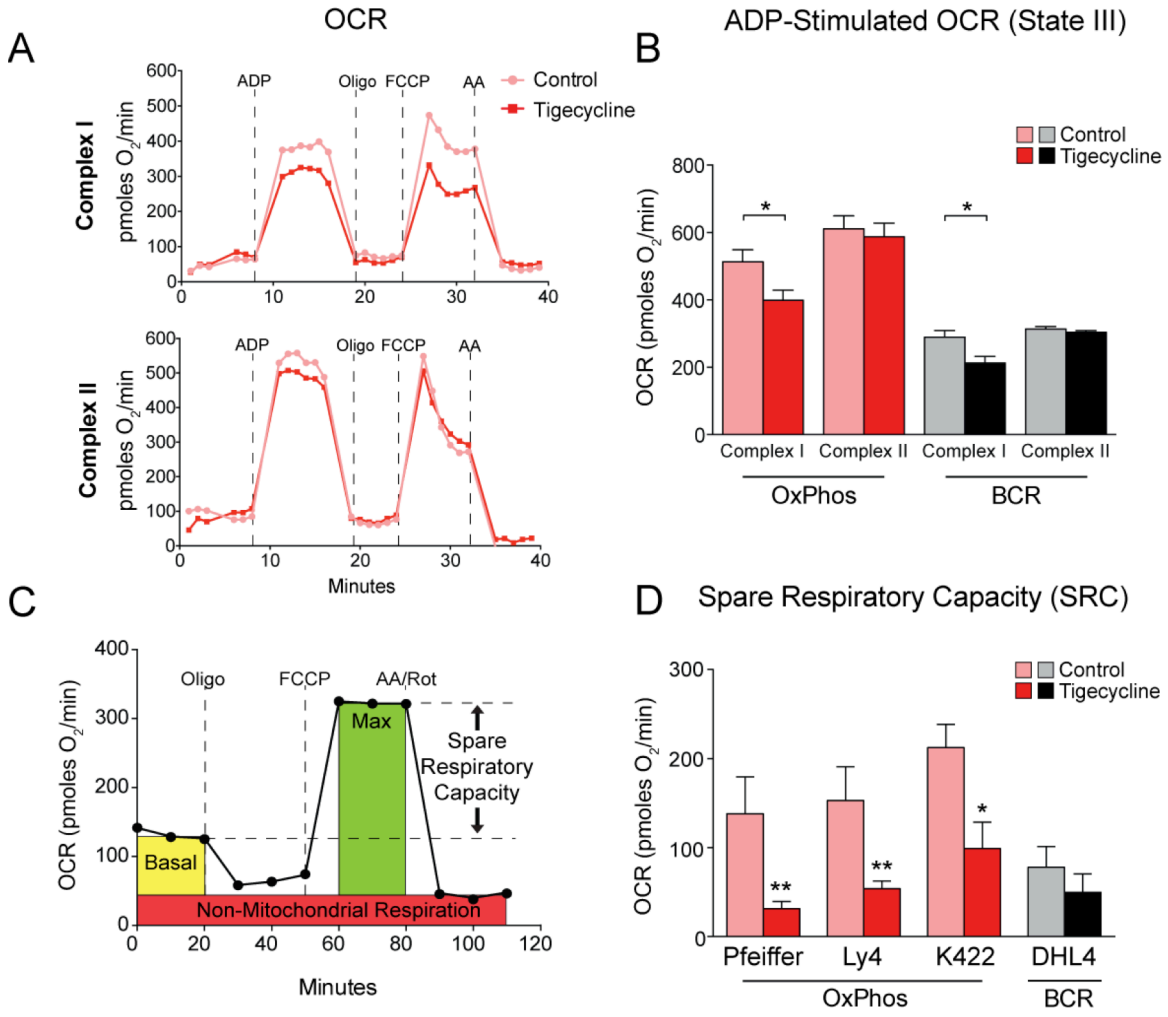

Figure 3.5. Effects of tigecycline on mitochondrial respiration
(A-B) Complex I- and Complex II-linked oxygen consumption rates (OCR) in mitochondria isolated from OxPhos- (Pfeiffer, OCI-Ly4, and Karpas 422) and BCR- (SU-DHL-6) DLBCL treated with tigecycline. (A) Representative OCR traces of mitochondria isolated from one OxPhos-DLBCL cell line (Pfeiffer) supplied with complex I-linked (glutamate/malate) or complex II-linked (succinate) substrates. (B) Cumulative data of ADP-stimulated (State III) respiration derived from n=2-4 independent traces as shown in (A). (C-D) The effect of tigecycline on mitochondrial spare respiratory capacity (SRC). (C) Representative trace of whole cell OCR indicating derivation of SRC. (D) SRC in DLBCL cell lines treated with 1 μM tigecycline for 15 hr, n=3-4 independent OCR measurements per condition in each cell line. Error bars, ± SEM. *p < 0.05; **p < 0.01; two-tailed Student's t-test.

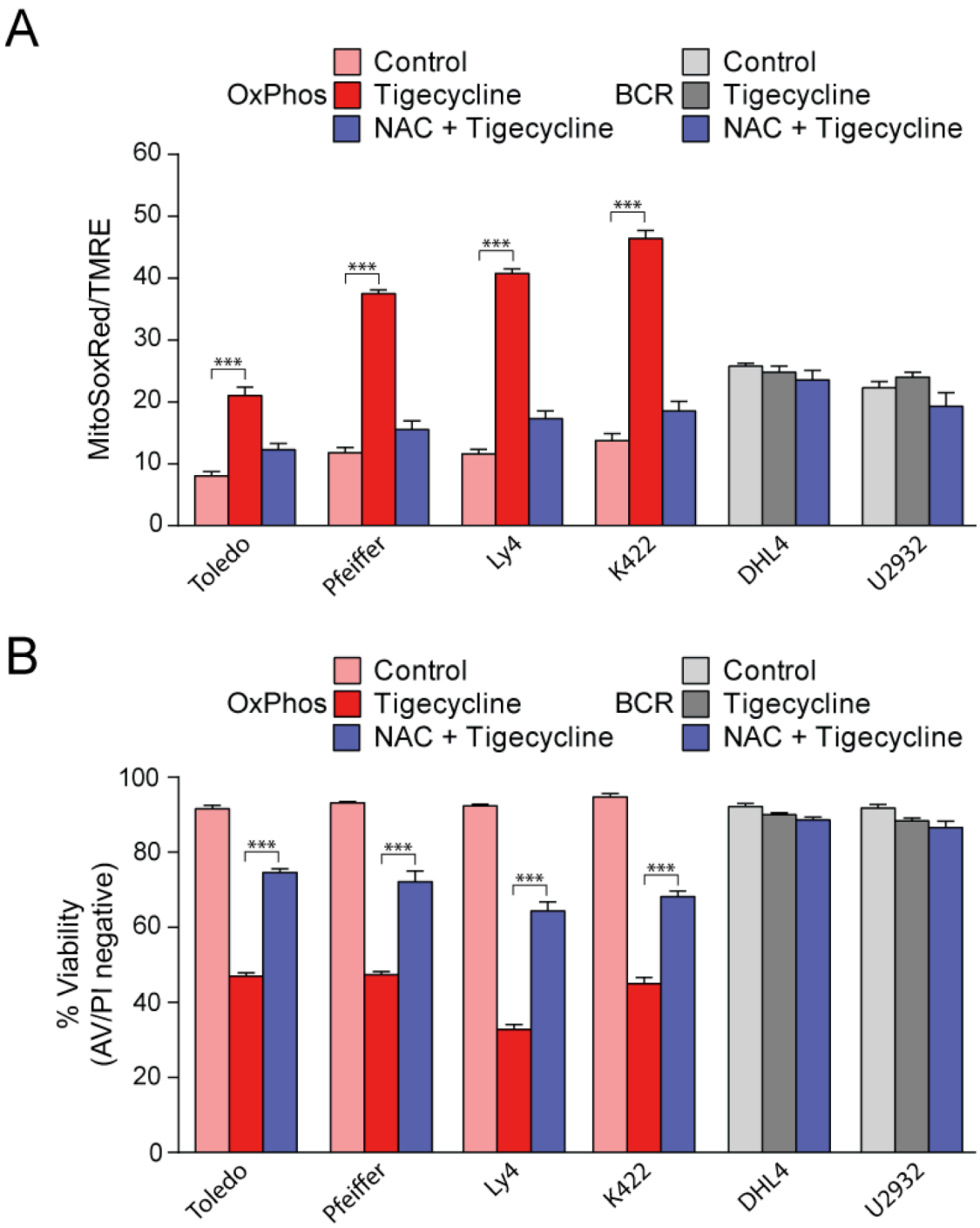

Figure 3.6. Inhibition of the mitochondrial translation pathway stimulates ROS-dependent cell death

(A) Mitochondrial superoxide levels in DLBCL cells that were untreated or treated with 1 mM NAC and subsequently exposed to 1 μM tigecycline for 18 hr. (B) Survival of the indicated DLBCL cell lines analyzed 24 hr following treatment with tigecycline and NAC as in (A). n=2-3 independent experiments per condition. Error bars, ± SEM, ***p < 0.001; two-tailed Student's t-test.

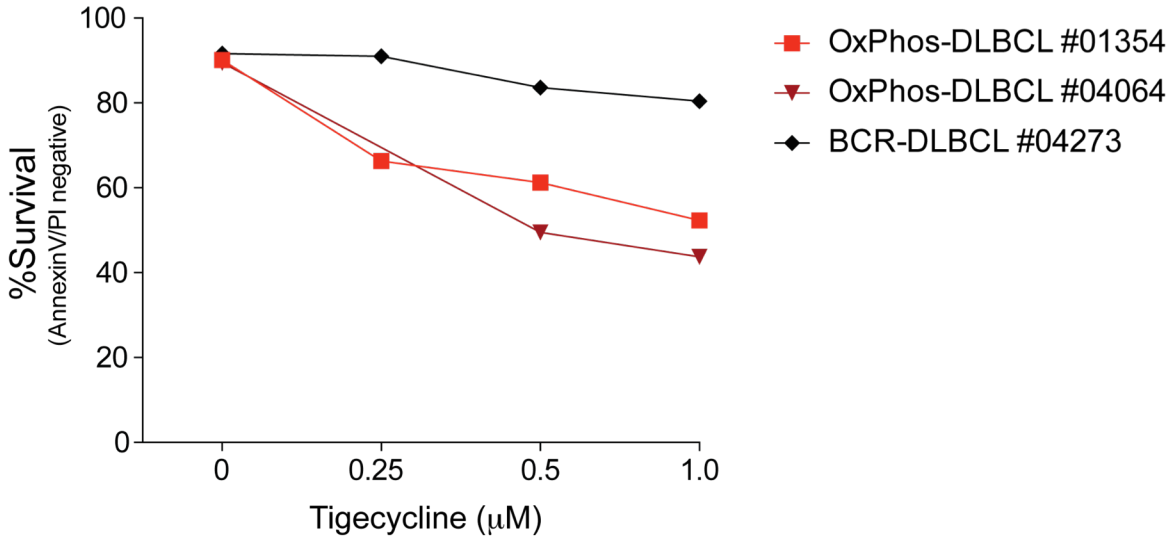

Figure 3.7. Differential sensitivity of primary OxPhos- and BCR-DLBCL tumor cells to tigecycline

DLBCL tumor cells were isolated from two OxPhos- and one non-OxPhos/BCR-DLBCL cryopreserved patient samples and treated with the indicated concentrations of tigecycline. Cell survival was measured by Annexin V/PI exclusion 20 hr post treatment.

Differential toxicity of tigecycline in DLBCL subtypes extends to primary OxPhos- and BCR-DLBCL tumor cells

We next wished to determine whether the differential contribution of the mitochondrial translation pathway to the survival of DLBCL subtypes could be substantiated in primary DLBCLs. To this end, tumor cells were purified from cryopreserved primary biopsies that were previously classified as OxPhos- or BCR-DLBCL using consensus clustering classification (CCC) [28]. Primary DLBCL cells from two OxPhos- and one BCR-DLBCL biopsy were treated for 20 hr with 0.25 to 1 μM tigecycline followed by cell viability measurements. In concordance with our findings in DLBCL cell lines, primary OxPhos-DLBCL cells were significantly more sensitive to tigecycline treatment than non-OxPhos biopsies (Figure 3.7).

DISCUSSION

The current study provides biochemical and functional evidence for the mitochondrial translation pathway as a survival mechanism that supports a central metabolic feature of OxPhos-DLBCLs; increased mitochondrial energy transduction. We show that genetic or pharmacologic perturbations of the mitochondrial translation apparatus lead to subtype-selective toxicity in OxPhos-DLBCL cell lines, which can also be corroborated in primary tumor cells purified from newly diagnosed, previously untreated patient biopsies. At the molecular level, inhibition of the mitochondrial translation pathway is associated with reduced abundance of mtDNA-encoded ETC subunits that would disrupt the stoichiometric balance of mitochondrial- and nuclear-encoded components normally required for functional assembly and integrity of ETC complexes [29]. Interference with the mitochondrial translation apparatus has a greater bioenergetic impact on OxPhos- than BCR-DLBCLs. Compared to BCR-DLBCLs, OxPhos-DLBCLs have a significantly higher steady state mitochondrial spare respiratory capacity (SRC) that is consistent with increased ETC activity and mitochondrial ATP production in this subtype. Inhibition of the mitochondrial translation pathway in OxPhos-DLBCLs lowers the mitochondrial

SRC and increases mitochondrial superoxide production. Increased mitochondrial ROS is likely due to a greater probability of electron slippage when the functional integrity of ETC complexes is diminished [30], and has been previously reported in the context of perturbations in mitochondrial translation factors [31, 32]. In addition, increased mitochondrial superoxide levels in the face of decreased SRC is in line with published studies that have implicated the mitochondrial SRC as an important determinant of cells' capacity to counter oxidative stress [33]. In light of these considerations, it is possible that diminished ETC function and SRC are part of a vicious cycle of oxidative stress that contributes to the toxicity associated with inhibition of mitochondrial translation in OxPhos-DLBCLs. The rescue of viability when cells are treated with an antioxidant prior to tigecycline exposure supports this scenario.

The dependency of OxPhos-DLBCLs on the mitochondrial translation pathway co-segregates with increased abundance of mitochondrial translation factors, higher ETC activity, and greater reliance on oxidative phosphorylation in this subtype compared to BCR/Warburg-type DLBCLs. Within this context, our findings are consistent with an earlier report that identified tigecycline as an antileukemia compound, which exerts its toxic effect through inhibition of mitochondrial translation [24]. Importantly, increased sensitivity of acute myeloid leukemia (AML) cell lines to tigecycline, compared to normal hematopoietic cells, was attributed to higher mitochondrial biogenesis and electron transport in AML cells. Of note, tigecycline treatment of AML cells was not associated with an increase in total cellular ROS, although mitochondrial superoxide was not specifically measured [24]. However, consistent with our observations, studies in other cell types reported increased mitochondrial superoxide content following knockdown of mitochondrial translation factors and examination of MitoSOX Red and DHR123 probe intensities, which specifically measure mitochondrial ROS [31, 32]. The basis of the difference between tigecycline's effect on ROS content in DLBCL and AML cells is unclear. It is possible that, beyond inhibition of mitochondrial translation, tigecycline may invoke cell context-

specific mechanisms that contribute to its toxicity. In the context of OxPhos-DLBCLs, rescue studies using NAC support the idea that oxidative stress is a component of tigecycline toxicity.

Our results extend the mitochondrial proteomic signature of OxPhos-DLBCLs to numerous mitochondrial translation factors consistent with the functional significance of this pathway in OxPhos-DLBCLs. These observations raise the question as to the nature of this programmatic increase in the expression of the mitochondrial translation pathway. It is possible that the programmatic enrichment of mitochondrial translation factors is transcriptionally regulated. Interestingly, several transcription factors that regulate OXPHOS genes also activate the expression of mitochondrial translation factors (cMYC, ERR, and YY1) [34, 35]. In addition, evidence in human breast cancer biopsies indicates a similar increase in expression of mitochondrial ribosomal subunits and other translation factors that appears to be associated with expression of NRF1, NRF2 and PGC1-α, which are transcription factors known to stimulate mitochondrial biogenesis [36]. The molecular basis for the observed enrichment of mitochondrial translation factors in OxPhos-DLBCLs awaits future studies.

Although downstream inhibitors of B-cell receptor signaling, including small molecule inhibitors of SYK and BTK kinases, are being evaluated in DLBCL [37, 38], there are currently no clinically approved targeted therapeutic strategies for OxPhos-type DLBCLs. Our investigation of metabolic distinctions among DLBCL subtypes has led to the identification of several mitochondrial pathways, including fatty acid oxidation [19] and mitochondrial translation that provide selective pro-survival benefits to OxPhos-DLBCLs that, in the fullness of time, may prove clinically relevant. As such, tigecycline is an FDA-approved antibiotic that is being actively developed for its potential therapeutic benefits in AML and other hematologic malignancies as well as infectious diseases [39-41]. Our findings warrant investigation of the therapeutic utility of tigecycline and other inhibitors of the mitochondrial translation pathway in DLBCL.

MATERIALS AND METHODS

Cell culture, growth and viability assays

All DLBCL cell lines were grown as previously described [19]. Cell growth was measured using CellTiter-Glo Luminescent Assay per manufacturer's instruction (Promega). Cell viability was measured using Annexin V/FITC Apoptosis Detection Kit (BD Bioscience) followed by flow cytometry.

RNA interference

Lentiviral vectors containing short hairpins targeting TuFM (TRCN0000160152 and TRCN0000165471), GFM1 (TRCN0000141319 and TRCN0000144593), and MRPS7 (TRCN0000117458 and TRCN0000117459) were purchased from The RNAi Consortium (TRC, the Broad Institute). An empty pLKO.1 vector was used for control. Viral supernatants were produced according to the TRC standard protocols and used to spinfect 500,000 cells for 2 hr at 460 *g* as previously described [19]. The effect of knockdown on cell viability and protein depletion was assessed 24 hr after viral infection.

Immunoblotting

20 μg of whole cell lysates were fractionated on 4-12% gradient NuPAGE gels and subsequently developed by western blotting using anti-GFM1 (Sigma, HPA 034765), anti-TuFM (Abcam, ab85438), anti-MRPS7 (Abcam, ab140149), and anti-β-Tubulin (Millipore, 05-661) antibodies.

N-Acetyl Cysteine treatment

N-acetyl cysteine (Sigma) was used as follows. In knockdown studies (Figure 3.3A-C), 0.5 mM NAC was added directly to the media following spinfection of DLBCL cell lines with lentiviruses bearing shRNA against GFM1, TuFM and MRPS7. For rescue of tigecycline toxicity, 1 mM NAC

was added 30 min prior to treatment with 1 μM Tigecycline. In each case, cell viability was assessed 24 hr after knockdown or tigecycline treatment using Annexin V/FITC as described above.

Determination of mitochondrial superoxide content

Mitochondrial superoxide was measured using MitoSOX Red (Molecular probes) as previously described [19]. All values were normalized to mitochondrial membrane potential as measured by TMRE (Molecular Probes).

Analysis of primary DLBCL samples

Cryopreserved viable primary DLBCL samples were obtained according to Institutional Review Board (IRB)-approved protocols from Mayo Clinic, Brigham and Women's Hospital and the Dana-Farber Cancer Institute. These anonymous primary tumor specimens were considered discarded tissues that did not require informed consent. For assessment of tigecycline sensitivity, cryopreserved viable primary DLBCL samples were Ficoll purified, and tumor cells were treated with the indicated concentrations of tigecycline for 20 hr followed by measurement of cell viability using Annexin V/FITC Apoptosis Detection kit as described above.

iTRAQ analysis of DLBCL mitochondria

Sample preparation for LC/MS. Purified mitochondria were solubilized in 7.2 M guanidine hydrochloride with 100 mM ammonium bicarbonate and protein concentrations determined by Bradford assay (Bio-Rad, Hercules, CA). Equal amounts of protein were reduced with DTT (10 mM final concentration) for 30 min at 56 ºC, and alkylated with iodoacetamide (22.5 mM) for 30 min at room temperature in the dark. After adding additional DTT (final concentration 20 mM) and diluting guanidine hydrochloride concentration to 1 M with 100 mM ammonium bicarbonate, proteins were digested with trypsin overnight at 37 ºC. Digests were acidified with 10% TFA and

desalted by C18. Peptides (50 µg) from three OxPhos (Karpas 422, Toledo, Pfeiffer) and three BCR (OCI-Ly1, SU-DHL-4, SU-DHL-6) cell lines were solubilized in 100 µL of 30% 500 mM triethylammonium bicarbonate, pH 8.5/70% ethanol and 1 unit of iTRAQ 8-plex reagent was added to each sample (K422-113, Tol-114, Pf-115, Ly1-117, D4-118, D6-119). Reactions were incubated for 1 hr at room temperature, combined, dried by vacuum centrifugation, desalted by C18, and dried again.

3D RP-SAX-RP LC-MS/MS. iTRAQ labeled peptides (50 µg) were subjected to multidimensional fractionation with a modified NanoAcquity UPLC system (Waters, Milford, MA) consisting of 2 binary pumps, an autosampler, and an additional 6-port, 2-position valve (Valco, Austin, TX) [21]. First dimension separations were conducted at high pH (10.0) using a reversed phase column (200 µm ID fused silica x 20 cm packed with 5 µM XBridge C18). In the second dimension, peptides were fractionated by strong anion exchange chromatography (200 µm fused silica x 20 cm packed with 5 µM SAX; SEPAX technologies, Neward, DE). Peptides were eluted from first and second dimensions using solutions of acetonitrile and ammonium formate (pH 10), trapped on the final dimension precolumn (200 µm ID fused silica x 4 cm of POROS 10R2) after in-line dilution with 0.1% formic acid, resolved on an analytical column (25 µm ID fused silica packed with 100 cm of 5 µm Monitor C18 (Column Engineering, Ontario, CA), 2–50% B in 580min, A=0.1% formic acid, B=acetonitrile with 0.1% formic acid) and subjected to MS/MS (5600 Triple TOF mass spectrometer, ABI, Framingham, MA). Replicate analyses were performed each with 8 total fractions.

Data Analysis. Raw mass spectrometry data files were converted to .mgf using ABSciex MS Data Converter version 1.3 and searched using Mascot version 2.2.1 after recalibration of precursor and product ions using multiplierz scripts [42, 43]. Search parameters specified precursor and product ion tolerances of 0.5 Da, trypsin specificity, up to 2 missed cleavages, fixed carbamidomethylation (C), variable oxidation (M) and fixed iTRAQ modification (N-term, K). Additional multiplierz scripts were used to filter search results to a 1% false discovery rate,

remove reverse database hits and identifications with mass deviations greater than 25 ppm, and extract iTRAQ reporter ion intensities which were corrected for isotopic impurities as well as minor variations in source protein concentration. Abundance ratios were derived by summing reporters for all peptides mapping to unique genes across replicates, and only genes represented by 2 or more unique peptides are reported.

Measurement of Oxygen Consumption Rates in whole cells and isolated mitochondria

Oxygen consumption rate (OCR) was measured in real time using the XF24 Extracellular Flux analyzer instrument and the AKOS algorithm v1.7.0.74 software (Seahorse Bioscience Inc., North Billerica, MA). For whole cell respirometry studies and measurement of spare respiratory capacity (SRC) (Figure 3.5D), cells were treated with tigecycline for 15 hr prior to seeding on XF24 V7 plates coated with 22.4 µg/ml of Cell-Tak (BD Bioscience) at $3x10^5$ cells/well in 600 µl of sodium bicarbonate-free RPMI medium supplemented with standard concentrations of the amino acids, 10% FBS, 11.1 mM D-glucose and 4 mM L-glutamine. To adhere cells to Cell Tak coated plates, the plates were centrifuged at 400 rpm and incubated at 37°C for 10 min. After baseline measurements, the following order of additions were made using the instrument's individual injection ports; 2.5 µM oligomycin to determine ATP-coupled OCR, 3 µM FCCP to determine maximal OCR, and a combination of 1 µM Antimycin A and 2.5 µM Rotenone to inhibit mitochondrial respiration. SRC was deduced from the difference between maximal and basal OCR.

To measure complex I and complex II activities, mitochondrial OCR was measured in isolated mitochondria supplied with complex I-linked substrate malate/glutamate or complex II-linked substrate succinate as previously described [19]. Briefly, mitochondria were isolated from cells treated with 1 µM tigecycline for 20 hr, and OCR was measured in the presence of 5 mM glutamate/5 mM malate or 5 mM succinate. Succinate was combined with 2.5 µM rotenone to inhibit the reverse flow of electrons to complex I. OCR values shown in Figures 3.5B and 3-S2

indicated state III respiration, which was measured after injection of 2 mM ADP using the instrument's injection ports.

Statistical analysis

All values are presented as mean ± SEM. Statistical significance was determined using two-tailed Student's t-test. Significance indicated by p-values as follows: *$p < 0.05$, **$p < 0.01$, ***$p < 0.001$.

Contributions

The studies described in this chapter were conducted as joint efforts between Illana Stanley and Erik Norberg in the Danial laboratory. Illana Stanley prepared the isolated mitochondria for proteomics studies and performed functional assays to dissect the effects of tigecycline on cellular bioenergetics and mitochondrial respiration. Erik Norberg performed the knockdown studies and worked together with Illana Stanley on analyses of the cytostatic and cytotoxic effects of tigecycline in DLBCL cell lines and primary tumor cells. The proteomics studies were performed in collaboration with Jarrod Marto and Scott Ficarro. Scott Ficarro performed the iTRAQ analysis and worked together with Illana Stanley to identify the mitochondrial proteome signatures of DLBCL subsets. Margaret Shipp (DFCI) and Scott Rodig (Brigham and Women's Hospital) provided the primary DLBCL biopsies, and Linfeng Chen (DFCI) assisted with Ficoll purification of tumor cells. Illana Stanley wrote the manuscript describing these studies, which is currently pending submission.

REFERENCES

1. Falkenberg, M., N.G. Larsson, and C.M. Gustafsson, *DNA replication and transcription in mammalian mitochondria.* Annu Rev Biochem, 2007. **76**: p. 679-99.

2. Rebelo, A.P., L.M. Dillon, and C.T. Moraes, *Mitochondrial DNA transcription regulation and nucleoid organization.* J Inherit Metab Dis, 2011. **34**(4): p. 941-51.

3. Lightowlers, R.N., A. Rozanska, and Z.M. Chrzanowska-Lightowlers, *Mitochondrial protein synthesis: Figuring the fundamentals, complexities and complications, of mammalian mitochondrial translation.* FEBS Lett, 2014. **588**(15): p. 2496-2503.

4. Smits, P., J. Smeitink, and L. van den Heuvel, *Mitochondrial translation and beyond: processes implicated in combined oxidative phosphorylation deficiencies.* J Biomed Biotechnol, 2010. **2010**: p. 737385.

5. Shahni, R., et al., *A distinct mitochondrial myopathy, lactic acidosis and sideroblastic anemia (MLASA) phenotype associates with YARS2 mutations.* Am J Med Genet A, 2013. **161**(9): p. 2334-8.

6. Ohtake, A., et al., *Diagnosis and molecular basis of mitochondrial respiratory chain disorders: exome sequencing for disease gene identification.* Biochim Biophys Acta, 2014. **1840**(4): p. 1355-9.

7. Naviaux, R.K., *Mitochondrial DNA disorders.* Eur J Pediatr, 2000. **159 Suppl 3**: p. S219-26.

8. Marin, S.E., et al., *Leigh syndrome associated with mitochondrial complex I deficiency due to novel mutations In NDUFV1 and NDUFS2.* Gene, 2013. **516**(1): p. 162-7.

9. Koopman, W.J., et al., *OXPHOS mutations and neurodegeneration.* EMBO J, 2013. **32**(1): p. 9-29.

10. Cappelli, E., et al., *Mitochondrial respiratory complex I defects in Fanconi anemia.* Trends Mol Med, 2013. **19**(9): p. 513-4.

11. Calvo, S.E., et al., *Molecular diagnosis of infantile mitochondrial disease with targeted next-generation sequencing.* Sci Transl Med, 2012. **4**(118): p. 118ra10.

12. Tatsuta, T., M. Scharwey, and T. Langer, *Mitochondrial lipid trafficking.* Trends Cell Biol, 2014. **24**(1): p. 44-52.

13. Nunnari, J. and A. Suomalainen, *Mitochondria: in sickness and in health.* Cell, 2012. **148**(6): p. 1145-59.

14. Baker, M.J., T. Tatsuta, and T. Langer, *Quality control of mitochondrial proteostasis.* Cold Spring Harb Perspect Biol, 2011. **3**(7).

15. Jose, C., N. Bellance, and R. Rossignol, *Choosing between glycolysis and oxidative phosphorylation: a tumor's dilemma?* Biochim Biophys Acta, 2011. **1807**(6): p. 552-61.

16. Moreno-Sanchez, R., et al., *The bioenergetics of cancer: is glycolysis the main ATP supplier in all tumor cells?* Biofactors, 2009. **35**(2): p. 209-25.

17. Marin-Valencia, I., et al., *Analysis of tumor metabolism reveals mitochondrial glucose oxidation in genetically diverse human glioblastomas in the mouse brain in vivo.* Cell Metab, 2012. **15**(6): p. 827-37.

18. Guppy, M., *The hypoxic core: a possible answer to the cancer paradox.* Biochem Biophys Res Commun, 2002. **299**(4): p. 676-80.

19. Caro, P., et al., *Metabolic signatures uncover distinct targets in molecular subsets of diffuse large B cell lymphoma.* Cancer Cell, 2012. **22**(4): p. 547-60.

20. Zhou, F., et al., *Nanoflow low pressure high peak capacity single dimension LC-MS/MS platform for high-throughput, in-depth analysis of mammalian proteomes.* Anal Chem, 2012. **84**(11): p. 5133-9.

21. Zhou, F., et al., *Genome-scale proteome quantification by DEEP SEQ mass spectrometry.* Nat Commun, 2013. **4**: p. 2171.

22. Wenzel, R., G. Bate, and P. Kirkpatrick, *Tigecycline.* Nat Rev Drug Discov, 2005. **4**(10): p. 809-10.

23. Jenner, L., et al., *Structural basis for potent inhibitory activity of the antibiotic tigecycline during protein synthesis.* Proc Natl Acad Sci U S A, 2013. **110**(10): p. 3812-6.

24. Skrtic, M., et al., *Inhibition of mitochondrial translation as a therapeutic strategy for human acute myeloid leukemia.* Cancer Cell, 2011. **20**(5): p. 674-88.

25. van der Windt, G.J., et al., *Mitochondrial respiratory capacity is a critical regulator of CD8+ T cell memory development.* Immunity, 2012. **36**(1): p. 68-78.

26. Nicholls, D.G., *Spare respiratory capacity, oxidative stress and excitotoxicity.* Biochem Soc Trans, 2009. **37**(Pt 6): p. 1385-8.

27. Mailloux, R.J., S.L. McBride, and M.E. Harper, *Unearthing the secrets of mitochondrial ROS and glutathione in bioenergetics.* Trends Biochem Sci, 2013. **38**(12): p. 592-602.

28. Chen, L., et al., *SYK inhibition modulates distinct PI3K/AKT- dependent survival pathways and cholesterol biosynthesis in diffuse large B cell lymphomas.* Cancer Cell, 2013. **23**(6): p. 826-38.

29. Papa, S., et al., *The oxidative phosphorylation system in mammalian mitochondria.* Adv Exp Med Biol, 2012. **942**: p. 3-37.

30. Lenaz, G., *The mitochondrial production of reactive oxygen species: mechanisms and implications in human pathology.* IUBMB Life, 2001. **52**(3-5): p. 159-64.

31. Nagar, H., et al., *CRIF1 deficiency induces p66shc-mediated oxidative stress and endothelial activation.* PLoS One, 2014. **9**(6): p. e98670.

32. Echevarria, L., et al., *Glutamyl-tRNAGln amidotransferase is essential for mammalian mitochondrial translation in vivo.* Biochem J, 2014. **460**(1): p. 91-101.

33. Dranka, B.P., B.G. Hill, and V.M. Darley-Usmar, *Mitochondrial reserve capacity in endothelial cells: The impact of nitric oxide and reactive oxygen species.* Free Radic Biol Med, 2010. **48**(7): p. 905-14.

34. Scarpulla, R.C., R.B. Vega, and D.P. Kelly, *Transcriptional integration of mitochondrial biogenesis.* Trends Endocrinol Metab, 2012. **23**(9): p. 459-66.

35. Morrish, F., et al., *The oncogene c-Myc coordinates regulation of metabolic networks to enable rapid cell cycle entry.* Cell Cycle, 2008. **7**(8): p. 1054-66.

36. Sotgia, F., et al., *Mitochondria "fuel" breast cancer metabolism: fifteen markers of mitochondrial biogenesis label epithelial cancer cells, but are excluded from adjacent stromal cells.* Cell Cycle, 2012. **11**(23): p. 4390-401.

37. Younes, A., et al., *Combination of ibrutinib with rituximab, cyclophosphamide, doxorubicin, vincristine, and prednisone (R-CHOP) for treatment-naive patients with CD20-positive B-cell non-Hodgkin lymphoma: a non-randomised, phase 1b study.* Lancet Oncol, 2014. **15**(9): p. 1019-26.

38. Friedberg, J.W., et al., *Inhibition of Syk with fostamatinib disodium has significant clinical activity in non-Hodgkin lymphoma and chronic lymphocytic leukemia.* Blood, 2010. **115**(13): p. 2578-85.

39. Schimmer, A.D. and M. Skrtic, *Therapeutic potential of mitochondrial translation inhibition for treatment of acute myeloid leukemia.* Expert Rev Hematol, 2012. **5**(2): p. 117-9.

40. Jitkova, Y., et al., *A novel formulation of tigecycline has enhanced stability and sustained antibacterial and antileukemic activity.* PLoS One, 2014. **9**(5): p. e95281.

41. Bucaneve, G., et al., *Results of a multicenter, controlled, randomized clinical trial evaluating the combination of piperacillin/tazobactam and tigecycline in high-risk hematologic patients with cancer with febrile neutropenia.* J Clin Oncol, 2014. **32**(14): p. 1463-71.

42. Askenazi, M., J.R. Parikh, and J.A. Marto, *mzAPI: a new strategy for efficiently sharing mass spectrometry data.* Nat Methods, 2009. **6**(4): p. 240-1.

43. Parikh, J.R., et al., *multiplierz: an extensible API based desktop environment for proteomics data analysis.* BMC Bioinformatics, 2009. **10**: p. 364.

Chapter 4

Contribution of Mitochondrial Architecture to Fatty Acid Oxidation in OxPhos-DLBCLs

SUMMARY

Mitochondrial size, shape and network architecture are dynamically regulated by the processes of fusion and fission. Evidence suggests that the balance between fusion and fission can influence the mitochondrial capacity to utilize nutrients, and exposure to different nutrients can in turn lead to adaptive changes in mitochondrial dynamics. We have previously shown that the B-cell receptor (BCR)-independent "OxPhos" subset of Diffuse Large B-cell Lymphoma (DLBCL) displays distinct metabolic features, including a substantial and selective increase in fatty acid oxidation (FAO) capacity compared to other carbon substrates. As FAO provides pro-proliferative and pro-survival benefits to OxPhos-DLBCLs, identification and characterization of molecular modulators of FAO may provide insights into additional targets in these lymphomas. The studies described in this chapter show that FAO is regulated by mitochondrial architecture. Specifically, OxPhos-DLBCLs display a more fragmented mitochondrial network profoundly distinct from BCR-DLBCLs. Remarkably, blocking mitochondrial fragmentation by inhibiting the mitochondrial pro-fission GTPase DRP1 blunts FAO but does not alter oxidation of other fuels, ruling out pleiotropic effects on substrate oxidation. Notably, mitochondrial fragmentation facilitates oxidation of both long- and short-chain fatty acids, indicating that the mitochondrial outer membrane enzyme carnitine palmitoyl transferase (CPT)1, which is specifically required for the import of long-chain fatty acids, is not the main site of FAO regulation by mitochondrial fragmentation. Consistent with its effects on FAO, inhibition of mitochondrial fragmentation is selectively toxic to OxPhos-DLBCLs but does not affect the viability of BCR-dependent DLBCLs. Overall, these findings point to a specific requirement for mitochondrial fragmentation in facilitating FAO and its pro-survival effects in OxPhos-DLBCLs.

INTRODUCTION

Mitochondria are distributed as a network throughout the cytoplasm with specific sizes, shapes and degrees of interconnectedness. These properties are regulated by the competing processes of fusion and fission, controlled by large GTPases at the mitochondrial outer and inner membranes. Mitochondrial fragmentation by fission is primarily executed by Dynamin-related protein 1 (DRP1), a cytosolic protein that is recruited to the mitochondrial outer membrane at points of future membrane constriction [1]. The recruitment of DRP1 to the mitochondrial membrane is likely mediated and/or regulated by one or more integral mitochondrial outer membrane proteins such as FIS1 (Fission protein 1), MFF (Mitochondrial fission factor) and MiD49/MiD51 [2] (Figure 4.1). Fusion is orchestrated by mitofusins (MFN) 1 and 2 in the outer mitochondrial membrane and the optic atrophy 1 (OPA1) protein in the inner mitochondrial membrane [3] (Figure 4.1).

While early reports implicated the fragmented vs. connected state of the mitochondrial network in the regulation of cell-death/apoptotic mechanisms [4-7], recent work suggests a broader role for mitochondrial dynamics as a general homeostatic mechanism for changes in nutrient utilization and energy demand [8]. This is in turn linked to the capacity of fusion and fission factors to integrate signals from external and internal stimuli to adapt mitochondrial morphology to the changing needs of the cell. For example, during complete starvation conditions, the inhibitory phosphorylation of DRP1 by cAMP dependent protein kinase A (PKA) at Ser637 generates hyperfused mitochondria that are spared from autophagic degradation [9]. Conversely, excess nutrient overload leads to mitochondrial fragmentation in pancreatic β-cells as a protection against apoptosis induced by glucolipotoxicity [10]. It is likely that modulation of nutrient utilization capacity by mitochondrial architecture occurs through multiple control points, including the organization and assembly of electron transport chain components [11], as well as mitochondrial nutrient access and import. The precise regulation of these processes by mitochondrial network architecture is not fully understood.

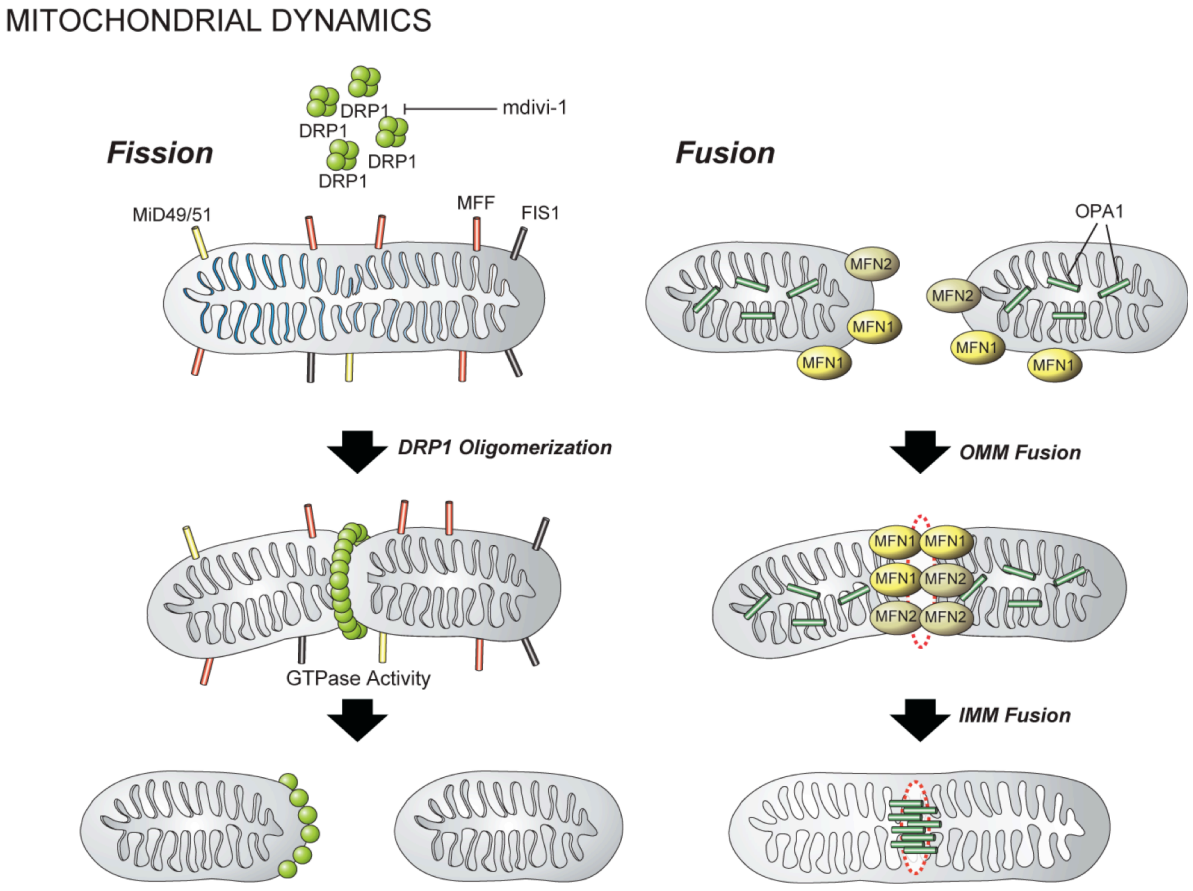

Figure 4.1. Protein mediators of fusion and fission
Illustration of the competing processes of fission (left) and fusion (right). Fission is mediated by the recruitment of cytosolic DRP1 to the outer mitochondrial membrane. MFF, FIS1 and MiD49/51 are proteins tethered to the outer mitochondrial membrane, which play a role in recruiting DRP1 to the outer membrane. DRP1 GTPase activity leads to constriction of one mitochondrion into two. This activity is inhibited by the small molecule mdivi-1. Fusion of the outer membrane is mediated by MFN1 and 2 GTPases, which form oligomers that connect two mitochondria before fusion and mediate merging of the outer membranes. Inner membrane fusion is regulated by the IMM protein OPA1.
Abbreviations: Dynamin related protein 1 (DRP1), Mitochondrial fission factor (MFF), Mitofusin (MFN) 1 and 2, Outer mitochondrial membrane (OMM), Inner mitochondrial membrane (IMM).

As described in Chapter 2, we recently characterized distinct patterns of fuel utilization capacity and associated metabolic dependencies in two genetic subsets of Diffuse Large B-Cell Lymphoma (DLBCL). In particular, OxPhos-DLBCLs display elevated mitochondrial electron transport chain (ETC) activity and ATP production, as well as greater incorporation of fatty acid-derived carbons into the tricarboxylic acid (TCA) cycle [12]. These tumors survive independent of B-cell receptor (BCR) signalling, which is important for the activation and maintenance of normal B-lymphocytes and for the survival of the BCR-dependent DLBCL subtype [13-16]. Instead, OxPhos-DLBCLs rely on mitochondrial fatty acid oxidation (FAO) for proliferation and survival [12]. Early dissection of pathways that could contribute to enhanced FAO in OxPhos-DLBCLs identified a role for PPARγ, a transcriptional regulator of fatty acid oxidation enzymes that contributes to the survival of OxPhos-DLBCLs [12]. However, it is likely that additional pathways promote FAO in OxPhos-DLBCLs. Identification of these pathways may not only provide molecular insights into regulation of FAO, but also uncover additional strategies to interfere with FAO-dependent survival. The studies reported in this chapter have identified a functional link between mitochondrial architecture, in particular a more fragmented mitochondrial network, and FAO in OxPhos-DLBCLs.

RESULTS

OxPhos-DLBCLs maintain a more fragmented mitochondrial network

To examine whether the distinct fuel utilization patterns in DLBCL subtypes are associated with changes in mitochondrial morphology, the mitochondrial network was examined in a panel of four OxPhos- and four BCR-DLBCL cell lines that were fixed and stained with the mitochondrial potentiometric dye Mitotracker Red. Mitochondria appeared smaller in OxPhos-DLBCL cell lines compared to large globular mitochondria observed in BCR-DLBCL cell lines (Figure 4.2A).

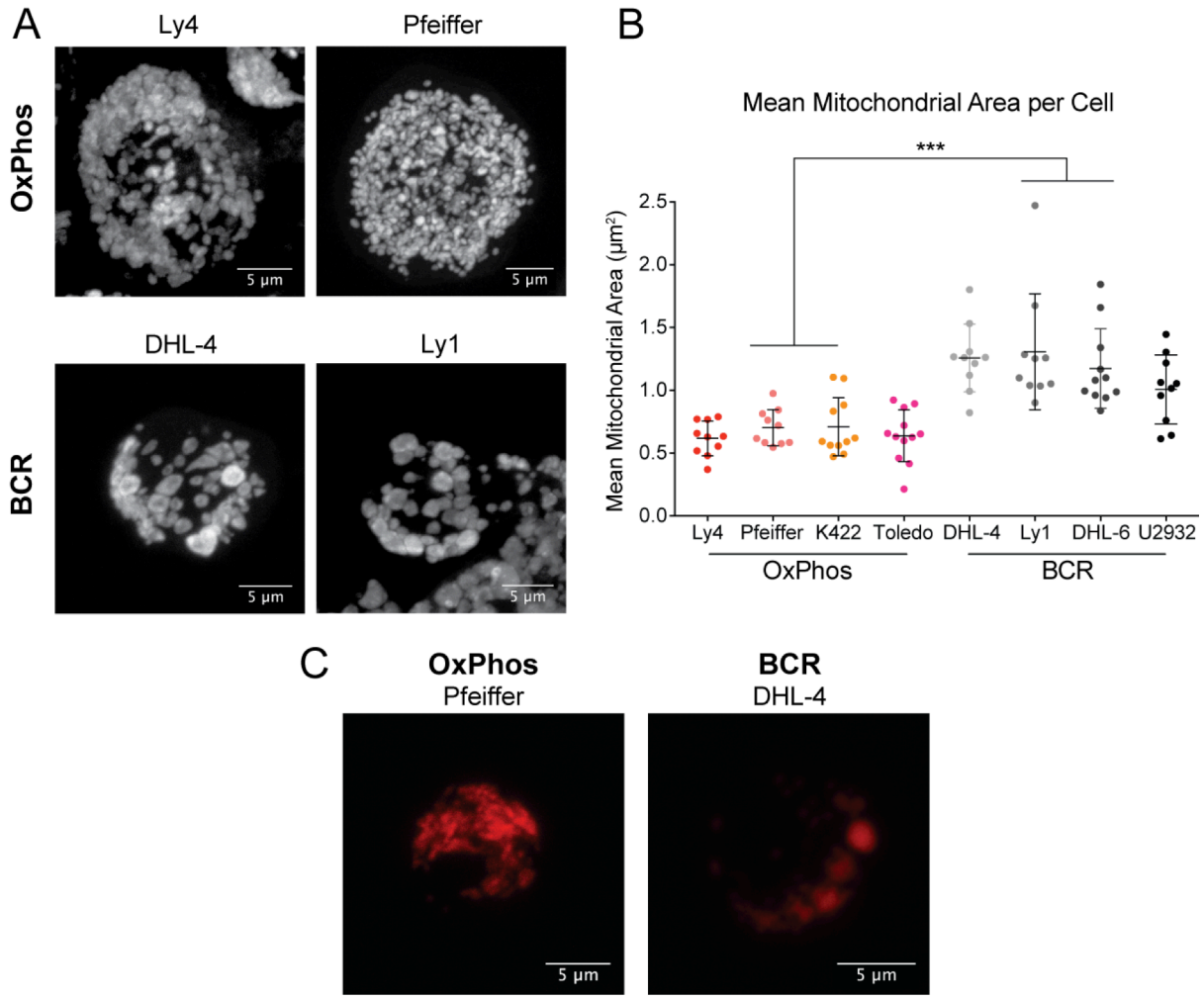

Figure 4.2. OxPhos- and BCR-DLBCL cell lines have distinct mitochondrial morphologies

(A) Representative images of the mitochondrial network in OxPhos- and BCR-DLBCL cell lines labeled with Mitotracker Red. Each image displays maximum intensity projections of 0.25 µm interval Z-stacks displaying the mitochondrial network within a single representative cell. (B) Quantification of mean mitochondrial area per cell for four OxPhos- and four BCR-DLBCL cell lines. Error bars, ± SEM. ***p < 0.001; two-tailed Student's t-test. (C) Representative confocal images of live cells expressing the matrix targeted dsRed, which were immobilized in low percentage agarose before imaging.

Careful quantification of mean mitochondrial cross-sectional area per cell indicated that the average mitochondrial area was significantly reduced in OxPhos-DLBCL cell lines compared to BCR counterparts (Figure 4.2B). Moreover, similar observations were made in live cells upon labeling mitochondria with matrix-targeted dsRed (mt-dsRed) or the membrane potential sensitive dye TMRE, indicating that the observed morphologic differences were not an artifact of fixation (Figure 4.2C and data not shown). These data suggest that the mitochondrial network in OxPhos-DLBCLs may be more fragmented, which can in turn stem from changes in the net balance of mitochondrial fusion and fission, including increased relative rates of fission over fusion.

Genetic and pharmacologic inhibition of mitochondrial fission blocks mitochondrial fragmentation and perturbs FAO in OxPhos-DLBCLs

Given that the fragmented mitochondrial network was restricted to OxPhos-DLBCLs and was not observed in BCR-DLBCLs, a possible connection between mitochondrial morphology and FAO, which is a prominent metabolic feature of OxPhos-DLBCLs [12], warranted investigation. This was initially addressed by examining palmitate oxidation in OxPhos- and BCR-DLBCL cell lines in which the pro-fission protein DRP1 was inhibited using the K38A dominant-negative DRP1 mutant (DRP1-DN) [17]. As expected, expression of DRP1-DN, in both OxPhos- and BCR-DLBCL cell lines, led to a more fused mitochondrial network (Figure 4.3A). This was associated with reduced FAO in OxPhos-DLBCLs as measured by mitochondrial respiration rates in response to palmitate (Figure 4.3B,C). Expression of DRP1-DN in BCR-DLBCL cell lines did not alter FAO (Figure 4.3B,C). To provide a pharmacologic correlate to the effect of DRP1-DN on FAO, a small molecule inhibitor of DRP1 GTPase activity, mdivi-1 [18], was also examined. Similar to DRP1-DN, 24 hr treatment with mdivi-1 led to a decrease in FAO (Figures 4.4A and 4-S1).

Figure 4.3. Inhibition of DRP1 selectively reduces FAO capacity in OxPhos-DLBCLs
(A) Representative confocal images of OxPhos- and BCR-DLBCL cell lines expressing DRP1-DN in which mitochondria were labeled with Mitotracker Red. Maximum intensity projections of 0.25 μm interval z-stacks are shown. (B-C) Mitochondrial oxygen consumption rates (OCR) on palmitate in DLBCL cell lines expressing DRP1-DN. (B) Representative OCR traces are shown for one OxPhos-DLBCL (Pfeiffer) and one BCR-DLBCL (SU-DHL-4) cell line. Dotted line indicates time-point of oligomycin injection. Representative western blots showing the level of DRP1-DN in the same cell lines are shown on top. (C) Cumulative data for ATP-coupled OCR in two OxPhos-DLBCL (Pfeiffer and OCI-Ly4) and one BCR-DLBCL (SU-DHL-4) cell line deduced from similar traces as in (B), n=2 independent experiments per cell line. All analyses were performed 24 hr after infection with lentiviruses carrying DRP1-DN or empty vector control. Error bars, ± SEM. ***$p < 0.001$; two-tailed Student's t-test.

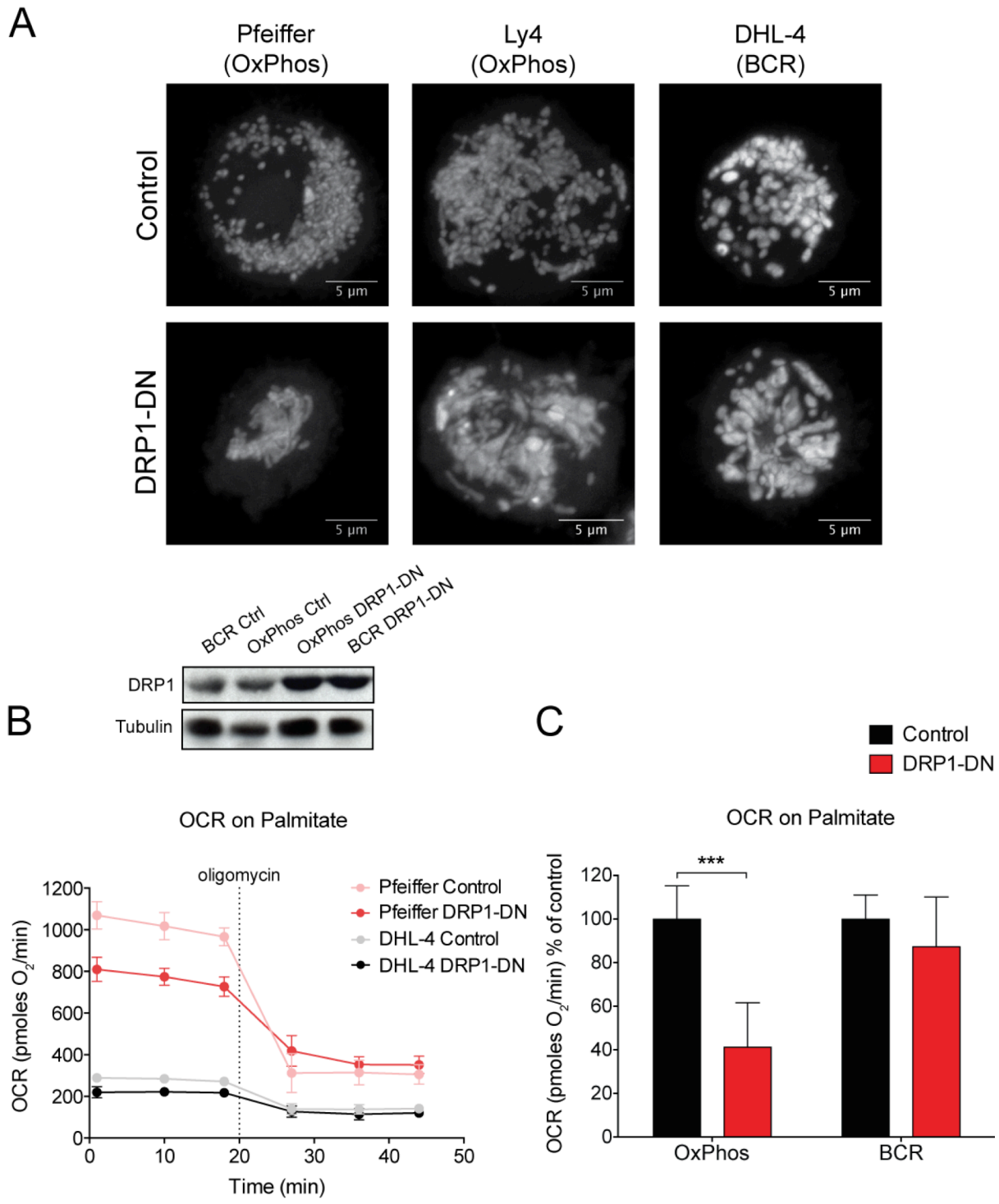

Figure 4.3. (continued)

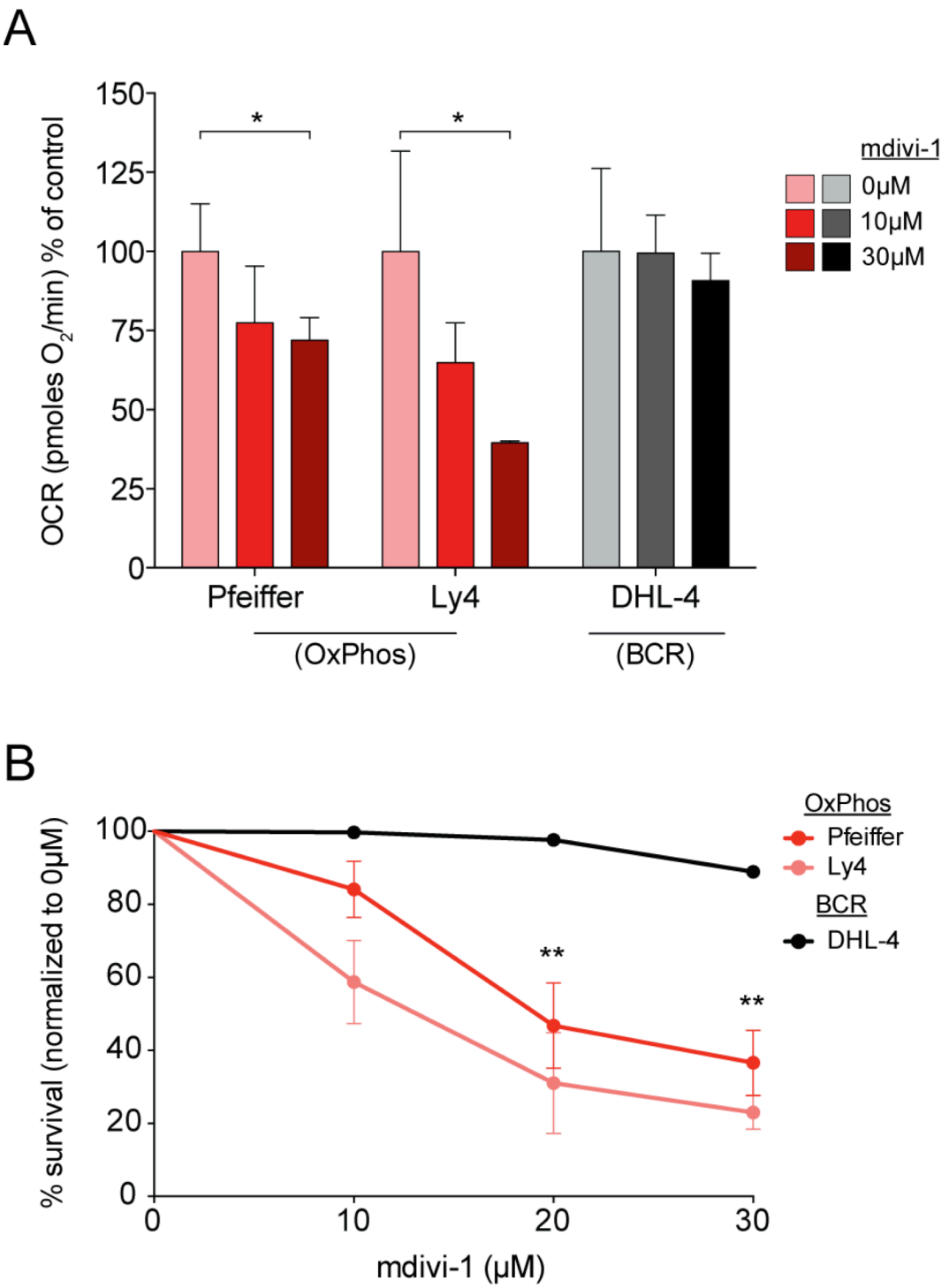

Figure 4.4. A chemical inhibitor of DRP1 reduces FAO and viability in OxPhos-DLBCLs
(A) ATP-coupled oxygen consumption rates (OCR) in response to palmitate in the indicated DLBCL cell lines following 24 hr treatment with mdivi-1 with the indicated concentrations, n=3 independent experiments per condition (B) Survival of DLBCL cell lines treated for 48 hr with 10-30 μM mdivi-1. Asterisks in (B) compare the BCR-DLBCL cell line to both OxPhos-DLBCL cell lines, n=3 independent experiments per condition Error bars, ± SEM. *$p < 0.05$; **$p < 0.01$; two-tailed Student's t-test.

Because FAO contributes to the survival of OxPhos-DLBCLs [12], blocking mitochondrial fragmentation and the attendant reduction in FAO is predicted to be toxic to this subtype over longer periods of time. Low infection efficiency of DLBCL cell lines precluded examination of long-term effects of DRP1-DN. For this reason, we investigated the outcome of mdivi-1 treatment on DLBCL survival. A selective and dose-dependent diminution of cell viability was apparent in OxPhos-DLBCL cell lines following 48 hr treatment with mdivi-1 (Figure 4.4B). These results suggest that maintaining a fragmented mitochondrial network may be relevant to OxPhos-DLBCL survival by supporting/promoting FAO.

Regulation of fuel oxidation by mitochondrial fragmentation is selective for fatty acids and independent of fatty acid chain length

To determine if inhibition of fission has a pleiotropic effect on mitochondrial fuel oxidation, we compared mitochondrial oxidation of glutamine in the presence or absence of DRP1-DN. We have previously shown that both DLBCL subtypes are capable of respiring on glutamine (Chapter 2, Figure 2.4). In contrast to its effect on FAO, DRP1-DN did not alter mitochondrial handling of glutamine (Figures 4.5 and 4-S2). Thus, in this setting, the contribution of mitochondrial fragmentation to fuel oxidation appears to be selective for fatty acids. However, additional studies are required to expand the spectrum of respiratory substrates examined in these experiments.

Because blocking mitochondrial fragmentation inhibits FAO but does not alter oxidation of glutamine, the effect of mitochondrial morphology on FAO is less likely to occur through regulation of the TCA cycle or respiratory chain activity per se. For this reason, we turned our attention to fatty acid import from the cytoplasm to the mitochondrial matrix where the enzymes of fatty acid β-oxidation are localized.

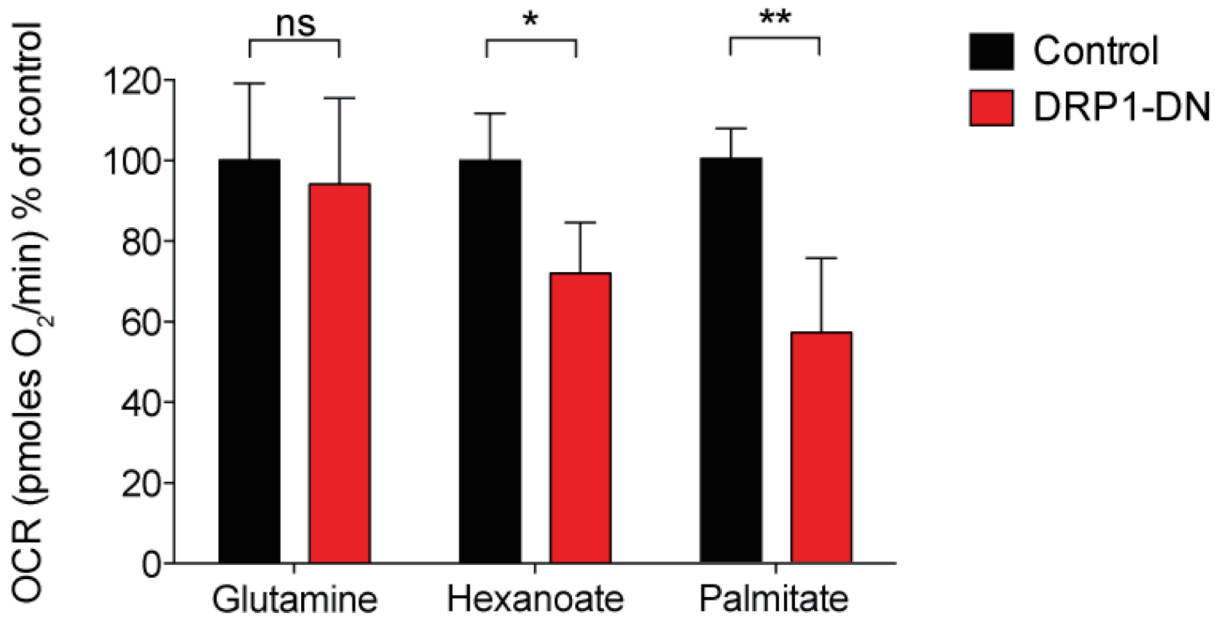

Figure 4.5. Blocking fragmentation reduces oxidation of fatty acids but not other carbon substrates

ATP-coupled mitochondrial oxygen consumption rates (OCR) in response to 0.2 mM palmitate, 0.5 mM hexanoate or 2 mM L-glutamine 24 hrs after lentiviral transduction of DRP1-DN . Cumulative data from three independent experiments in two OxPhos-DLBCL cell lines (Pfeiffer and OCI-Ly4) are shown. Error bars, ± SEM. *$p < 0.05$; **$p < 0.01$; two-tailed Student's t-test.

Long chain fatty acids such as palmitate require conjugation to carnitine via carnitine palmitoyl transferase (CPT)1 for transport across the mitochondrial inner membrane while short chain fatty acids are able to passively diffuse across the inner membrane [19]. We reasoned that if CPT1 is a step where mitochondrial fragmentation exerts its effect, then DRP1-DN expression should selectively affect oxidation of palmitate but not hexanoate, a short chain fatty acid. If, however, oxidation of both long- and short-chain fatty acids is modulated by DRP1-DN, CPT1 is less likely to be the main point of regulation by fragmentation. Parallel comparison of palmitate and hexanoate oxidation in OxPhos-DLBCLs indicated a comparable reduction in the presence of DRP1-DN (Figures 4.5 and 4-S2). Thus, the mechanism underlying regulation of FAO by mitochondrial fragmentation is likely independent of CPT1.

DISCUSSION

The findings described in this chapter are consistent with a model in which a more fragmented mitochondrial network is required for maintaining high FAO capacity in OxPhos-DLBCLs. As such, this chapter highlights distinctions in mitochondrial architecture as a previously unappreciated dimension to the differences in fuel utilization patterns we previously described in DLBCL subsets. These observations give rise to several questions that are the subject of ongoing studies, including the underlying cause of the fragmented mitochondrial network in OxPhos-DLBCLs and the mechanism by which it facilitates FAO.

At the molecular level, it is likely that differences in regulation of pro-fusion and pro-fission GTPases in the two DLBCL subtypes may shift the net balance between fusion and fission toward increased fission in OxPhos-DLBCLs and elevated fusion in BCR-DLBCLs. Consistent with this idea, the enlarged round mitochondria observed in BCR-DLBCLs resemble “mitochondrial bulb” structures reported in HeLa cells following depletion of DRP1 or MFF and the resulting block in fission [20-22]. Efforts are underway to distinguish between these potential

scenarios by directly measuring fusion and fission rates in real time upon co-labeling individual mitochondria with matrix-targeted photo-activatable GFP (mtPAGFP) and TMRE [23].

We predict that potential differences in relative fusion and fission rates between the DLBCL subsets may in turn be linked to differential regulation of the protein machinery in charge of modifying the mitochondrial architecture, including the DRP1, OPA1, and MFN1/2 GTPases. These differences may manifest at the level of protein abundance or post-translational modifications (PTMs) capable of modulating their activity, protein-protein interactions, and mitochondrial localization. Such modifications include, phosphorylation (DRP1) [9, 24, 25], ubiquitination (DRP1, FIS1 and MFN2) [26-28], S-nitrosylation (DRP1) [29], O-GlcNAc modification (DRP1) [30], and SUMOylation (DRP1) [31]. These PTMs can allow remodelling of the mitochondrial network architecture in response to a diverse array of cellular cues and signaling modules [9, 25, 28]. In the context of DLBCL-subtypes, one potential candidate pathway is signaling downstream of the B-cell receptor, a signaling axis that distinguishes the two DLBCL subtypes, and normally inhibits FAO in BCR-DLBCLs (Chapter 2, Figure 2.4B) [12].

Another possible mechanism that would support increased mitochondrial fragmentation in OxPhos-DLBCLs is altered regulation of the factors that recruit DRP1 to the mitochondrial outer membrane, including MFF [20, 32]. Previous biochemical studies and genetic rescue experiments have shown that regulation of MFF protein stability by the HSP90 family protein TRAP1 is an important determinant of mitochondrial network fragmentation [33]. Interestingly, TRAP1 is enriched in mitochondria isolated from OxPhos- compared with BCR-DLBCLs as evident from quantitative proteomics [12] and western blot analysis (Figure 4-S3). This predicts MFF protein may be more stable in OxPhos-DLBCLs, potentially resulting in increased recruitment of DRP1 to mitochondria and greater fission. This possibility remains to be formally tested.

A novel and unexpected finding in our studies is the selective effect of mitochondrial fission on mitochondrial handling of fatty acids as opposed to other fuels. The molecular

underpinnings of this fuel-selective effect are currently unknown. Our data do not support CPT1 and the mitochondrial import of long-chain fatty acids as the main site of regulation by fragmentation. It is possible that the smaller mitochondrial size facilitates mitochondrial juxtaposition near lipid droplets, where fatty acids are stored as triglycerides or activated to their fatty acyl-CoA derivatives and oxidized in the mitochondria [34, 35]. This mechanism, which can directly influence the access of mitochondria to fatty acids, has been predominantly studied in brown adipocytes, a cell type that is normally enriched in lipid droplets and oxidizes fatty acids extensively. Whether a similar mechanism operates in other cell types is not known. Notably, lipid droplets can be detected in OxPhos- and BCR-DLBCL cell lines (Figure 4-S4). Whether juxtaposition of mitochondria near lipid droplets is quantitatively different in OxPhos- and BCR-DLBCLs warrants examination.

Overall, our findings indicate engagement of additional regulatory pathways that influence the FAO capacity and its effect on DLBCL survival. Here, we have identified mitochondrial network dynamics and architecture as one such regulatory pathway that provides an additional component to the metabolic distinction between OxPhos- and BCR-DLBCLs. Understanding the molecular dialogue between FAO and mitochondrial architecture may provide novel insights into fuel utilization pathways in DLBCLs that may be therapeutically exploited. Such insights may also have broader implications for molecular regulation of FAO in other cell types.

MATERIALS AND METHODS

Cell culture

All DLBCL cell lines were grown in RPMI-1640 supplemented with 10% fetal bovine serum, 2 mM L-glutamine, and 1% penicillin/streptomycin as described in Chapter 2.

Western blots

Whole cell lysates were analyzed by 4-12% BisTris NuPage (Invitrogen) gel electrophoresis, transferred to nitrocellulose membrane, and developed with antibodies against DRP1 (Abcam ab56788) or β-Tubulin (Millipore 05-661).

Expression of DRP1-DN in DLBCL cell-lines

The lentiviral vector expressing the K38A dominant mutant of DRP1 was a generous gift of Dr. Orian Shirihai (Boston University). Lentiviral supernatants were generated by standard lentivirus packaging techniques in HEK 293 cells and used to transduce DLBCL cell lines by "spinfection". Briefly, $5x10^5$ cells were centrifuged in 5-8 ml of viral supernatant for 2 hr at 460 *g* at room temperature. Subsequent metabolic assays were done 24 hr after infection.

Mdivi-1 viability assay

Cells were seeded at $2.5x10^5$ cells/ml and treated with 10-30 μM of mdivi-1 (Sigma) or vehicle (DMSO) control for 24 hr. Cell viability was analyzed using the Annexin V/FITC Apoptosis Detection Kit (BD Bioscience) by flow cytometry.

Imaging and quantification of mitochondrial morphology

DLBCL cell lines were stained with 100 nM Mitotracker Red™ (Invitrogen) for 15 min at 37°C, washed in PBS, and incubated for an additional 15 min at 37°C on poly-l-lysine coated glass

coverslips. Cells were then fixed in 4% paraformaldehyde for 30 min at room temperature. Coverslips were then mounted on glass slides using mounting media (Vectashield) and sealed with clear nail polish. Cells were imaged using the 100x objective of a Zeiss LSM 710-Live Duo Scan confocal microscope. 30-40 consecutive Z-stacks were taken at 0.25 μm intervals covering the height of an entire cell. Mitochondrial area was quantified using ImageJ 1.47f. For imaging of mitochondrial morphology in live cells, Pfeiffer and SU-DHL-4 cell lines were infected with lentiviruses carrying mt-dsRed [23] at an MOI of 5 and immobilized in 0.5% agarose/phenol red-free DMEM on MatTek plates. Images were collected on a Zeiss LSM 710-Live Duo Scan confocal microscope using a humidified chamber supplied with 5% CO_2 and maintained at 37°C.

Measurement of oxygen consumption

Mitochondrial oxygen consumption rates (OCR) were measured in real time using the XF24 Extracellular Flux analyzer instrument and the AKOS algorithm v1.7.0.74 software (Seahorse Bioscience Inc., North Billerica, MA). Briefly, 24 hr after lentiviral transduction of DRP1-DN or treatment with mdivi-1, cells were seeded in XF24 V7 plates coated with 22.4 μg/ml Cell Tak (BD Bioscience) at a density of $3x10^5$ cells in 600 μl of sodium bicarbonate-free RPMI supplemented with 0.2 mM palmitate/0.5 mM carnitine, 0.5 mM hexanoate, or 2 mM L-glutamine. OCR was measured for 3 min periods with 5 min intervals between consecutive measurements. To measure ATP-coupled respiration, oligomycin was injected at a final concentration of 2.5 μM using the instrument's injection ports after the first three OCR measurements.

Statistical Analysis

All values are presented as mean ± SEM. Statistical significance was determined using two-tailed Student's t-test assuming unequal variance. Significance indicated by p-values as follows: *$p < 0.05$, **$p < 0.01$, ***$p < 0.001$.

Contributions:

Illana Stanley conceived this project and performed all of the experiments presented in this chapter, including image collection and analysis, knockdown studies, cell death and respirometry assays. Generous guidance and expertise were provided on imaging by Marc Liesa and Orian Shirihai (Boston University).

REFERENCES

1. Lackner, L.L. and J.M. Nunnari, *The molecular mechanism and cellular functions of mitochondrial division.* Biochim Biophys Acta, 2009. **1792**(12): p. 1138-44.

2. Otera, H., N. Ishihara, and K. Mihara, *New insights into the function and regulation of mitochondrial fission.* Biochim Biophys Acta, 2013. **1833**(5): p. 1256-68.

3. Elgass, K., et al., *Recent advances into the understanding of mitochondrial fission.* Biochim Biophys Acta, 2013. **1833**(1): p. 150-61.

4. Li, H., et al., *Bcl-xL induces Drp1-dependent synapse formation in cultured hippocampal neurons.* Proc Natl Acad Sci U S A, 2008. **105**(6): p. 2169-74.

5. Karbowski, M., et al., *Spatial and temporal association of Bax with mitochondrial fission sites, Drp1, and Mfn2 during apoptosis.* J Cell Biol, 2002. **159**(6): p. 931-8.

6. Frank, S., et al., *The role of dynamin-related protein 1, a mediator of mitochondrial fission, in apoptosis.* Dev Cell, 2001. **1**(4): p. 515-25.

7. Delivani, P., et al., *Role for CED-9 and Egl-1 as regulators of mitochondrial fission and fusion dynamics.* Mol Cell, 2006. **21**(6): p. 761-73.

8. Liesa, M. and O.S. Shirihai, *Mitochondrial dynamics in the regulation of nutrient utilization and energy expenditure.* Cell Metab, 2013. **17**(4): p. 491-506.

9. Gomes, L.C., G. Di Benedetto, and L. Scorrano, *During autophagy mitochondria elongate, are spared from degradation and sustain cell viability.* Nat Cell Biol, 2011. **13**(5): p. 589-98.

10. Molina, A.J., et al., *Mitochondrial networking protects beta-cells from nutrient-induced apoptosis.* Diabetes, 2009. **58**(10): p. 2303-15.

11. Cogliati, S., et al., *Mitochondrial cristae shape determines respiratory chain supercomplexes assembly and respiratory efficiency.* Cell, 2013. **155**(1): p. 160-71.

12. Caro, P., et al., *Metabolic signatures uncover distinct targets in molecular subsets of diffuse large B cell lymphoma.* Cancer Cell, 2012. **22**(4): p. 547-60.

13. Young, R.M. and L.M. Staudt, *Targeting pathological B cell receptor signalling in lymphoid malignancies.* Nat Rev Drug Discov, 2013. **12**(3): p. 229-43.

14. Juszczynski, P., et al., *BCL6 modulates tonic BCR signaling in diffuse large B-cell lymphomas by repressing the SYK phosphatase, PTPROt.* Blood, 2009. **114**(26): p. 5315-21.

15. Chen, L., et al., *SYK inhibition modulates distinct PI3K/AKT- dependent survival pathways and cholesterol biosynthesis in diffuse large B cell lymphomas.* Cancer Cell, 2013. **23**(6): p. 826-38.

16. Chen, L., et al., *SYK-dependent tonic B-cell receptor signaling is a rational treatment target in diffuse large B-cell lymphoma.* Blood, 2008. **111**(4): p. 2230-7.

17. Smirnova, E., et al., *Dynamin-related protein Drp1 is required for mitochondrial division in mammalian cells.* Mol Biol Cell, 2001. **12**(8): p. 2245-56.

18. Cassidy-Stone, A., et al., *Chemical inhibition of the mitochondrial division dynamin reveals its role in Bax/Bak-dependent mitochondrial outer membrane permeabilization.* Dev Cell, 2008. **14**(2): p. 193-204.

19. Houten, S.M. and R.J. Wanders, *A general introduction to the biochemistry of mitochondrial fatty acid beta-oxidation.* J Inherit Metab Dis, 2010. **33**(5): p. 469-77.

20. Otera, H., et al., *Mff is an essential factor for mitochondrial recruitment of Drp1 during mitochondrial fission in mammalian cells.* J Cell Biol, 2010. **191**(6): p. 1141-58.

21. Mopert, K., et al., *Loss of Drp1 function alters OPA1 processing and changes mitochondrial membrane organization.* Exp Cell Res, 2009. **315**(13): p. 2165-80.

22. Ban-Ishihara, R., et al., *Dynamics of nucleoid structure regulated by mitochondrial fission contributes to cristae reformation and release of cytochrome c.* Proc Natl Acad Sci U S A, 2013. **110**(29): p. 11863-8.

23. Twig, G., et al., *Fission and selective fusion govern mitochondrial segregation and elimination by autophagy.* EMBO J, 2008. **27**(2): p. 433-46.

24. Cribbs, J.T. and S. Strack, *Reversible phosphorylation of Drp1 by cyclic AMP-dependent protein kinase and calcineurin regulates mitochondrial fission and cell death.* EMBO Rep, 2007. **8**(10): p. 939-44.

25. Taguchi, N., et al., *Mitotic phosphorylation of dynamin-related GTPase Drp1 participates in mitochondrial fission.* J Biol Chem, 2007. **282**(15): p. 11521-9.

26. Yonashiro, R., et al., *A novel mitochondrial ubiquitin ligase plays a critical role in mitochondrial dynamics.* EMBO J, 2006. **25**(15): p. 3618-26.

27. Karbowski, M., A. Neutzner, and R.J. Youle, *The mitochondrial E3 ubiquitin ligase MARCH5 is required for Drp1 dependent mitochondrial division.* J Cell Biol, 2007. **178**(1): p. 71-84.

28. Chen, Y. and G.W. Dorn, 2nd, *PINK1-phosphorylated mitofusin 2 is a Parkin receptor for culling damaged mitochondria.* Science, 2013. **340**(6131): p. 471-5.

29. Guo, C., et al., *SENP3-mediated deSUMOylation of dynamin-related protein 1 promotes cell death following ischaemia.* EMBO J, 2013. **32**(11): p. 1514-28.

30. Gawlowski, T., et al., *Modulation of dynamin-related protein 1 (DRP1) function by increased O-linked-beta-N-acetylglucosamine modification (O-GlcNAc) in cardiac myocytes.* J Biol Chem, 2012. **287**(35): p. 30024-34.

31. Braschi, E., R. Zunino, and H.M. McBride, *MAPL is a new mitochondrial SUMO E3 ligase that regulates mitochondrial fission.* EMBO Rep, 2009. **10**(7): p. 748-54.

32. Gandre-Babbe, S. and A.M. van der Bliek, *The novel tail-anchored membrane protein Mff controls mitochondrial and peroxisomal fission in mammalian cells.* Mol Biol Cell, 2008. **19**(6): p. 2402-12.

33. Takamura, H., et al., *TRAP1 controls mitochondrial fusion/fission balance through Drp1 and Mff expression.* PLoS One, 2012. **7**(12): p. e51912.

34. Wikstrom, J.D., et al., *Hormone-induced mitochondrial fission is utilized by brown adipocytes as an amplification pathway for energy expenditure.* EMBO J, 2014. **33**(5): p. 418-36.

35. Wang, H., et al., *Perilipin 5, a lipid droplet-associated protein, provides physical and metabolic linkage to mitochondria.* J Lipid Res, 2011. **52**(12): p. 2159-68.

Chapter 5

Discussion and Future Directions

The investigation of metabolic profiles in DLBCL subsets has revealed several functional distinctions in the OxPhos subtype compared to the BCR-dependent subtype, including reliance on elevated ETC activity, FAO, the mitochondrial translation pathway, and a fragmented mitochondrial network architecture. Comparison of glucose and non-glucose fuel utilization pathways and mitochondrial bioenergetics in these two DLBCL subsets provided insights into the degree of metabolic heterogeneity that may exist within a given cancer type and alternative metabolic programs to aerobic glycolysis. The findings described in the previous chapters have also given rise to additional hypotheses and research opportunities that will lay the foundation for future investigations, three of which are highlighted in the following sections; the link between metabolic profiles of DLBCL subsets and normal developing B lymphocytes, the molecular pathways that contribute to higher ETC activity but lower ROS content in OxPhos-DLBCLs, and therapeutic implications of metabolic distinctions identified in DLBCL subsets.

The potential connection between metabolic profiles of DLBCL subtypes and normal developing B lymphocytes

One of the questions arising from this work is whether the metabolic profiles of DLBCL subtypes are acquired *de novo* during lymphomagenesis or they resemble certain metabolic features of normal B lymphocyte subsets. DLBCLs arise from germinal centers (GCs), a site of B-cell development where mature B-cells are activated upon encountering their cognate antigen and signals from T-cells [1]. Upon activation, germinal center B-cells can have several distinct fates. They can rapidly divide as centroblasts and subsequently undergo apoptosis or further differentiate into antibody secreting plasma cells or non-secreting memory B-cells that can be activated to produce antibodies upon antigen re-exposure [1]. These developmental cell fates are regulated by complex arrays of transcription factors and signaling pathways [2]. Because B-cell activation in the GCs is further linked to immunoglobulin class switching and somatic hypermutation, two processes that involve DNA modifications and chromosomal breaks to

modify the BCR's affinity for antigens, the GC phase of B-cell development is especially prone to mutations and chromosomal translocations leading to lymphomagenesis. While the precise origin of DLBCLs in the GC is debated, highly proliferating centroblasts and plasmablasts have been proposed as putative origins [2]. This suggests that DLBCLs may share certain features of a normal germinal center B-cell differentiation program.

The different stages of germinal center B-cell development, including proliferation, DNA modifications, antibody production and secretion, are bioenergetically and biosynthetically demanding processes. The exact metabolic profile of naïve (antigen-inexperienced) and activated (antigen-experienced) B-cells or long-term antibody producing plasma cells and memory B-cells are debated. Comparative metabolomics revealed that naïve B-cells perform oxidative phosphorylation, and following engagement of their BCR by antigen, they switch to aerobic glycolysis [3]. The Warburg-type profile of activated B-cells is consistent with the metabolic characteristics of many proliferating cell types and the metabolic switch associated with the transition from a quiescent to proliferative state [4, 5]. This might also parallel the Warburg-type metabolic profile of BCR-DLBCLs (Chapter 2, Figures 2.8A and 2.11) and is further consistent with published reports that BCR-stimulation of normal B-cells leads to a PI3K/AKT-dependent up-regulation of glucose uptake and glycolysis [6]. A switch from oxidative phosphorylation to aerobic glycolysis has also been reported in the transition of naïve to activated T lymphocytes [7-9]. Notably, oxidative phosphorylation in naïve T-cells is linked to increased FAO [10], but increased FAO has not been reported in naïve B-cells. A recent study has revealed a more complex landscape of metabolic pathways in activated B-cells, suggesting that, unlike activated T-cells, activated B-cells demonstrate a concomitant up-regulation of glycolysis and oxidative phosphorylation [11]. Specifically, the rate of glycolysis is higher in B-cells than T-cells, and following B-cell activation, oxidative phosphorylation is proportionally increased. The precise substrates oxidized by mitochondria in this setting (glucose, fatty acids, amino acids) have not yet been determined. In addition, if and how the balance between

glycolysis and oxidative phosphorylation changes once activated B-cells further differentiate to plasma or memory cells merits future examination. Within this context, the metabolic requirements of antibody production by plasma cells are likely complex. While glucose metabolism has been shown to be important [11], the physiologic contribution of mitochondrial pathways to antibody production has not been determined. This is especially relevant as mitochondrial function can affect the calcium and energy requirements of the secretory pathway and release of antibodies. Consistent with this idea, a previous study showed that, PPARγ, which can activate the expression of oxidative phosphorylation and FAO genes, is important for antibody production by B-cells [12].

While BCR-DLBCLs appear to be metabolically similar to activated B-cells in terms of aerobic glycolysis, it is unclear which stages of germinal center B-cell differentiation might be most similar to the metabolic features of OxPhos-DLBCLs. Similar to naïve B-cells, OxPhos-DLBCLs display increased oxidative phosphorylation. At the same time, the lack of a functional BCR in these lymphomas is reminiscent of anergic B-cells that are desensitized to BCR engagement [11, 13]. Yet, unlike anergic B-cells, OxPhos-DLBCLs have high metabolic capacity. Knowledge of the precise metabolic alterations occurring as mature B-cells enter and develop through the germinal center will help expand the metabolic landscape of B-cell development and identify potential metabolic characteristics that might be shared with OxPhos-DLBCLs.

Additional mitochondrial homeostatic pathways that may help maintain high ETC activity and low ROS in OxPhos-DLBCLs

The reliance of OxPhos-DLBCLs on mitochondrial metabolism, and specifically increased ETC activity, for a significant portion of overall cellular energy budget (Chapter 2, Figures 2.9A and 2.11A), together with up-regulation of the mitochondrial translation pathway necessary for synthesis of mtDNA-encoded ETC subunits (Chapter 3, Figure 3.2), point to the

paramount importance of ETC function in OxPhos-DLBCLs. Remarkably, increased ETC activity in this subtype is not associated with higher cellular mitochondrial superoxide content (Chapter 2, Figure 2.12A), which is otherwise expected due to increased electron transfer reactions. Lower ROS content can, in part, be explained by higher antioxidant mechanisms as indicated by greater GSH content and increased expression of several antioxidant enzymes such as SOD2 in OxPhos-DLBCLs, and the observation that interference with ROS detoxification is selectively toxic to OxPhos-DLBCLs (Chapter 2, Figure 2.12C). However, because steady state ROS content reflects the net balance of ROS production and detoxification, it is also possible that lower mitochondrial ROS in OxPhos-DLBCLs is reflective of highly efficient mitochondria that generate less ROS while harboring high ETC activity. To help address this possibility, two mitochondrial homeostatic mechanisms merit consideration: organization of ETC complexes into supercomplexes that are more efficient at electron transport, and prompt clearance of inefficient or damaged mitochondria from the mitochondrial network through mitophagy.

***The bioenergetic benefits of ETC supercomplexes*.** ETC complexes were traditionally thought to be individually embedded in a fluid mitochondrial membrane, interacting by random diffusion. However, this traditional view has been revised based on findings over the last decade that the ETC complexes are capable of forming higher order structures to facilitate electron flow by substrate channeling. Complexes I, III and IV can be found in respiratory supercomplexes (RSCs) that are dedicated to NADH-linked oxidation. Complex II is not found in such supercomplexes and is dedicated to $FADH_2$-linked oxidation [14]. Different carbon fuels generate different ratios of reducing equivalents. For example, glucose oxidation generates more NADH, while FAO generates more $FADH_2$, and there is evidence that assembly of the supercomplexes can be regulated to optimize nutrient utilization [15]. It has also been shown that incorporation of ETC complexes in RSCs reduces the amount of mitochondrial superoxide generated by complex I, suggesting that RSC formation is relevant for reduction of oxidative

stress [16]. Whether differences in RSC formation can contribute to increased ETC activity while lowering mitochondrial superoxide production in OxPhos-DLBCLs warrants future investigation.

Mitochondrial quality control through mitophagy. Mitophagy, the selective degradation of damaged mitochondria by autophagy, is a mitochondrial quality control mechanism that lowers the cellular mitochondrial superoxide levels and maintains efficient oxidative phosphorylation [17-19], both central metabolic characteristics of OxPhos-DLBCLs. Mitophagy is coordinated with mitochondrial fusion/fission dynamics [20]. Specifically, mitochondrial fission helps "pinch off" damaged mitochondria from the rest of the mitochondrial network. In addition, the mechanisms of fusion are dependent upon respiratory function and mitochondrial membrane potential [20]. Damaged mitochondria have lower membrane potential and are fusion deficient, and are therefore prevented from fusing back with the healthy mitochondrial pool. Mitophagy completes this clearance process by degrading damaged mitochondria, thus removing and recycling mitochondrial components as well as preventing the increased ROS generation that can occur in a damaged respiratory chain or suboptimal mitochondrion [21]. Several initial observations are consistent with the likelihood of increased mitophagy in OxPhos- compared to BCR-DLBCLs. First, autophagic flux is elevated in OxPhos-DLBCL cell lines compared to cells of the BCR subtype. Importantly, inhibition of autophagy leads to higher accumulation of mitochondrial superoxide and selective death of OxPhos-DLBCL cell lines without affecting the survival of BCR-DLBCLs (Stanley and Danial, unpublished observations). Second, co-localization of LC3-II and mitochondria, an indication of mitochondrial localization to autophagosomes, tends to be greater in OxPhos-DLBCLs. Third, a potential increase in mitophagy would be consistent with smaller mitochondrial surface area and a fragmented mitochondrial network in OxPhos-DLBCLs (Chapter 4, Figure 4.2), which can be easily engulfed by autophagosomes. This warrants a more thorough investigation of the contribution of

mitophagy to increased ETC efficiency, diminished intracellular ROS content, and survival of OxPhos-DLBCLs.

Potential therapeutic implications

Given the genetic and clinical heterogeneity of DLBCL, strategies to stratify patients, predict chemotherapeutic response, identify diagnostic markers and discover subtype-selective therapeutic targets will greatly improve DLBCL therapy and management. By identifying, characterizing and testing the contribution of metabolic pathways relevant to DLBCLs, in particular the BCR-independent/OxPhos subtype of DLBCL, the work described in this dissertation has the potential to unravel novel therapeutic targets, as well as resistance mechanisms to current therapies aimed at BCR initiated survival signaling that are normally operative in BCR-dependent DLBCLs. Furthermore, given that the BCR signaling pathway includes canonical pro-survival signaling nodes such as PI3K/AKT and mTOR that are highly relevant to a number of other cancer types, BCR-independent survival mechanisms may have broader implications to other tumors.

***Targeted therapies and resistance mechanisms to BCR inhibition*.** Identification and characterization of molecular signatures in DLBCLs has provided great insights into both the molecular pathogenesis of these tumors as well as targetable pathways. To date such molecular signatures have been predominantly based on gene expression profiling and associated mutations/chromosomal alterations that have uncovered dominant survival mechanisms in DLBCL [2, 22-24]. Among these, the BCR signaling axis and the genetic alterations that lead to increased activity of its downstream components, including NF-κB, PI3K/AKT, SYK and BTK, are actively pursued for their therapeutic utility in BCR-dependent DLBCLs. The BCR-independent survival characteristics of OxPhos-DLBCLs renders them refractory to BCR inhibition. The work described in this dissertation has begun to characterize

BCR-independent survival signaling that, in the fullness of time, may be therapeutically relevant. In particular, certain small molecule inhibitors of FAO and the mitochondrial translation pathway are approved for use in cancer or other disease indications [25-28]. Importantly, the findings that acute inhibition of BCR signaling in BCR-DLBCLs is sufficient to increase/disinhibit FAO indicates a reciprocal relationship between BCR signaling and FAO. As FAO can provide proliferation and survival benefits independent of the BCR, these observations may have broader implications for lymphomas that have lost dependency on the BCR pathway or acquired resistance to inhibitors of this signaling axis. As such, dissection of the molecular link between BCR signaling and FAO will likely provide valuable insights. Thus, characterization of BCR-independent survival mechanisms will not only be relevant to understanding the molecular pathogenesis of OxPhos-DLBCLs but also unravel potential resistance mechanisms to BCR-targeted interventions.

Diagnostic utility of metabolic distinctions in DLBCL subtypes. In light of the metabolic distinctions in DLBCL subtypes with respect to glucose and fatty acid metabolism, investigation of the utility of glycolysis and FAO probes for diagnostic and functional imaging of DLBCL subtypes is warranted. FDG-PET imaging is routine in clinical care for DLBCLs. The selectivity of ^{18}F-FDG-PET for cancer over normal tissue is due to increased glucose metabolism in many tumors [29]. Previous analyses of FDG uptake revealed a broad range of avidity in newly diagnosed DLBCLs. The possibility that BCR/Warburg-type and OxPhos-type DLBCLs differ in their FDG uptake may explain the broad range of FDG avidity seen in newly diagnosed DLBCL patients and requires investigation. As such, comparison of the FDG uptake profiles of patient cohorts for which CCC classification is already available with tumors designated as OxPhos- or BCR-type will be very informative. Another useful approach would be FDG-PET imaging of OxPhos- and BCR-DLBCL xenografts in mice. Based on the metabolic profiles described in Chapter 2, BCR-DLBCLs are predicted to be more FDG-PET avid than OxPhos-DLBCLs. In

addition, FAO imaging probes such as [^{18}F]fluoro-4-thia-oleate (FTO) [30] may be tested in similar settings. Based on the findings discussed in this dissertation, ^{18}F-FTO radioactivity is predicted to be higher in OxPhos-DLBCLs.

***A pan OxPhos metabolic signature and its broader implications in other heterogeneous cancers*.** The proteome- and metabolome-level signatures that emerged from integrative metabolic analysis of DLBCL subsets expanded the original mitochondrial gene signature of OxPhos-DLBCLs to include functionally validated and biologically relevant pathways of fuel utilization and associated vulnerabilities in DLBCL subsets. The expanded set of genes selectively enriched in OxPhos-DLBCLs and multiple validated functional readouts for "OxPhos-ness" provides a unique opportunity to develop, test and validate a parsimonious classifier of OxPhos versus non-OxPhos distinction that may then serve as a powerful tool to interrogate other heterogeneous groups of tumors for the presence of similar metabolic heterogeneity and subtype-specific targets.

REFERENCES

1. Zotos, D. and D.M. Tarlinton, *Determining germinal centre B cell fate.* Trends Immunol, 2012. **33**(6): p. 281-8.

2. Lenz, G. and L.M. Staudt, *Aggressive lymphomas.* N Engl J Med, 2010. **362**(15): p. 1417-29.

3. Garcia-Manteiga, J.M., et al., *Metabolomics of B to plasma cell differentiation.* J Proteome Res, 2011. **10**(9): p. 4165-76.

4. Lunt, S.Y. and M.G. Vander Heiden, *Aerobic glycolysis: meeting the metabolic requirements of cell proliferation.* Annu Rev Cell Dev Biol, 2011. **27**: p. 441-64.

5. Stanley, I.A., et al., *Changing appetites: the adaptive advantages of fuel choice.* Trends Cell Biol, 2014. **24**(2): p. 118-27.

6. Dufort, F.J., et al., *Cutting edge: IL-4-mediated protection of primary B lymphocytes from apoptosis via Stat6-dependent regulation of glycolytic metabolism.* J Immunol, 2007. **179**(8): p. 4953-7.

7. Carr, E.L., et al., *Glutamine uptake and metabolism are coordinately regulated by ERK/MAPK during T lymphocyte activation.* J Immunol, 2010. **185**(2): p. 1037-44.

8. Frauwirth, K.A., et al., *The CD28 signaling pathway regulates glucose metabolism.* Immunity, 2002. **16**(6): p. 769-77.

9. Sinclair, L.V., et al., *Control of amino-acid transport by antigen receptors coordinates the metabolic reprogramming essential for T cell differentiation.* Nat Immunol, 2013. **14**(5): p. 500-8.

10. Bental, M. and C. Deutsch, *Metabolic changes in activated T cells: an NMR study of human peripheral blood lymphocytes.* Magn Reson Med, 1993. **29**(3): p. 317-26.

11. Caro-Maldonado, A., et al., *Metabolic reprogramming is required for antibody production that is suppressed in anergic but exaggerated in chronically BAFF-exposed B cells.* J Immunol, 2014. **192**(8): p. 3626-36.

12. Garcia-Bates, T.M., et al., *Peroxisome proliferator-activated receptor gamma ligands enhance human B cell antibody production and differentiation.* J Immunol, 2009. **183**(11): p. 6903-12.

13. Yarkoni, Y., A. Getahun, and J.C. Cambier, *Molecular underpinning of B-cell anergy.* Immunol Rev, 2010. **237**(1): p. 249-63.

14. Genova, M.L. and G. Lenaz, *Functional role of mitochondrial respiratory supercomplexes.* Biochim Biophys Acta, 2014. **1837**(4): p. 427-43.

15. Lapuente-Brun, E., et al., *Supercomplex assembly determines electron flux in the mitochondrial electron transport chain.* Science, 2013. **340**(6140): p. 1567-70.

16. Maranzana, E., et al., *Mitochondrial respiratory supercomplex association limits production of reactive oxygen species from complex I.* Antioxid Redox Signal, 2013. **19**(13): p. 1469-80.

17. Chen, Y. and G.W. Dorn, 2nd, *PINK1-phosphorylated mitofusin 2 is a Parkin receptor for culling damaged mitochondria.* Science, 2013. **340**(6131): p. 471-5.

18. Cui, T., et al., *Silencing of PINK1 induces mitophagy via mitochondrial permeability transition in dopaminergic MN9D cells.* Brain Res, 2011. **1394**: p. 1-13.

19. Glick, D., et al., *BNip3 regulates mitochondrial function and lipid metabolism in the liver.* Mol Cell Biol, 2012. **32**(13): p. 2570-84.

20. Gottlieb, R.A. and A.B. Gustafsson, *Mitochondrial turnover in the heart.* Biochim Biophys Acta, 2011. **1813**(7): p. 1295-301.

21. Twig, G. and O.S. Shirihai, *The interplay between mitochondrial dynamics and mitophagy.* Antioxid Redox Signal, 2011. **14**(10): p. 1939-51.

22. Abramson, J.S. and M.A. Shipp, *Advances in the biology and therapy of diffuse large B-cell lymphoma: moving toward a molecularly targeted approach.* Blood, 2005. **106**(4): p. 1164-74.

23. Jardin, F., *Next generation sequencing and the management of diffuse large B-cell lymphoma: from whole exome analysis to targeted therapy.* Discov Med, 2014. **18**(97): p. 51-65.

24. Lohr, J.G., et al., *Discovery and prioritization of somatic mutations in diffuse large B-cell lymphoma (DLBCL) by whole-exome sequencing.* Proc Natl Acad Sci U S A, 2012. **109**(10): p. 3879-84.

25. Zidkova, H., et al., *[Extensive metastases of Ewing's sarcoma in the adreno-renal area].* Cesk Radiol, 1990. **44**(1): p. 37-40.

26. Wenzel, R., G. Bate, and P. Kirkpatrick, *Tigecycline.* Nat Rev Drug Discov, 2005. **4**(10): p. 809-10.

27. Kantor, P.F., et al., *The antianginal drug trimetazidine shifts cardiac energy metabolism from fatty acid oxidation to glucose oxidation by inhibiting mitochondrial long-chain 3-ketoacyl coenzyme A thiolase.* Circ Res, 2000. **86**(5): p. 580-8.

28. Skrtic, M., et al., *Inhibition of mitochondrial translation as a therapeutic strategy for human acute myeloid leukemia.* Cancer Cell, 2011. **20**(5): p. 674-88.

29. Jadvar, H., *Prostate cancer: PET with 18F-FDG, 18F- or 11C-acetate, and 18F- or 11C-choline.* J Nucl Med, 2011. **52**(1): p. 81-9.

30. Pandey, M.K., et al., *Structure dependence of long-chain [18F]fluorothia fatty acids as myocardial fatty acid oxidation probes.* J Med Chem, 2012. **55**(23): p. 10674-84.

APPENDIX

List of Publications

Caro, P., A. U. Kishan, E. Norberg, **I. A. Stanley**, B. Chapuy, S. B. Ficarro, K. Polak, D. Tondera, J. Gounarides, H. Yin, F. Zhou, M. R. Green, L. Chen, S. Monti, J. A. Marto, M. A. Shipp and N. N. Danial (2012). "*Metabolic signatures uncover distinct targets in molecular subsets of diffuse large B cell lymphoma.*" Cancer Cell **22**(4): 547-560. *Journal Cover and Featured Article*

Featured in:

- Previews, *Cancer cell* 22:423-4, 2012. DeBerardinis, R. A mitochondrial power play in lymphoma.

- News and Research Watch, *Cancer Discovery*. October 25, 2012. McKenna, E.S. Diffuse Large B Cell Lymphomas Are Metabolically Heterogeneous (http://cdnews.aacrjournals.org/node/16242**)**

Akbay, E. A., J. Moslehi, C. L. Christensen, S. Saha, J. H. Tchaicha, S. H. Ramkissoon, K. M. Stewart, J. Carretero, E. Kikuchi, H. Zhang, T. J. Cohoon, S. Murray, W. Liu, K. Uno, S. Fisch, K. Jones, S. Gurumurthy, C. Gliser, S. Choe, M. Keenan, J. Son, **I. Stanley,** J. A. Losman, R. Padera, R. T. Bronson, J. M. Asara, O. Abdel-Wahab, P. C. Amrein, A. T. Fathi, N. N. Danial, A. C. Kimmelman, A. L. Kung, K. L. Ligon, K. E. Yen, W. G. Kaelin, Jr., N. Bardeesy and K. K. Wong (2014). "*D-2-hydroxyglutarate produced by mutant IDH2 causes cardiomyopathy and neurodegeneration in mice.*" Genes Dev **28**(5): 479-490.

Stanley, I. A., S. M. Ribeiro, A. Gimenez-Cassina, E. Norberg and N. N. Danial (2014). "*Changing appetites: the adaptive advantages of fuel choice.*" Trends Cell Biol **24**(2): 118-127.

Submission pending

Norberg E.*, **I. A. Stanley***, S. Ficarro, B. Chapuy, L. Chen, E. Patton, S. Rodig, M. A. Shipp, J. Marto, N.N. Danial. "*Differential contribution of the mitochondrial translation pathway to the survival of Diffuse Large B-cell Lymphoma*"

*co-first authors

Supplementary Figures and Tables

Figure 2-S1. Comparison of mitochondrial proteome via 2D-DIGE
2D-DIGE comparison of mitochondria isolated from Karpas 422 (OxPhos) and OCI-Ly1 (BCR) DLBCL cell lines. Equivalent amounts of mitochondrial protein lysates from OCI-Ly1 and Karpas 422 cell lines were labeled with Cy3 and Cy5 DIGE fluors, respectively, mixed and resolved on a 2D analytical gel (Applied Biomics, inc. Hayward, CA) (left panel). Image scans were carried out and the differential protein expressions (Cy5/Cy3) were determined using DeCyder software (version 6.5, GE-Healthcare). Proteins that were ≥ 2.5 fold more abundant in OxPhos-DLBCL were picked by Ettan Spot Picker (GE-Healthcare) and subjected to in-gel trypsin digestion, peptide extraction, desalting, and MALDI-TOF/TOF mass spectrometry (Applied Biosystems). Protein species in red display higher abundance in the OxPhos-DLBCL cell line Karpas 422. pI, iso-electric point. Identity and metabolic function of up-regulated mitochondrial proteins in Karpas 422 are shown in the right panel.

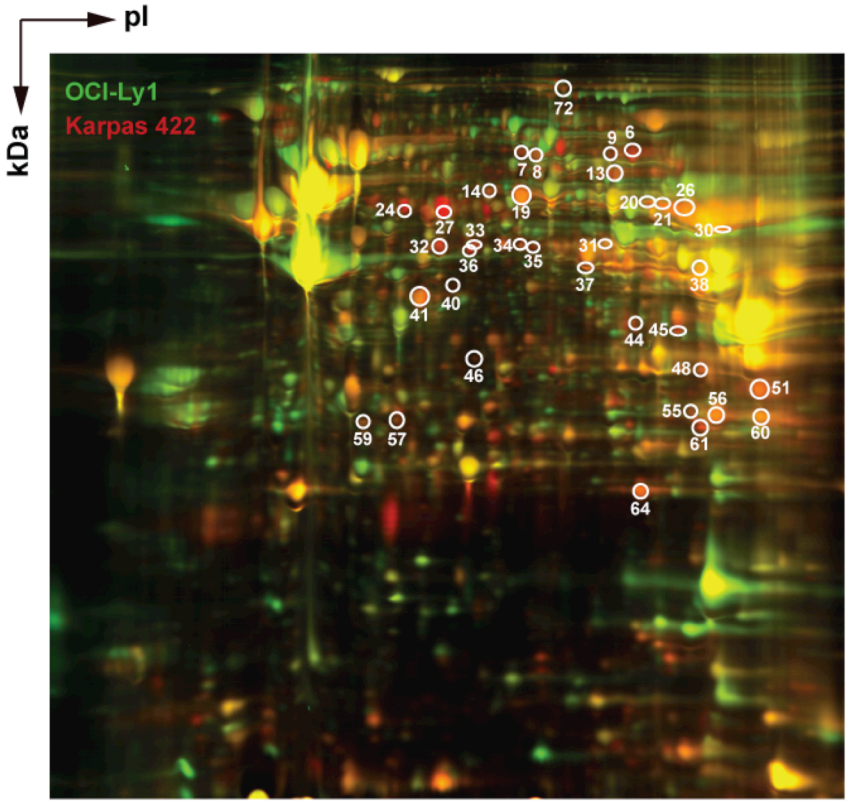

Spot ID and Gene Symbol	Peptide Count	Protein Name	Metabolic Pathway
6- PCK2	31	Phosphoenolpyruvate carboxykinase (mitochondrial)	TCA cycle
7- SDHA	20	Succinate dehydrogenase subunit A	TCA cycle
8- SDHA	21	Succinate dehydrogenase subunit A	TCA cycle
9- PCK2	32	Phosphoenolpyruvate carboxykinase 2 (mitochondrial)	TCA cycle
13- AIF	20	Apoptosis Inducing Factor (Aif)	OXPHOS
14- OXCT1	16	3-oxoacid CoA transferase 1 precursor	Ketone body metabolism
19- OXCT1	16	3-oxoacid CoA transferase 1 precursor	Ketone body metabolism
20- ALDH5A1	12	Aldehyde dehydrogenase 5A1, succinate semialdehyde dehydrogenase	Amino acid metabolism
21- ATP5A	18	ATP synthase F1 complex a subunit	OXPHOS
24- ALDH2	21	Mitochondrial aldehyde dehydrogenase	Amino acid and alcohol metabolism
26- ATP5A	19	ATP synthase F1 complex a subunit	OXPHOS
27- ALDH2	23	Mitochondrial aldehyde dehydrogenase	Amino acid and alcohol metabolism
30- SHMT2	21	Mitochondrial serine hydroxymethyltransferase	Amino acid metabolism
31- PDH	13	Pyruvate dehydrogenase	TCA cycle
32- LC25A24	20	Mitochondrial carrier protein (ANT1)	ADP, ATP transport
33- LC25A24	20	Mitochondrial carrier protein (ANT1)	ADP, ATP transport
34- NDUFS2	20	Mitochondrial carrier portein (ANT1)	ADP, ATP transport
35- NDUFS2	22	NADH dehydrogenase (ubiquinone) Fe-S protein 2	Electron transport
36- OAT	27	Ornithine aminotransferase precursor	Amino acid metabolism
37- MCAD	21	Medium chain acyl- CoA dehydrogenase	Mitochondrial b-oxidation
38- ACAT1	14	Mitochondrial acetoacetyl-CoA thiolase (T2)	Ketone body metabolism
40- OXCT1	11	3-oxoacid CoA transferase 1 precursor	Ketone body metabolism
41- IDH3A	17	Isocitrate dehydrogenase 3 (NAD+) a precursor	TCA cycle
44- TOM40	11	Translocase of outer mitochondrial membrane	Mitochondrial protein import
45- MTHFD2	12	Methylenetetrahydrofolate dehydrogenase	One carbon metabolism
46- NDUFA1	14	Complex I a subcomplex assembly factor 1	Electron transport
48- HADH	8	Hydroxyacyl-CoA dehydrogenase	Mitochondrial b-oxidation
51- VDAC3	13	Voltage-dependent anion channel 3	Translocation of adenine nucleotides
55- AK2	10	Adenylate kinase 2	Transfer of phosphate between ATP and AMP
56- ETF	11	Electron-transfer-flavoprotein	Mitochondrial b-oxidation
57- ECHS1	6	Enoyl-CoA hydratase short Chain 1	Mitochondrial b-oxidation
59- NDUFS3	17	Complex I Fe-S protein 3	Electron transport
60- SDHB	13	Succinate dehydrogenase subunit B	TCA cycle
61- AK2	11	Adenylate kinase 2	Transfer of phosphate between ATP and AMP
64- SOD2	12	Superoxide dismutase [Mn], mitochondrial	ROS detoxification
72- OGDH	40	Oxoglutarate (a-ketoglutarate) dehydrogenase	TCA cycle

Figure 2-S1. (continued)

Figure 2-S2. iTRAQ-based quantitative comparison of DLBCL mitochondrial proteome
Schematics of analytical work flow for multiplex iTRAQ analysis of mitochondria isolated from DLBCL cell lines. Mitochondria isolated from the indicated DLBCL cell lines were subjected to tryptic digestion and iTRAQ labeling and analyzed by LC-MS/MS as described in Chapter 2. MS files were searched using Mascot version 2.2.1 against a forward-reversed human (38190 forward entries) NCBI refseq database with an appended cRAP database of 752 entries. An excel spreadsheet containing the Mascot search results was generated using Multiplierz version 0.8.3. Abundance ratios for the protein candidates within the mitochondrial protein signature (defined in Figure 2-S1) were derived by summing reporters for all peptides mapping to unique genes across replicates. Only genes represented by 2 or more unique peptides are reported. See Chapter 2 for additional details on data collection and analysis.

B

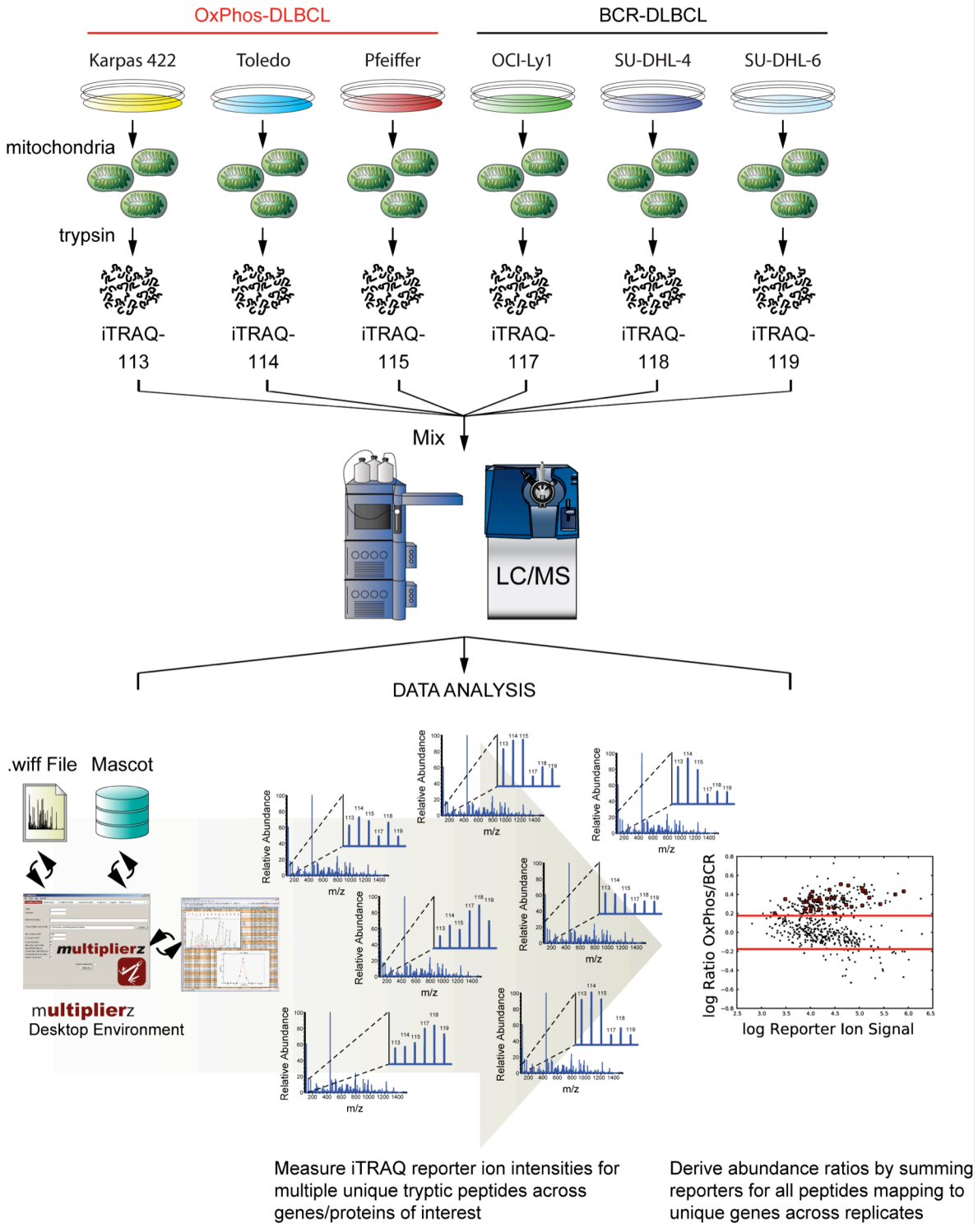

Figure 2-S2. (continued)

Figure 2-S3. Mitochondrial carbon substrate oxidation in DLBCL subsets
Basal (top) and ATP-coupled (bottom) OCR in individual DLBCL cell lines. For each cell line, the mean of 7-13 independent respirometry experiments (independent days and independent plates and cartridges for the XF24 flux analyzer instrument) is shown. NS denotes no substrate added exogenously. Cumulative data for all cell lines per subtype are shown in main Figure 2.4A.

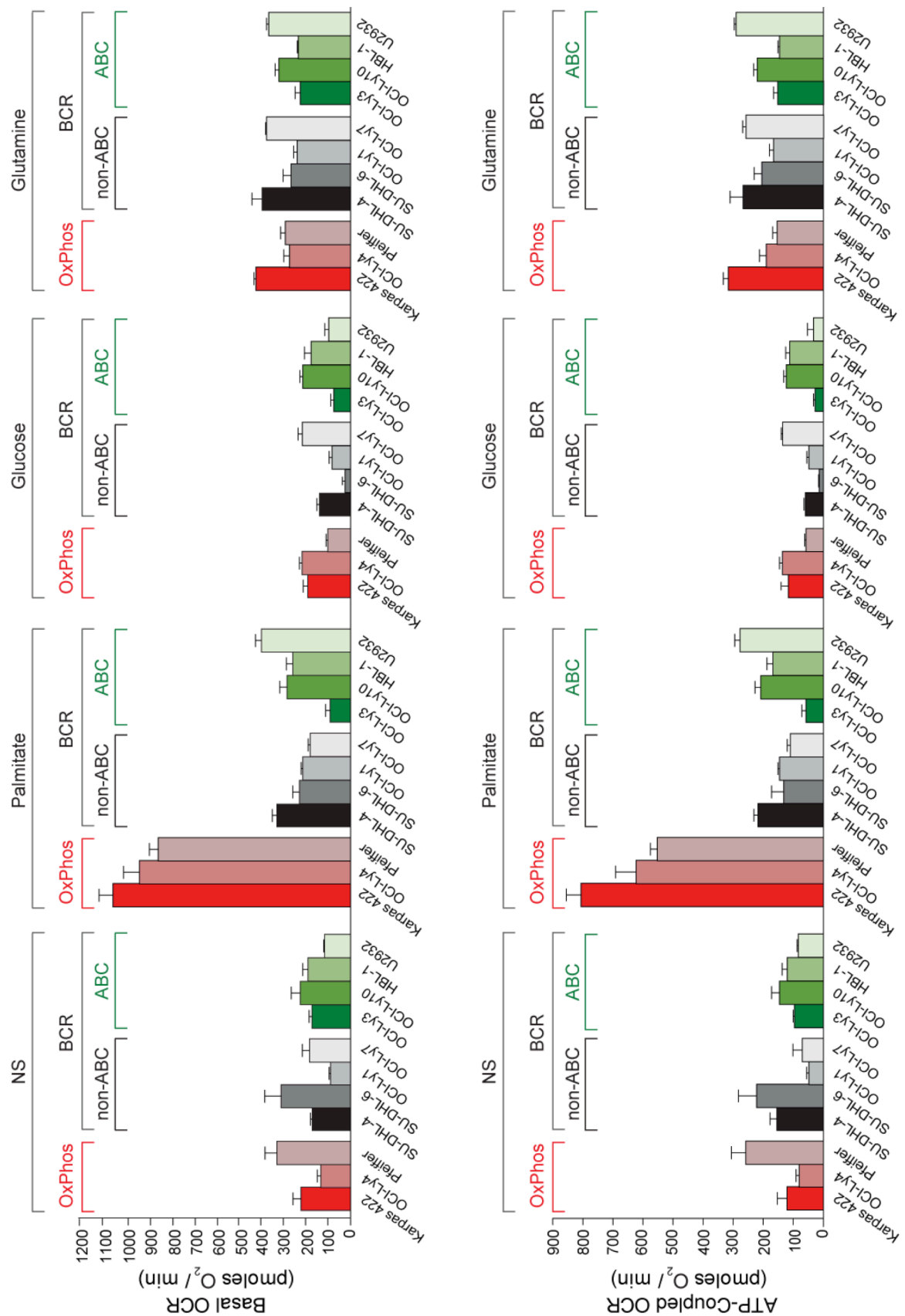

Figure 2-S3. (continued)

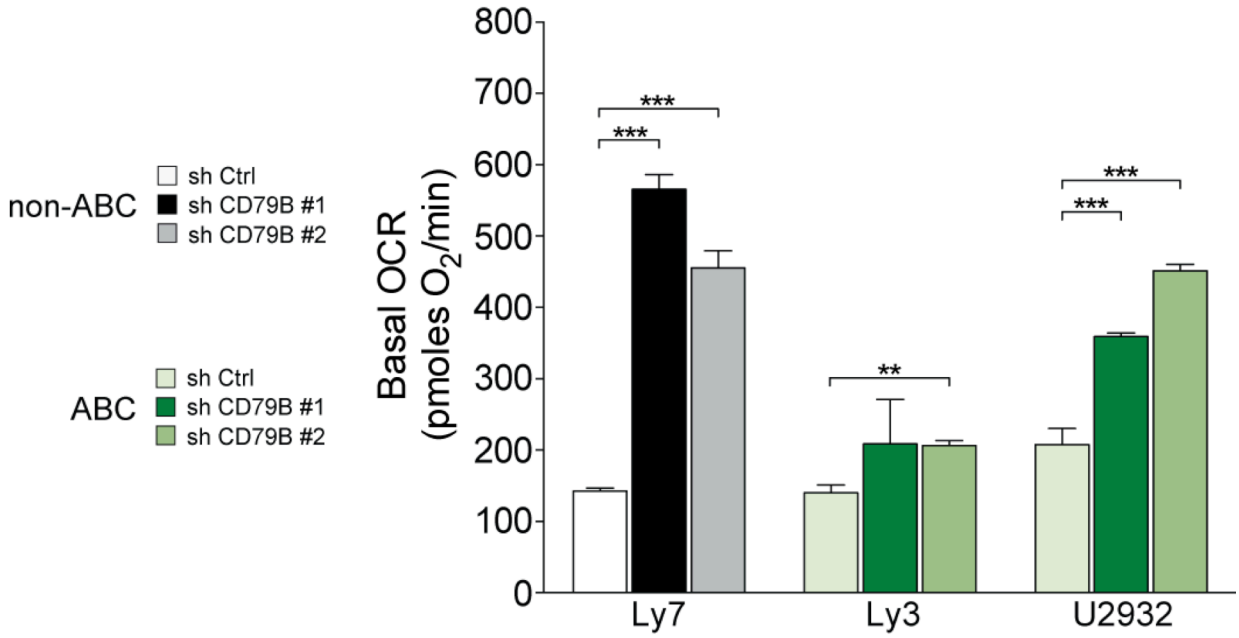

Figure 2-S4. FAO following acute knockdown of CD79B in BCR-DLBCL cell lines
Palmitate stimulated basal OCR in the indicated non-OxPhos/BCR-DLBCL cell lines following 24 hr acute knockdown of CD79B. Error bars, ± SEM. **p < 0.01; ***p < 0.001; two-tailed Student's t-test. Diminished FAO in this setting can also be corroborated by another downstream component of BCR signaling, SYK as shown in main Figure 2.4B.

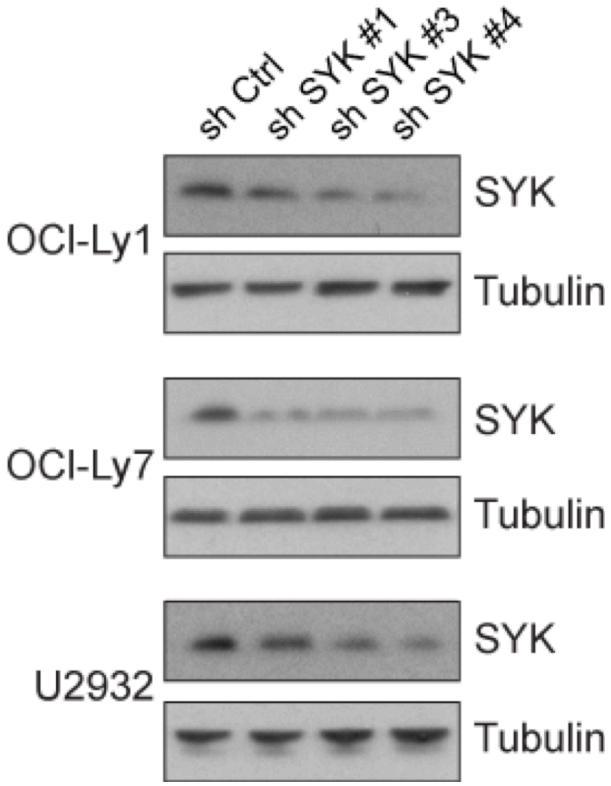

Figure 2-S5. Efficiency of SYK knockdown in BCR-type DLBCL cell lines
Efficiency of shRNA-mediated SYK depletion. SYK protein levels 24 hr after cells were infected with the indicated lentiviruses. This time point was also used to analyze the effect of palmitate on basal OCR in these same cell lines as shown in main Figure 2.4B.

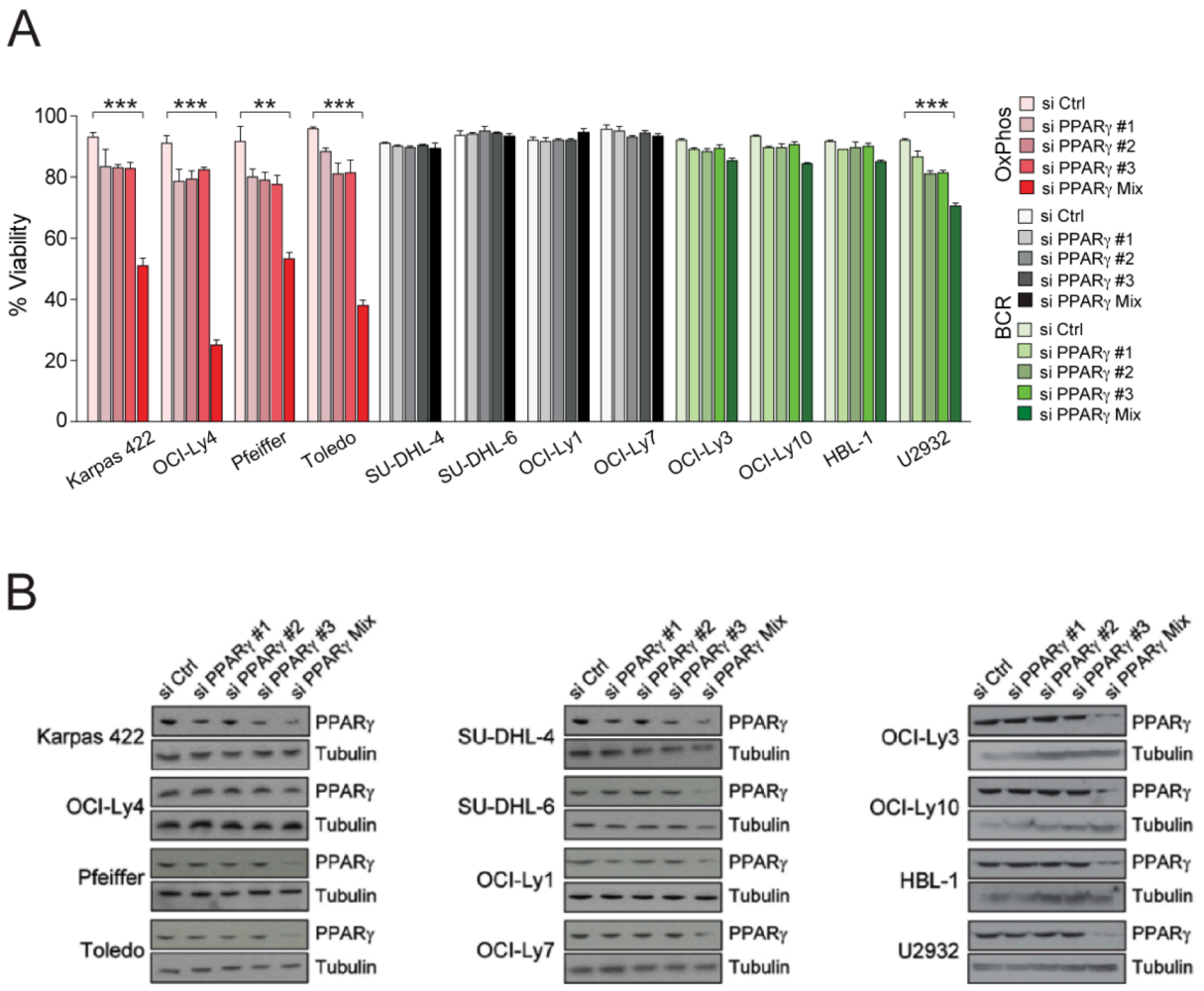

Figure 2-S6. Knockdown of PPARγ in DLBCL cell lines

(A) Viability of DLBCL cell lines after 72 hr treatment with individual or a mixture of 3 independent siRNAs against PPARγ. Error bars, ± SEM. **p <0.01; ***p < 0.001; two-tailed Student's t-test. (B) Western blot analysis of PPARγ levels in DLBCL cell lines subjected to siRNA as in (A), showing best knockdown efficiency was achieved with the mixture of independent siRNAs. See main Figure 2.7B.

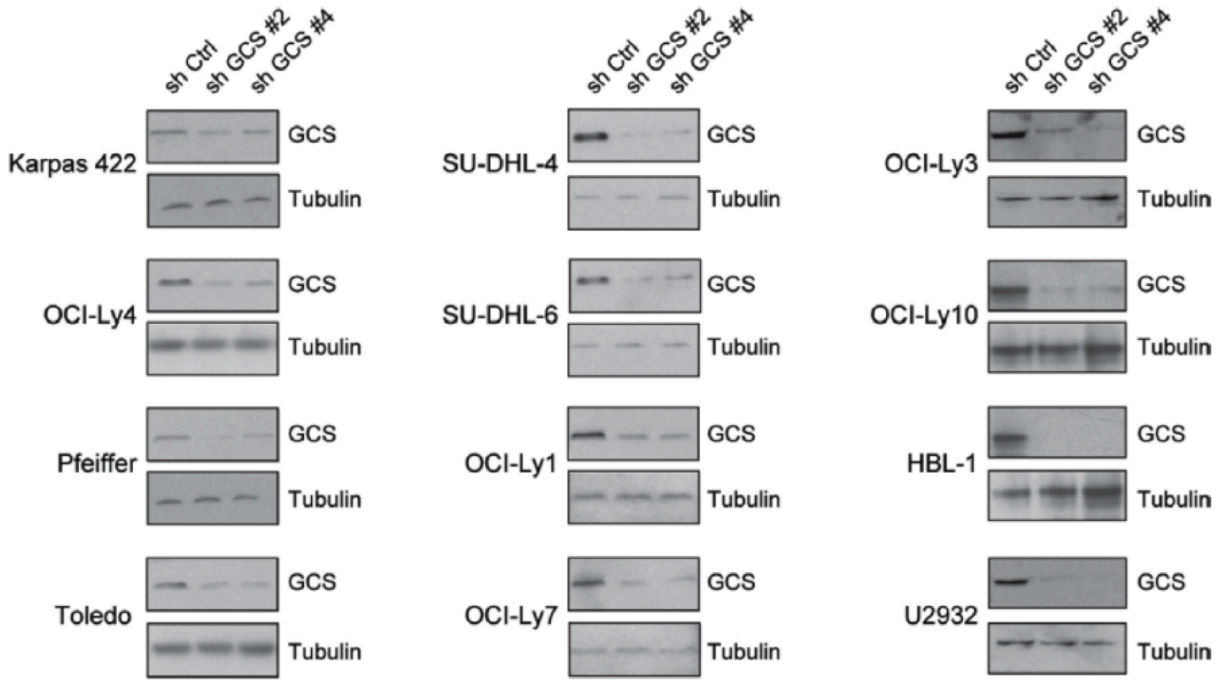

Figure 2-S7. Efficiency of shRNA-mediated GCS depletion
GCS protein levels 72 hr after the indicated DLBCL cell lines were infected with lentiviruses bearing shRNA against GCS or control viruses. See main Figure 2.12C.

Table 2-S1. Consensus cluster designations for primary DLBCL expression profile data set

Sample	CCC [Best10/13]	Sample	CCC [Best10/13]
GSM275076	OxPhos	GSM275125	BCR
GSM275077	OxPhos	GSM275126	BCR
GSM275078	OxPhos	GSM275127	BCR
GSM275079	OxPhos	GSM275128	OxPhos
GSM275080	BCR	GSM275129	OxPhos
GSM275081	OxPhos	GSM275130	BCR
GSM275082	OxPhos	GSM275131	BCR
GSM275083	HR	GSM275132	HR
GSM275084	OxPhos	GSM275133	BCR
GSM275085	HR	GSM275134	OxPhos
GSM275086	OxPhos	GSM275135	HR
GSM275087	OxPhos	GSM275136	OxPhos
GSM275088	BCR	GSM275137	Unassigned
GSM275089	OxPhos	GSM275138	HR
GSM275090	OxPhos	GSM275139	OxPhos
GSM275091	OxPhos	GSM275140	OxPhos
GSM275092	OxPhos	GSM275141	BCR
GSM275093	OxPhos	GSM275142	OxPhos
GSM275094	OxPhos	GSM275143	BCR
GSM275095	HR	GSM275144	BCR
GSM275096	BCR	GSM275145	BCR
GSM275097	BCR	GSM275146	BCR
GSM275098	OxPhos	GSM275147	BCR
GSM275099	Unassigned	GSM275148	BCR
GSM275100	OxPhos	GSM275149	OxPhos
GSM275101	BCR	GSM275150	OxPhos
GSM275102	Unassigned	GSM275151	BCR
GSM275103	OxPhos	GSM275152	OxPhos
GSM275104	BCR	GSM275153	BCR
GSM275105	HR	GSM275154	Unassigned
GSM275106	BCR	GSM275155	OxPhos
GSM275107	BCR	GSM275156	OxPhos
GSM275108	BCR	GSM275157	BCR
GSM275109	BCR	GSM275158	OxPhos
GSM275110	HR	GSM275159	OxPhos
GSM275111	Unassigned	GSM275160	OxPhos
GSM275112	HR	GSM275161	BCR
GSM275113	HR	GSM275162	HR
GSM275114	OxPhos	GSM275163	HR
GSM275115	OxPhos	GSM275164	BCR
GSM275116	OxPhos	GSM275165	OxPhos
GSM275117	OxPhos	GSM275166	Unassigned
GSM275118	OxPhos	GSM275167	OxPhos
GSM275119	OxPhos	GSM275168	OxPhos
GSM275120	BCR	GSM275169	OxPhos
GSM275121	HR	GSM275170	HR
GSM275122	HR	GSM275171	OxPhos
GSM275123	HR	GSM275172	OxPhos
GSM275124	BCR	GSM275173	HR

Table 2-S1. (continued)

Sample	CCC [Best10/13]
GSM275174	OxPhos
GSM275175	OxPhos
GSM275176	OxPhos
GSM275177	OxPhos
GSM275178	OxPhos
GSM275179	OxPhos
GSM275180	BCR
GSM275181	OxPhos
GSM275182	HR
GSM275183	HR
GSM275184	BCR
GSM275185	HR
GSM275186	HR
GSM275187	HR
GSM275188	HR
GSM275189	OxPhos
GSM275190	HR
GSM275191	OxPhos
GSM275192	OxPhos
GSM275193	Unassigned
GSM275194	BCR
GSM275195	HR
GSM275196	OxPhos
GSM275197	OxPhos
GSM275198	OxPhos
GSM275199	BCR
GSM275200	HR
GSM275201	OxPhos
GSM275202	Unassigned
GSM275203	OxPhos
GSM275204	OxPhos
GSM275205	HR
GSM275206	OxPhos
GSM275207	OxPhos
GSM275208	OxPhos
GSM275209	BCR
GSM275210	HR
GSM275211	BCR
GSM275212	BCR
GSM275213	BCR
GSM275214	HR
GSM275215	HR
GSM275216	BCR
GSM275217	BCR
GSM275218	BCR
GSM275219	Unassigned
GSM275220	BCR
GSM275221	BCR
GSM275222	BCR
GSM275223	HR
GSM275224	HR
GSM275225	HR

Sample	CCC [Best10/13]
GSM275226	BCR
GSM275227	OxPhos
GSM275228	Unassigned
GSM275229	BCR
GSM275230	HR
GSM275231	HR
GSM275232	BCR
GSM275233	HR
GSM275234	BCR
GSM275235	HR
GSM275236	HR
GSM275237	BCR
GSM275238	BCR
GSM275239	BCR
GSM275240	BCR
GSM275241	BCR
GSM275242	BCR
GSM275243	BCR
GSM275244	HR
GSM275245	HR
GSM275246	HR
GSM275247	HR
GSM275248	HR
GSM275249	Unassigned
GSM275250	BCR
GSM275251	Unassigned
GSM275252	BCR
GSM275253	BCR
GSM275254	HR
GSM275255	HR
GSM275256	BCR
GSM275257	HR
GSM275258	BCR
GSM275259	HR
GSM275260	HR
GSM275261	Unassigned
GSM275262	HR
GSM275263	BCR
GSM275264	HR
GSM275265	HR
GSM275266	BCR
GSM275267	BCR
GSM275268	Unassigned
GSM275269	BCR
GSM275270	BCR
GSM275271	OxPhos
GSM275272	BCR
GSM275273	Unassigned
GSM275274	HR
GSM275275	BCR
GSM275276	HR
GSM275277	OxPhos

Table 2-S1. (continued)

Sample	CCC [Best10/13]
GSM275278	HR
GSM275279	BCR
GSM275280	Unassigned
GSM275281	BCR
GSM275282	Unassigned
GSM275283	BCR
GSM275284	BCR
GSM275285	BCR
GSM275286	BCR
GSM275287	HR
GSM275288	BCR
GSM275289	HR
GSM275290	BCR
GSM275291	OxPhos
GSM275292	BCR
GSM275293	BCR
GSM275294	HR
GSM275295	OxPhos
GSM275296	OxPhos
GSM275297	BCR
GSM275298	BCR
GSM275299	BCR
GSM275300	HR
GSM275301	HR
GSM275302	HR
GSM275303	BCR
GSM275304	HR
GSM275305	OxPhos
GSM275306	BCR
GSM275307	BCR
GSM275308	HR

Table 2-S2. Number of patient samples assigned to each Consensus Cluster

	GCB	ABC	Unclassified	Sum
BCR	42	34	7	83
OxPhos	27	37	7	71
HR	26	19	17	62
Unassigned	12	3	2	17
Sum	107	93	33	233

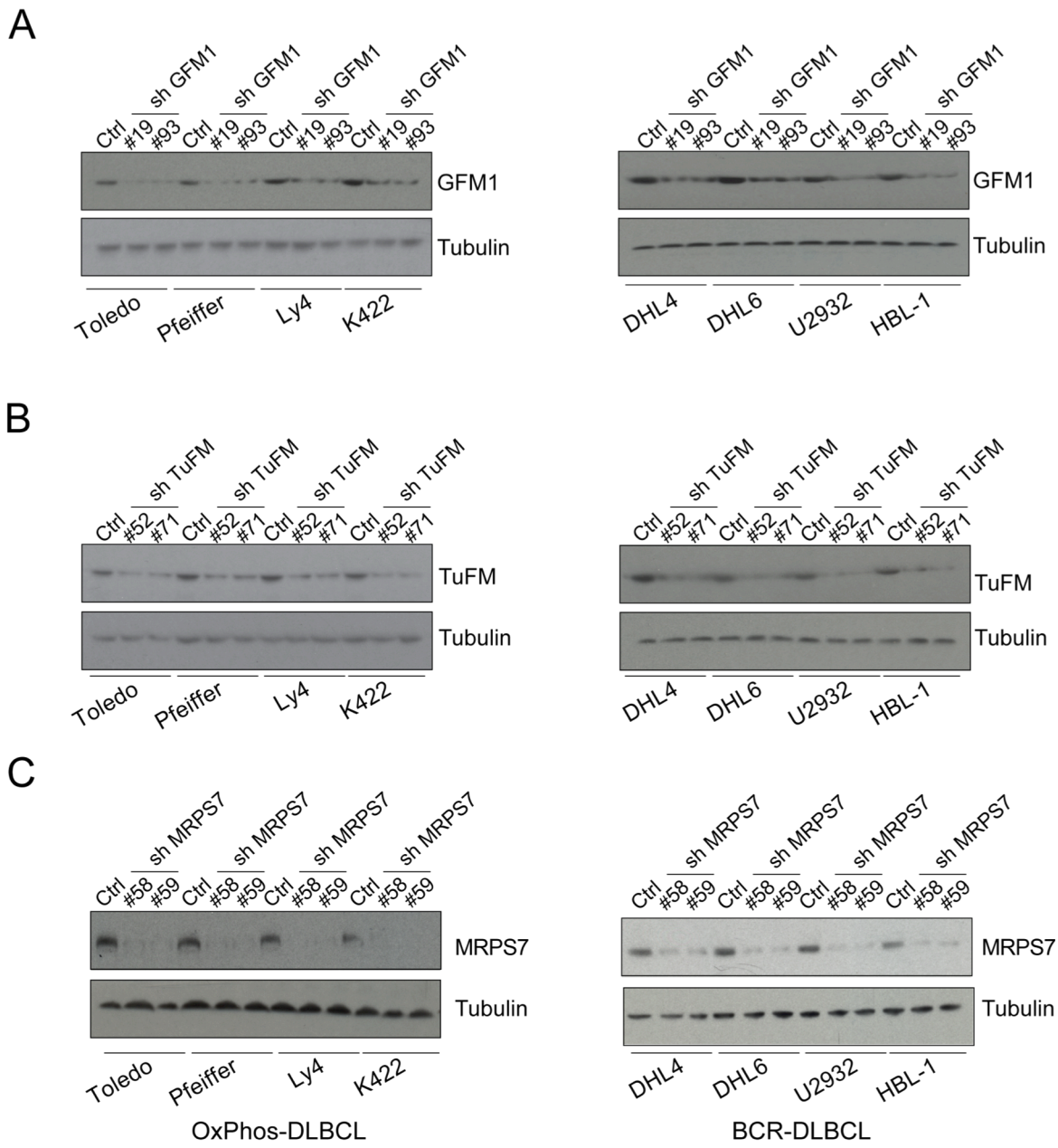

Figure 3-S1. Efficiency of shRNA-mediated depletion of mitochondrial translation components

Protein levels of GFM1 (A), TuFM (B), and MRPS7 (C) 24 hr after the indicated DLBCL cell lines were infected with lentiviruses carrying shRNAs or control viruses as in Figure 3.3A-C.

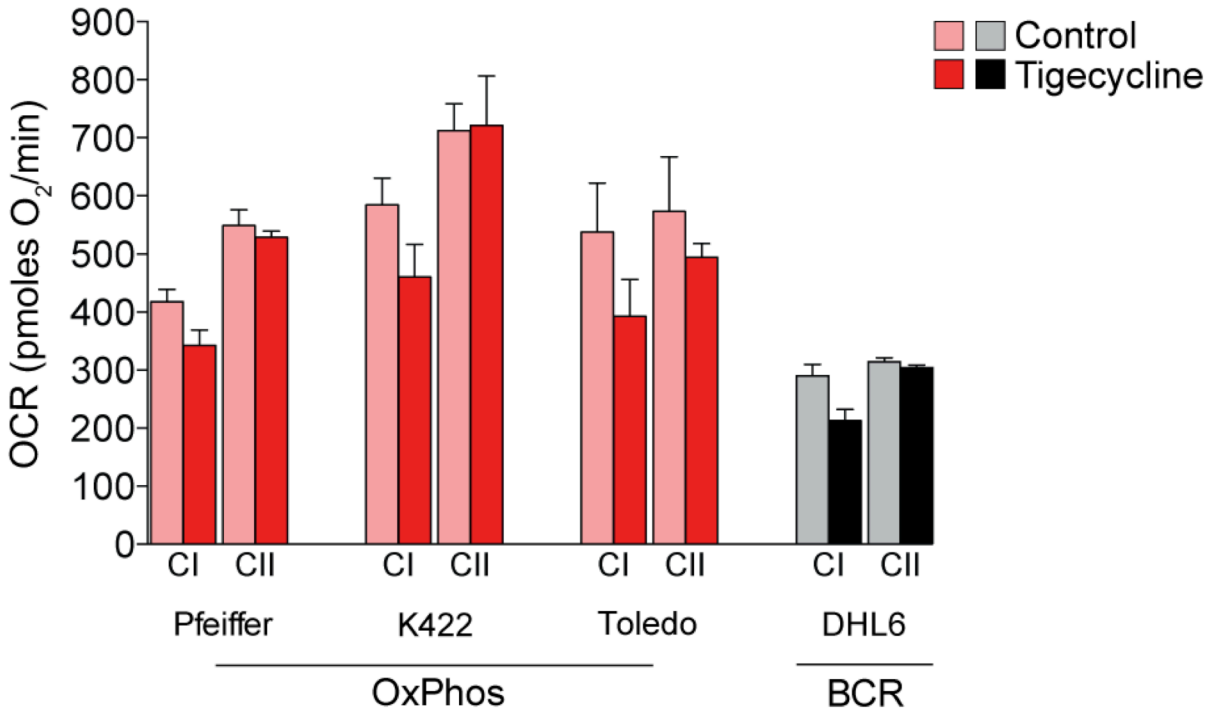

Figure 3-S2. ADP-stimulated respiration following tigecycline treatment
Effects of 20 hr treatment with 1 μM tigecycline on ADP-stimulated (State III) respiration for mitochondria isolated from OxPhos- (Pfeiffer, Karpas 422 and Toledo) or BCR- (SU-DHL-6) DLBCL cell lines. Respiration rates were measured in the presence of complex I (CI) or complex II (CII) linked substrates. Error bars, ± SEM. See main Figure 3.5B.

Table 3-S1. Identification of mtDNA-encoded ETC subunits enriched in the OxPhos-DLBCL mitochondrial proteome

Gene Symbol and Protein Name	Total OxPhos Signal	Total BCR Signal	Total Spectra	Total Peptides	Peptide Sequences	Log Ratio (OxPhos/BCR)	log Intensity	Ratio (OxPhos/BCR)
COX2	1303	365	13	6	IFEMGPVFTL, LLDVDNRVVLPIEAPIR, VVLPIEAPIR, LLDVDNR, MMITSQDVLHSWAVPTL GLK, TDAIPGR	0.55	3.22	3.57
ATP6	71	27	1	1	LITTQQWLIK	0.42	1.99	2.63
ATP8	157	110	1	1	ICSLHSLPPQS	0.15	2.43	1.43

Table lists mtDNA-encoded proteins enriched in the same mitochondrial samples from OxPhos and BCR-DLBCL cell lines used to identify and quantitate the potein translation factors in Figure 3.2. The number and list of unique tryptic peptides shown for each protein are indicated. Abundance ratios were derived by summing iTRAQ reporters for all unique peptides per protein.

Table 3-S2. Identification of mitochondrial translation factors enriched in the OxPhos-DLBCL proteome

Table lists unique peptides identified across each mitochondrial translation factor shown in Figure 3.2. The number and list of unique tryptic peptides identified for each protein are indicated. Abundance ratios were derived by summing iTRAQ reporters for all unique peptides per protein.

Table 3-S2. (continued)

Gene Symbol and Protein Name	Total OxPhos Signal	Total BCR Signal	Total Spectra	Total Peptides	Peptide Sequences	log2 Ratio (OxPhos/BCR)	log2 Intensity	Ratio (OxPhos/BCR)
DARS2 Mitochondrial aspartyl-tRNA synthetase 2	1101	349	19	12	DIESIR, MPTGEIEIK, LECADLLETR, IIDISDVFR, SFQMQYNLR, LRLECADLLETR, AICIPEGAK, NTEIGFLQDALSKPHGTVK, NFAADHFNQEILPVFLNANR, ACSLLGK, LMETQEEDVVLLTAGEHNK, QLLMVGGLDR	1.66	10.50	3.2
GFM1 Mitochondrial G elongation factor 1	883	387	21	16	FGQLTYVR, IPSISDLK, SFTPVFLGSALK, GIVDLIEER, SCTEGKGEYTMEYSR, GFLDACEK, DGVGAVMDSMELER, AAATDHRQELIECVANSDEQLGEMFLEEK (OxMet), VIGVLEPLDPEDYTK, EYGCPCITGKPK, AIYFDGDFGQIVR, DNSHPFVGLAFK, SYQGELK, EDPTFK, FVLQDGAHHMVDSNEISFIR, GKDGVGAVMDSMELER	1.19	10.31	2.3
MRPL12 Mitochondrial ribosomal protein L12	2057	674	12	7	LVESLPQEIK, AALEAVGGTVVLE, NYIQGINLVQAK, LTEAKPVDK, IKAALEAVGGTVVLE, KLVESLPQEIK, THFTVR	1.61	11.42	3.1
MRPL46 Mitochondrial ribosomal protein L46	382	136	9	6	DELGDYLKPK, ADLHDEEDEQDILLAQDLEDMWEQK (OxMet), KADLHDEEDEQDILLAQDLEDMWEQK (OxMet), TLATLSENNMEAK, NLVLLVR, FVSDL	1.49	9.02	2.8
MRPS16 Mitochondrial ribosomal protein S16	91	23	4	2	LVALNLDR, LLGLAGFFPLHPMMITNAER	1.98	6.83	4.0
MRPS22 Mitochondrial ribosomal protein S22	490	160	8	6	DQAAEGINLIK, VPINDVLAEDK, LKMPPVLEER, IDGLLIDQIQR, LMTQAQLEEATR, MTGLNLQK	1.61	9.34	3.1
MRPS25 Mitochondrial ribosomal protein S25	237	98	5	3	SNKEIMEHIR, NMTPSPFLR, ECICEVEGQVPCPSLVPLPK	1.27	8.39	2.4
MRPS5 Mitochondrial ribosomal protein S5	777	292	23	15	GLHVVEIR, DPEPEDEVPDVK, SKEEQEKVEADMIQQR, NVFTMTAK, YEDHTIFHDISLR, EECGPLPIVVASPR, LTADELWK, YGFLWPGLNVPLMK, VSGSINMLSLTQGLFR, AIITICR, ILEVR, GALAETGAGAK, VEADMIQQR, GAAGFSIGK, KDPEPEDEVPDVK	1.41	10.06	2.7
MRPS7 Mitochondrial ribosomal protein S7	508	195	11	9	FYQVPVPLPDR, NCEPMIGLVPILK, FYQVPVPLPDRR, SLMIQTLEAVK, LLEAFHNQGPVIK, TLMPEK, RFLAMK (OxMet), WMITECR, TSSVFEDPVISK	1.38	9.46	2.6
MRPS9 Mitochondrial ribosomal protein S9	1275	463	22	14	SVTLESK, HLANMMGEDPETFTQEDIDR, LGKHDVTCTVSGGGR, AIAYLFPSGLFEK, AEAIVYK, QAGLLTTDPR, LLTSQCGAAEEEFVQR, EQLMFPFHFVDR, RETYTEDFIKK, ETYTEDFIKK, HPEQIFPR, LSDLDYMQFIR, QIEEFNIGKR, SLLPEK	1.46	10.76	2.8
PUS1 Pseudouridine synthase 1	62	19	3	3	TIEDDLVSALVR, APGLGLVLER, LSAETLQQVNR	1.71	6.34	3.3
TUFM Mitochondrial Tu translation elongation factor	33870	12071	65	36	AEAGDNLGALVR, GITINAAHVEYSTAAR, TVVTGIEMFHK, QPMILEK (OxMet), TVVTGIEMFHK (OxMet), TIGTGLVTNTLAMTEEEK (OxMet), DPELGLK, KGDECELLGHSK, TTLTAAITK, GTVVTGTLER, ELAMPGEDLK (OxMet), ELAMPGEDLKFNLILR, ELAMPGEDLK, FKKYEEIDNAPEER, HYAHTDCPGHADYVK, KYEEIDNAPEER, TIGTGLVTNTLAMTEEEK, QIGVEHVVVYVNK, NMITGTAPLDGCILVVAANDGPMPQTR (OxMet), ELLTEFGYK, NMITGTAPLDGCILVVAANDGPMPQTR (OxMet), GDECELLGHSK, IILPPEK, ADAVQDSEMVELVELEIR, ILAEGGGAK, QPMILEK, LLDAVDTYIPVPAR, DLEKPFLLPVEAVYSVPGR, DKPHVNVGTIGHVDHGK, VEAQVYILSK, NMITGTAPLDGCILVVAANDGPMPQTR, YEEIDNAPEER, IILPPEKELAMPGEDLK, ADAVQDSEMVELVELEIR (OxMet), GEETPVIVGSALCALEGRDPELGLK, IILPPEKELAMPGEDLKFNLILR	1.49	15.49	2.8
YARS2 Mitochondrial tyrosyl-tRNA synthetase 2	359	166	13	9	AGHNVIALVGGATAR, LGLEALAANHQQLFTDGR, IELPELFDR, TSPFELYQFFVR, LTGEDVFGITVPLITSTTGAK, NFYIIK, SAGNAVWLNR, VQLGGSDQLGNIMSGYEFINK, AHSGAQGLLAAQK	1.11	9.04	2.2

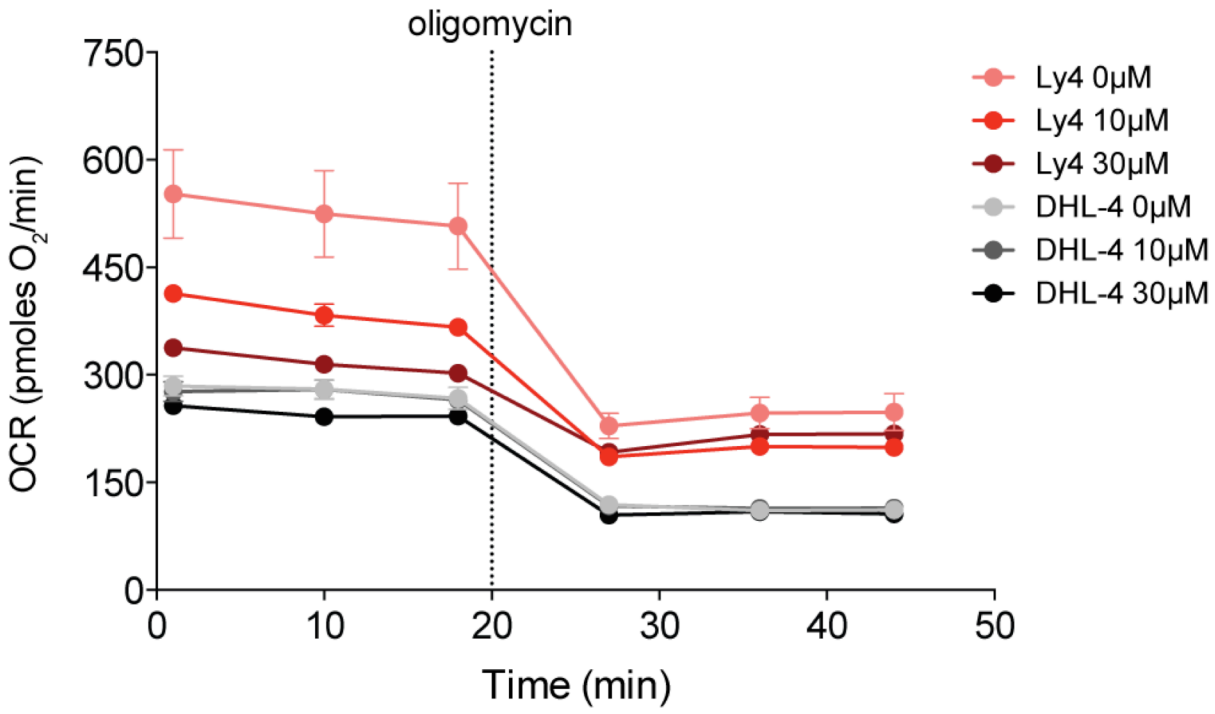

Figure 4-S1. Representative rates of palmitate respiration following mdivi-1 treatment
Representative oxygen consumption rates (OCR) for one OxPhos-DLBCL (OCI-Ly4) and one BCR-DLBCL (SU-DHL-4) cell line supplied with exogenous palmitate following 24 hr mdivi-1 treatment at the indicated concentrations. Error bars, ± SD. See main Figure 4.4A.

Figure 4-S2. Representative traces of oxygen consumption rates on various substrates following DRP1-DN expression

Representative assay for mitochondrial oxygen consumption rates (OCR) in response to 2 mM L-glutamine, 0.5 mM hexanoate or 0.2 mM palmitate after 24 hr lentiviral transduction with DRP1-DN. Data shown is from one OxPhos-DLBCL cell line (OCI-Ly4). Error bars, ± SD. See main Figure 4.5.

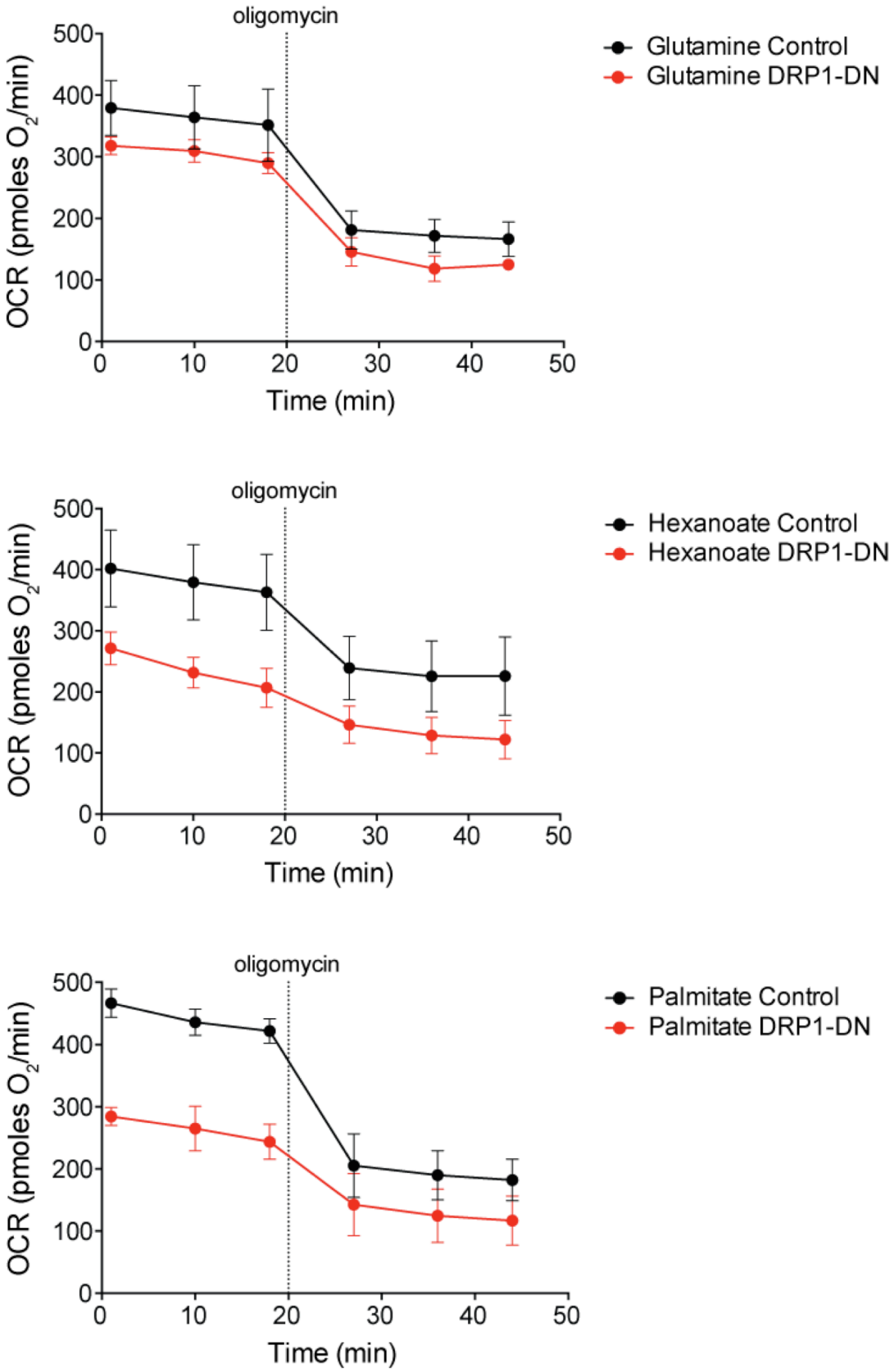

Figure 4-S2. (continued)

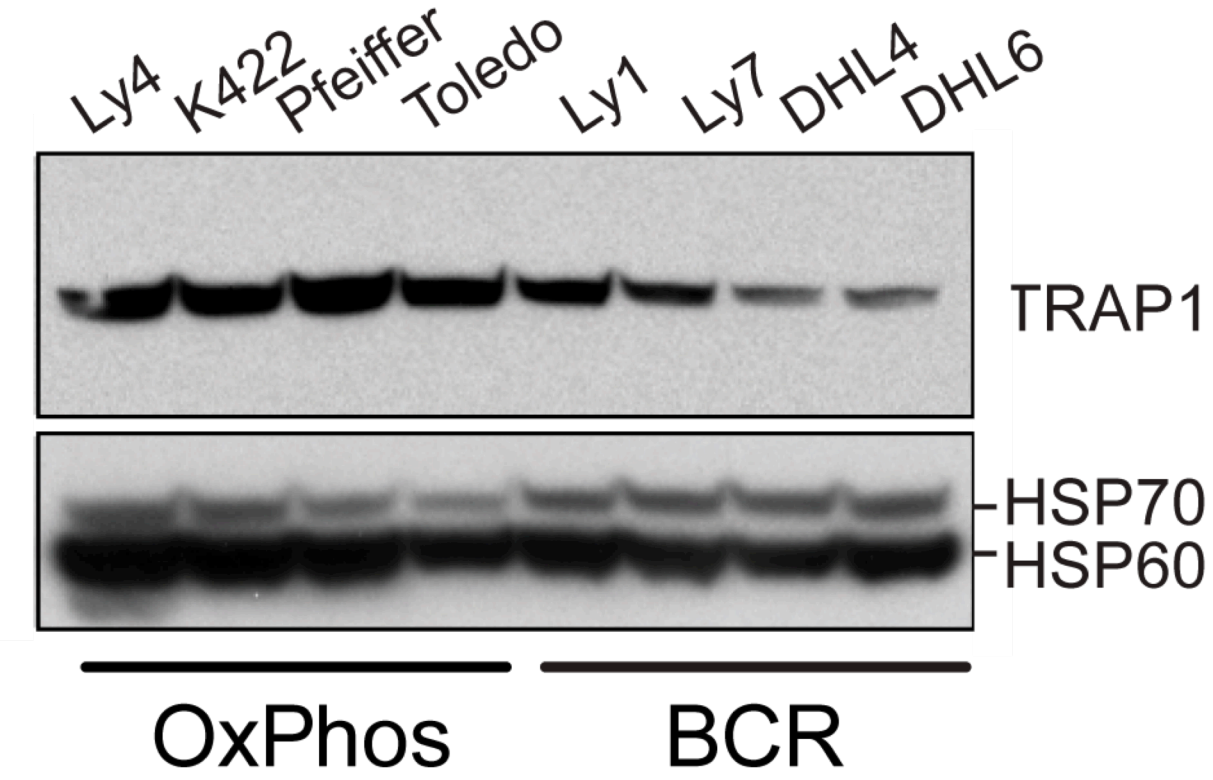

Figure 4-S3. Differential expression of TRAP1 in mitochondria-enriched heavy membrane fractions prepared from DLBCL cell lines
Western blot analysis of TRAP1 levels in mitochondria-enriched heavy membrane fractions derived from OxPhos- and BCR-DLBCL cell lines. HSP70 and HSP60 serve as loading controls.

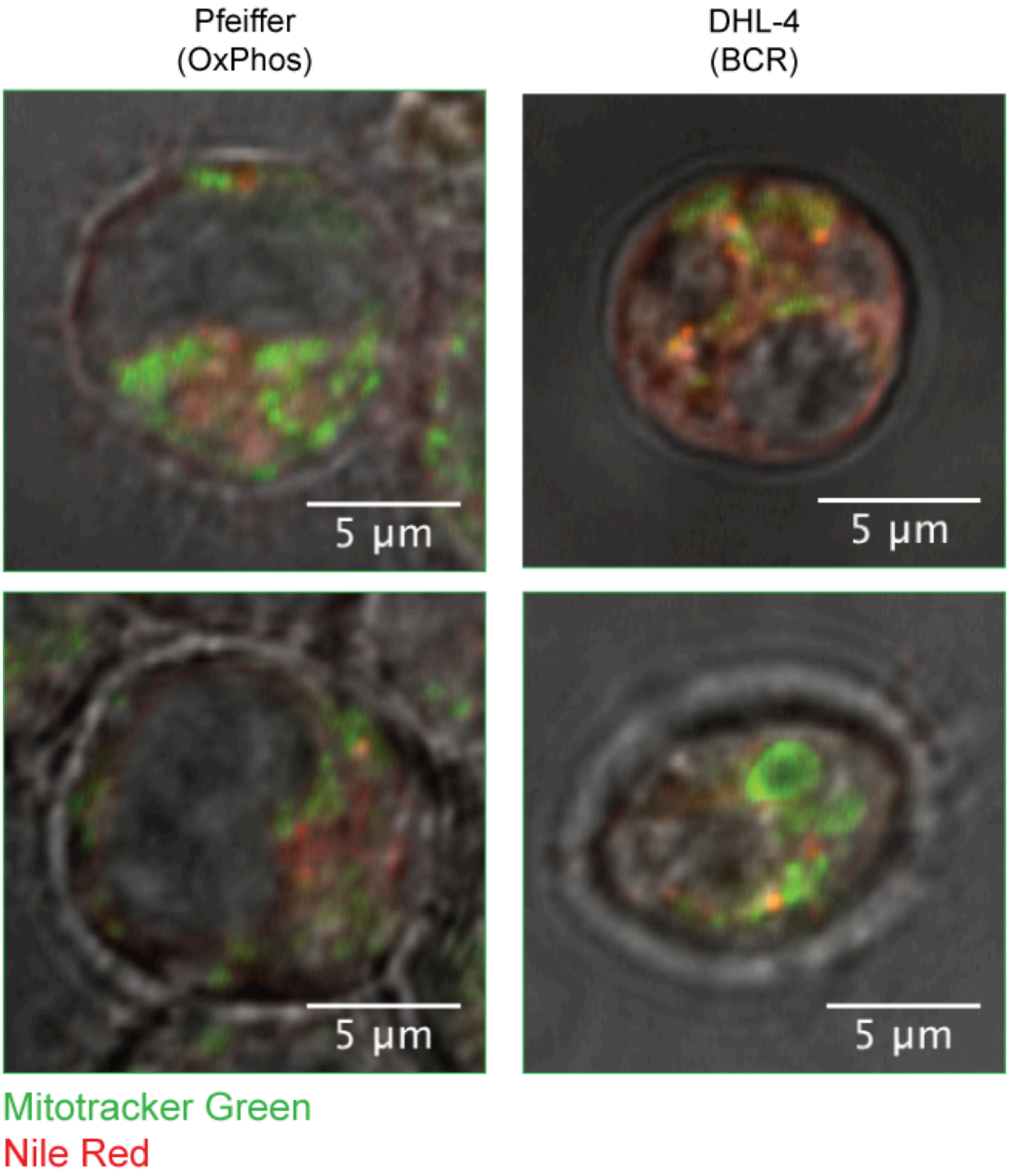

Figure 4-S4. DLBCL cell lines contain lipid droplets
Lipid droplets were visualized using Nile Red in an OxPhos- (Pfeiffer) and BCR- (SU-DHL-4) DLBCL cell line. Live cells were incubated for 30 min in 100 nM Mitotracker Green followed by labeling with 1 μg/ml Nile Red for 15 min. Images were collected using a Zeiss LSM 710-Live Duo Scan confocal microscope on live cells immobilized in 0.5% agarose/media.